



THE HONG KONG
POLYTECHNIC UNIVERSITY

香港理工大學

Pao Yue-kong Library

包玉剛圖書館

Copyright Undertaking

This thesis is protected by copyright, with all rights reserved.

By reading and using the thesis, the reader understands and agrees to the following terms:

1. The reader will abide by the rules and legal ordinances governing copyright regarding the use of the thesis.
2. The reader will use the thesis for the purpose of research or private study only and not for distribution or further reproduction or any other purpose.
3. The reader agrees to indemnify and hold the University harmless from and against any loss, damage, cost, liability or expenses arising from copyright infringement or unauthorized usage.

IMPORTANT

If you have reasons to believe that any materials in this thesis are deemed not suitable to be distributed in this form, or a copyright owner having difficulty with the material being included in our database, please contact lbsys@polyu.edu.hk providing details. The Library will look into your claim and consider taking remedial action upon receipt of the written requests.

**GIANT MAGNETOSTRICTIVE COMPOSITES
FOR SMART TRANSDUCER AND ACTUATOR
APPLICATIONS**

LO CHING YIN

M.PHIL.

**THE HONG KONG
POLYTECHNIC UNIVERSITY**

2008

THE HONG KONG POLYTECHNIC UNIVERSITY

DEPARTMENT OF APPLIED PHYSICS

**GIANT MAGNETOSTRICTIVE COMPOSITES
FOR SMART TRANSDUCER AND ACTUATOR
APPLICATIONS**

LO CHING YIN

**A thesis submitted in partial fulfillment of
the requirements for the Degree of
MASTER OF PHILOSOPHY**

JUNE 2007

CETIFICATE OF ORIGINALITY

I hereby declare that this thesis is my own work and that, to the best of my knowledge and belief, it reproduces no material previously published or written, nor material that has been accepted for the award of any other degree or diploma, except where due acknowledgment has been made in the text.

(Signed)

LO CHING YIN

(Name of Student)



Abstract

Magnetostrictive materials are the most widely used magnetomechanically coupled smart materials. Terfenol-D ($\text{Tb}_{0.3}\text{Dy}_{0.7}\text{Fe}_{1.92}$), a rare earths-iron alloy, is the best-known magnetostrictive material. While possessing giant magnetostrictive strain (~ 1000 ppm) and expeditious response ($\sim 1 \mu\text{s}$) at room temperature and low fields (< 200 kA/m), [112]-textured monolithic Terfenol-D suffers from four intrinsic problems. The first is the eddy current-induced heating and bandwidth limitation to a few kilohertz; the second is the brittleness-imposed challenges to machining and shape novelty; the third is the lack of composition and property varieties; and the fourth is the high material cost. These problems have urged the necessity of developing polymer-bonded magnetostrictive composites in the recent decade. Laminated composites fabricated with Terfenol-D thin sheets have improved operating frequencies of about 20 kHz at the expense of high production cost and less shape flexibility. Particulate and particulate-chain composites based on irregularly shaped, randomly oriented Terfenol-D particles (10 – 300 μm size) are relatively practicable, but their strain values fall short of their monolithic material by at least 30 %. The recently reported short-fiber composites with needle-shaped, [112]-oriented Terfenol-D short fibers (~ 3 mm long and 0.8 mm wide) exhibit the largest strain outputs, reaching about 80 % of the monolithic Terfenol-D.

In this study, we aimed to evolve the polymer-bonded magnetostrictive composites into a promising new type of crystallographically oriented continuous- (or long-) fiber composite, showing even larger magnetostrictive strains compared to the monolithic Terfenol-D, besides preserving the desired advantages of the existing



magnetostrictive composites. Applications of the continuous-fiber composites in smart transducers and actuators were also realized.

[112]-oriented Terfenol-D continuous fibers of 45 mm long and (1 mm × 1 mm) square cross section were prepared with the highly magnetostrictive [112] crystallographic axis of monolithic Terfenol-D oriented along their long axes. Bar-shaped epoxy-bonded Terfenol-D continuous-fiber composites with a preferred [112] crystallographic orientation were fabricated with length 45 mm and square cross section (12 mm × 12 mm) using six Terfenol-D volume fractions ranging from 0.2 to 0.7. Epoxy-bonded Terfenol-D short-fiber and particulate-chain composites of the same dimensions were also produced for comparison. The quasistatic magnetic and magnetostrictive properties of the composites were measured as functions of applied magnetic field, Terfenol-D volume fraction, and post-curing temperature with zero external stress loading and at room temperature. The proposed continuous-fiber composites, after being post-cured at 80 °C, exhibited extremely large saturation strains in excess of 1600 ppm at 400 kA/m. These saturation strains not only were the largest reported values in polymer-bonded Terfenol-D composites, but also exceeded the unloaded monolithic Terfenol-D value (= 1115 ppm at 400 kA/m) by 43 %.

A physical model, based on the composite mechanics and filled with the requirements for temperature-dependent stress equilibrium within the composites and stress-dependent saturation strain of Terfenol-D, was presented to obtain an insight into the observed tremendous saturation strains in the continuous-fiber composites. It was found that the higher saturation strain compared to the monolithic Terfenol-D and their short-fiber and particulate-chain composites is mainly due to the residual compressive stresses developed in the continuous fibers during epoxy cure, a higher



fiber aspect ratio for greater stress transfer from the fibers to the matrix, and the texturing of the fibers along the highly magnetostrictive [112] crystallographic axis, respectively.

The dynamic magnetic and magnetostrictive properties of the continuous-fiber composites were evaluated as functions of frequency, magnetic bias field, and Terfenol-D volume fraction. The observed frequency dependent data indicated an insignificant eddy-current effect in the composites for operating frequencies up to 500 kHz. The bias field dependent data provided an improved understanding of the magnetization and magnetostriction processes in the composites. The volume fraction dependent data suggested an optimal device performance and cost by using composites with Terfenol-D volume fractions not less than 0.5. The overall property improvements in the continuous-fiber composites were expected to broaden the practical use of the magnetostrictive composites. A guide to designing and optimizing the composites for device applications was generated.

Two distinct smart devices were developed to demonstrate the application potential of the continuous-fiber composites. These included a tunable vibration absorber for active absorption of vibrations in vibrating structures and a 64 kHz sandwich transducer for sonic and ultrasonic driving. The structure, operational principle, design modeling/simulation, fabrication, and characterization of the smart devices were included. A number of publications (comprising three published journal papers, three submitted journal papers, and two presented conference papers) were produced during the course of this study, elucidating the originality and practical applications of the present work.



List of Publications

REFERRED TECHNICAL JOURNALS:

- [1] Siu Wing Or, Ching Yin Lo, Helen Lai Wa Chan, and Ping Kong Choy, “Tunable Vibration Absorber Incorporating Giant Magnetostrictive Composite Actuator and Piezoelectric Ceramic Sensors”, *Sensors and Actuators A: Physical* (submitted).
- [2] H. L. Liu, C. Y. LO, H. Y. Tam, and S. W. Or, “A Magneto-Strictive Composite–Fibre Bragg Grating (MSC–FBG) Magnetic Field Sensor with Large Dynamic Operational Frequency Range”, *IEEE Photonic Technology Letters* (submitted).
- [3] Ching Yin Lo, Siu Wing Or, and Helen Lai Wa Chan, “1600 ppm Unloaded Magnetostriction in Epoxy-Bonded Terfenol-D Continuous-Fiber Composites with [112] Crystallographic Orientation”, *Journal of Applied Physics* (submitted).
- [4] Ching Yin Lo, Siu Wing Or, and Helen Lai Wa Chan, “Large Magnetostriction in Epoxy-Bonded Terfenol-D Continuous-Fiber Composite with [112] Crystallographic Orientation”, *IEEE Transactions on Magnetics*, Vol. 42, No. 10, pp. 3111–3113 (October 2006).



- [5] J. J. Liu, S. W. Or, C. Y. LO, W. J. Ren, and Z. D. Zhang, “Magnetic and Magnetostrictive Properties of $Tb_xDy_{0.7-x}Pr_{0.3}(Fe_{0.9}B_{0.1})_{1.93}$ Compounds and Their Composites, *IEEE Transactions on Magnetics*, Vol. 42, No. 10, pp. 3114–3116 (October 2006).
- [6] Siu Wing Or, Chung Sheung Yung, and Ching Yin LO, “A 64-kHz Sandwich Transducer Fabricated Using Pseudo 1–3 Magnetostrictive Composite”, *IEEE Transactions on Magnetics*, Vol. 42, No. 1, pp. 47–50 (January 2006).

INTERNATIONAL CONFERENCE PROCEEDINGS:

- [1] Siu Wing Or, Ching Yin LO, Helen Lai Wa Chan, and Ping Kong Choy, “Tunable Vibration Absorber Incorporating Piezoelectric-Magnetostrictive Sensoriactuator”, *Proceedings World Forum on Smart Materials and Smart Structures Technology (SMSST' 07)*, 22–24 May 2007, Golden Resources Hotel, Jiangbei District, Chongqing, China (in press) (*Invited Paper*).
- [2] H. L. Liu, H. Y. Tam, C. Y. LO, and S. W. Or, “A Novel High Frequency Magnetostrictive Composite-Fiber Bragg Grating Sensor”, *Proceedings 2007 Optical Fiber Communication Conference and Exposition and National Fiber Optic Engineers Conference (OFC/NFOEC 2007)*, March 25–29, 2007, Anaheim Covention Center, Anaheim, California, USA, Paper JWA16 (in press).



Acknowledgements

I would like to express my deep appreciation to my chief supervisor, Dr Derek Siu Wing Or, for his precious guidance and advice throughout the course of my studies.

I would also like to thank my co-supervisor, Prof. Helen Lai Wa Chan, for her constant encouragement and support.

Thanks are also due to Dr Kin Hung Wong for providing useful suggestions and comments to this work.

To my colleagues: Mr. Cheung Yu Lau, Mr. Chang Shen Wu, Mr. Chung Sheung Yung, Dr Kwok Ho Lam, Dr Siu Hong Choy, and Ms Wai Yin Wong, I owe special thanks to their contributing discussions and technical assistance.

I gratefully acknowledge the financial support from the Competitive Earmarked Research Grant (CERG) of the Research Grants Council (RGC) of the HKSAR Government under Grant No. PolyU 5289/04E.

Last, I would like to express my gratitude to my parents and my sister for their understanding and encouragement during my studies.



Table of Contents

	<u>Page</u>
Abstract	i
List of Publications	iv
Acknowledgments	vi
Table of Contents	vii
List of Symbols and Their Units	x
List of Figure Captions	xii
List of Table Captions	xx
Chapter 1 Introduction	
1.1 Magnetism	1
1.1.1 Magnetic Fields	2
1.1.2 Magnetization	5
1.1.3 Magnetization Processes	7
1.2 Magnetostriction	12
1.2.1 Spontaneous Magnetostriction	13
1.2.2 Saturation Magnetostriction	14
1.2.3 Joule Magnetostriction	15
1.2.4 Magnetization and Magnetostriction Processes	16
1.3 Review of Magnetostrictive Materials	21
1.3.1 Transition Metals	24
1.3.2 Rare Earth Single Crystals	25
1.3.3 Rare Earth-Iron Alloys	26
1.3.4 Terfenol-D	28
1.3.5 Epoxy-Bonded Terfenol-D Composites	30
1.3.5.1 Laminated Composites	31
1.3.5.2 Particulate and Particulate-Chain Composites	32
1.3.5.3 Short-Fiber Composites	34
1.4 Objective of Project	36
1.5 Scope of Project	36
Chapter 2 Fabrication of Epoxy-Bonded Terfenol-D Continuous-Fiber Composites	39



2.1	Introduction	39
2.2	Preparation of Terfenol-D Elements	40
2.2.1	Material Used	40
2.2.2	[112]-Oriented Terfenol-D Continuous Fibers	42
2.2.3	[112]-Oriented Terfenol-D Short Fibers	47
2.2.4	Random-Oriented Terfenol-D Particles	48
2.3	Preparation of Epoxy Matrix	49
2.4	Fabrication of Epoxy-Bonded Terfenol-D Composites	50
2.4.1	Continuous-Fiber Composites	50
2.4.2	Short-Fiber and Particulate-Chain Composites	53
Chapter 3	Quasistatic Material Properties of Continuous-Fiber Composites	55
3.1	Introduction	55
3.2	Quasistatic Measurements	56
3.2.1	Experimental Arrangement and Method	56
3.2.2	Results and Discussion	59
3.2.2.1	Magnetostrictive Properties	59
3.2.2.2	Magnetic Properties	78
3.2.2.3	Domain Magnetization Processes	84
3.3	Theoretical Implication with a Physical Model	87
3.3.1	Formulation of Physical Model	87
3.3.2	Application to Experimental Results	90
Chapter 4	Dynamic Material Properties of Continuous-Fiber Composites	92
4.1	Introduction	92
4.2	Dynamic Measurements	93
4.3	Results and Discussion	96
4.3.1	Frequency Dependent Data	96
4.3.2	Bias Field Dependant Data	108
4.3.3	Volume Fraction Dependant Data	114
Chapter 5	Applications to Smart Devices	121
5.1	Introduction	121
5.2	Tunable Vibration Absorber	122
5.2.1	Application Background	122
5.2.2	Structure and Operating Principle	123



5.2.3	Fabrication	129
5.2.4	Characterization	133
5.2.4.1	Tunability	133
5.2.4.2	Sensibility	136
5.2.4.3	Vibration Absorption	139
5.2.5	Concluding Remarks	140
5.3	64 kHz Sandwich Transducer	142
5.3.1	Application Background	142
5.3.2	Design and Fabrication	143
5.3.3	Characterization	159
5.3.4	Concluding Remarks	163
Chapter 6	Conclusions and Suggestions for Future Work	164
6.1	Conclusions	164
6.1.1	[112]-Oriented Terfenol-D Continuous Fibers	164
6.1.2	Epoxy-Bonded Terfenol-D Continuous-Fiber Composites	165
6.1.3	Applications to Smart Devices	166
6.2	Suggestions for Future Work	168
6.2.1	Epoxy-Bonded, Light Rare Earths-Substituted Terfenol-D Continuous-Fiber Composites	168
6.2.2	Power Sonic and Ultrasonic Devices	169
	List of References	170



List of Symbols and Their Units

<i>Symbol</i>	<i>Meaning</i>	<i>SI Unit</i>
A	Area	m^2
B_i	Dynamic magnetic flux density component	T
B_i^{QS}	Quasistatic magnetic flux density component	T
B_r	Remanent magnetic flux density	T
c_{ijkl}, c_{pq}	Elastic stiffness coefficient	Pa
d	Displacement	m
d_{ijkl}, d_{pq}	Dynamic magnetomechanical strain coefficient	C/N or m/A
d_{pq}^{QS}	Quasistatic magnetomechanical strain coefficient	m/A
E_i^B	The elastic moduli component at constant magnetic flux density	V/m
E_i^H	The elastic moduli component at constant magnetic field strength	V/m
f	Frequency	Hz
f_a	Anti-resonance frequency	Hz
f_r	Resonance frequency	Hz
F	Force	N
H_{Bias}	Bias magnetic field	A/m or Oe
H_i	Dynamic magnetic field component	A/m or Oe
H_i^{QS}	Quasistatic magnetic field component	A/m or Oe
k_{pq}	Electromechanical coupling coefficient or Magnetomechanical coupling coefficient	–
L, l	Length	m
$\Delta\ell$	Change in length	m
m	Mass	g
M	Magnetization	T
M_i	Dynamic magnetization component	T
M_i^{QS}	Quasistatic magnetization component	T
M_S	Saturation magnetization	T



<i>Symbol</i>	<i>Meaning</i>	<i>SI Unit</i>
S_i	Strain component	m^2/N
t	Thickness	m
T	Temperature	$^{\circ}\text{C}$
T_C	Curie temperature	$^{\circ}\text{C}$
T_{PC}	Post-curing temperature	$^{\circ}\text{C}$
V	Voltage	V
v	Wave velocity	m/s
Y	Young's modulus	Pa
α	Thermal expansion coefficient	$/^{\circ}\text{C}$
α^{Epoxy}	Thermal expansion coefficient of the epoxy	$/^{\circ}\text{C}$
α^{T-D}	Thermal expansion coefficient of the fiber	V/cm·Oe
λ	Magnetostrictive strain	ppm
λ_0	Spontaneous magnetostriction	ppm
λ_s	Saturation magnetostriction	ppm
μ_{rij}	Dynamic relative permeability component	–
μ_{rij}^{QS}	Quasistatic relative permeability component	–
v_f	Volume fraction	–
ω	Angular frequency	rad/s
ρ	Density	kg/m^3

List of Figure Captions

		<i>Page</i>
Fig. 1.1	Magnetic induction (B) versus magnetic field strength (H) for a theoretical ferromagnetic material. This B – H relation is called hysteresis loop.	3
Fig. 1.2	Magnetization (M) versus applied field (H) for a theoretical ferromagnetic material.	6
Fig. 1.3	Transition of magnetic moments at a 180° domain wall moving to the right under the influence of an applied H field pointed up.	10
Fig. 1.4	(a) Spheres used to model isotropic, disordered material behavior in the paramagnetic phase at $T > T_C$. (b) Ellipsoids representing the isotropic, ordered ferromagnetic domains at $T < T_C$, leading to λ_o . (c) λ_S and ε due to the maximal alignment of the ferromagnetic domains in the H direction.	13
Fig. 1.5	Technical saturation magnetostriction ($\lambda_S = \Delta\ell_S / \ell$) caused by a saturating H .	15
Fig. 1.6	Magnetization and magnetostriction processes with applied H fields.	17
Fig. 1.7	Graphical representations of the initial (a) magnetization (M) and (b) magnetostriction (λ) with applied H fields.	18
Fig. 1.8	(a) Ellipsoids for the isotropic, ordered ferromagnetic domains at $T < T_C$. λ_S is produced in the applied H direction due to the maximal alignment of the ferromagnetic domains. (b) σ -induced negative strain ($= -\lambda_S/2$) due to the maximal production of the available 90° domain walls in the material. (c) Total allowable strain ($= 3\lambda_S/2$) due to the complete motion of the available 90° domain walls under a saturating H and an optimal σ .	19



Fig. 1.9	A typical λ - H plot showing the combined effect of the external stress loading and applied H fields on a magnetostrictive material.	20
Fig. 1.10	λ - H plot of a monolithic Terfenol-D rod measured at various constant stress loadings from 0 to 18.9 MPa.	21
Fig. 1.11	The evolution of magnetostrictive materials from 1842 to 2002.	22
Fig. 1.12	Crystallographic structure of Terfenol-D.	29
Fig. 1.13	Schematic diagram of a laminated composite.	31
Fig. 1.14	Schematic diagrams of (a) a particulate composite and (b) a particulate-chain composite.	33
Fig. 1.15	A short-fiber composite and its needle-shaped, [112]-oriented Terfenol-D short fibers.	34
Fig. 2.1	Photograph of an [112]-textured monolithic Terfenol-D plate with dimensions 45 mm long, 30 mm wide, and 1 mm thick.	41
Fig. 2.2	A commercial wire electrical discharge machining (WEDM) equipment used to prepare our [112]-oriented Terfenol-D continuous fibers.	44
Fig. 2.3	An as-supplied monolithic Terfenol-D plate (left) and WEDM-processed, [112]-oriented Terfenol-D continuous fibers of 45 mm long and (1 mm \times 1 mm) cross-section (right).	44
Fig. 2.4	Scanning electron micrograph (SEM) showing three pieces of [112]-oriented Terfenol-D continuous fibers after the WEDM and cleaning processes. The WEDM process is well-controlled so that the edges of the fibers are quite smooth without obvious chipping.	45
Fig. 2.5	Quasistatic magnetostrictive strain (λ) as a function of applied magnetic field (H_3^{OS}) for an as-supplied monolithic Terfenol-D plate and a continuous fibers measured at 0.1 Hz frequency, room temperature, and zero stress loading.	46



Fig. 2.6	Optical micrograph of [112]-oriented Terfenol-D short fibers for 4 mm long and (1 mm × 1 mm) cross-section.	47
Fig. 2.7	Scanning electron micrograph (SEM) of ball-milled, irregularly shaped, randomly oriented Terfenol-D particles with poly-distributed sizes of 10–300 μm.	48
Fig. 2.8	Schematic diagram of the fabrication of epoxy-bonded Terfenol-D continuous-fiber composites.	51
Fig. 2.9	The family of the fabricated epoxy-bonded Terfenol-D continuous-fiber composites.	52
Fig. 2.10	Schematic diagram of the fabrication of epoxy-bonded Terfenol-D short-fiber and particulate-chain composites.	54
Fig. 3.1	Photographs of the in-house automated quasistatic measurement system.	57
Fig. 3.2	Schematic diagram of the in-house automated quasistatic measurement system in Fig. 3.1.	57
Fig. 3.3	Photograph showing (a) a continuous-fiber composite sample with a strain gauge for the strain-field ($\lambda - H_3^{QS}$) measurement and (b) another sample with a search coil for the flux-field ($B_3^{QS} - H_3^{QS}$) measurement.	59
Fig. 3.4	$\lambda - H_3^{QS}$ curves for continuous-fiber composites with different ν_f for $T_{PC} =$ (a) 30, (b) 40, (c) 50, (d) 60, (e) 70, and (f) 80 °C. The $\lambda - H_3^{QS}$ curve for monolithic Terfenol-D is also enclosed for comparison.	61
Fig. 3.5	$\lambda - H_3^{QS}$ curves for continuous-fiber composites with different T_{PC} for $\nu_f =$ (a) 0.2, (b) 0.3, (c) 0.4, (d) 0.5, (e) 0.6, and (f) 0.7. The $\lambda - H_3^{QS}$ curve for monolithic Terfenol-D is also enclosed for comparison.	65

- Fig. 3.6 $\lambda - H_3^{QS}$ curves for continuous-fiber composites ($T_{PC} = 80$ °C) and monolithic Terfenol-D. This is a zoom-in plot of Fig. 3.4(f) for $H_3^{QS} \leq 200$ kA/m. The arrows are drawn to indicate the magnetization jumping region characterized by the non-180° domain wall motion. 69
- Fig. 3.7 $\lambda - H_3^{QS}$ curves for continuous-fiber composite, monolithic Terfenol-D, short-fiber composite, and particulate-chain composite. All the composites have the same ν_f of 0.5 and been post-cured at 80 °C. 71
- Fig. 3.8 λ_s versus ν_f for continuous-fiber composites ($\nu_f = 0.2 - 0.7$) at different T_{PC} , monolithic Terfenol-D, short-fiber composite ($\nu_f = 0.5$) at $T_{PC} = 80$ °C, particulate-chain composite ($\nu_f = 0.5$) at $T_{PC} = 80$ °C, and epoxy, where the symbols and lines represent the experimental and calculated data, respectively. 73
- Fig. 3.9 $d_{33}^{QS} - H_3^{QS}$ curves for continuous-fiber composites with different T_{PC} of 30 to 80 °C for $\nu_f =$ (a) 0.2, (b) 0.3, (c) 0.4, (d) 0.5, (e) 0.6, and (f) 0.7. 74
- Fig. 3.10 $d_{33\max}^{QS}$ versus ν_f for continuous-fiber composites ($\nu_f = 0.2 - 0.7$) at different T_{PC} , monolithic Terfenol-D, short-fiber composite ($\nu_f = 0.5$) at $T_{PC} = 80$ °C, particulate-chain composite ($\nu_f = 0.5$) at $T_{PC} = 80$ °C, and epoxy, where the symbols and lines represent the experimental and calculated data, respectively. 77
- Fig. 3.11 $B_3^{QS} - H_3^{QS}$ loops of continuous-fiber composites ($T_{PC} = 80$ °C) and monolithic Terfenol-D. 79
- Fig. 3.12 B_{3s}^{QS} versus ν_f for continuous-fiber composites, Terfenol-D, and epoxy. The symbols and line represent the experimental data and fitted curve, respectively. 79

- Fig. 3.13 μ_{r33}^{QS} versus H_3^{QS} for continuous-fiber composites ($T_{PC} = 80$ °C) and monolithic Terfenol-D. 81
- Fig. 3.14 $\mu_{r33\max}^{QS}$ versus ν_f for continuous-fiber composites, Terfenol-D, and epoxy. The symbols and line represent the experimental data and fitted curve, respectively. 81
- Fig. 3.15 $M_3^{QS} - H_3^{QS}$ loops of continuous-fiber composites ($T_{PC} = 80$ °C) and monolithic Terfenol-D. 83
- Fig. 3.16 M_{3s}^{QS} versus ν_f for continuous-fiber composites, Terfenol-D, and epoxy. The symbols and line represent the experimental data and calculated data, respectively. 83
- Fig. 3.17 λ versus M_3^{QS} for continuous-fiber composites and monolithic Terfenol-D. 85
- Fig. 3.18 Normalized magnetostriction versus magnetization curves for continuous-fiber composites and monolithic Terfenol-D. 86
- Fig. 3.19 Comparison between the experimental λ_S obtained in Fig. 3.8 and the modeled λ_S based on Eq. (3.12) with the parameters summarized in Table 3.1. 90
- Fig. 3.20 Thermal-induced residual compressive stress (σ_T) as a function of volume fraction of Terfenol-D fibers (ν_f). 91
- Fig. 4.1 Schematic diagram of the in-house automation dynamic measurement system. 92
- Fig. 4.2 μ_{r33} versus f at different H_{Bias} for continuous-fiber composites with (a) $\nu_f = 0.2$, (b) $\nu_f = 0.3$, (c) $\nu_f = 0.4$, (d) $\nu_f = 0.5$, (e) $\nu_f = 0.6$, and (f) $\nu_f = 0.7$, together with (g) monolithic Terfenol-D, (h) short-fiber composite ($\nu_f = 0.5$), and (i) particulate-chain composite ($\nu_f = 0.5$). 95

- Fig. 4.3 d_{33} versus f at different H_{Bias} for continuous-fiber composites 101
with (a) $\nu_f = 0.2$, (b) $\nu_f = 0.3$, (c) $\nu_f = 0.4$, (d) $\nu_f = 0.5$, (e) $\nu_f = 0.6$, and (f) $\nu_f = 0.7$, together with (g) monolithic Terfenol-D, (h) short-fiber composite ($\nu_f = 0.5$), and (i) particulate-chain composite ($\nu_f = 0.5$).
- Fig. 4.4 μ_{r33} measured at 1 kHz as a function of H_{Bias} for continuous- 107
fiber composites ($\nu_f = 0.2 - 0.7$), monolithic Terfenol-D, short-fiber composite ($\nu_f = 0.5$), and particulate-chain composite ($\nu_f = 0.5$).
- Fig. 4.5 Dependence of E_3^H and E_3^B on H_{Bias} for continuous-fiber 109
composites ($\nu_f = 0.2 - 0.7$), monolithic Terfenol-D, short-fiber composite ($\nu_f = 0.5$), and particulate-chain composite ($\nu_f = 0.5$).
- Fig. 4.6 d_{33} measured at 1 kHz as a function of H_{Bias} for continuous- 110
fiber composites ($\nu_f = 0.2 - 0.7$), monolithic Terfenol-D, short-fiber composite ($\nu_f = 0.5$), and particulate-chain composite ($\nu_f = 0.5$).
- Fig. 4.7 k_{33} measured at 1 kHz as a function of H_{Bias} for continuous- 112
fiber composites ($\nu_f = 0.2 - 0.7$), monolithic Terfenol-D, short-fiber composite ($\nu_f = 0.5$), and particulate-chain composite ($\nu_f = 0.5$).
- Fig. 4.8 ν_f dependence of μ_{r33} at $H_{Bias} = 40$ kA/m for continuous- 113
fiber composites ($\nu_f = 0.2 - 0.7$), monolithic Terfenol-D, short-fiber composite ($\nu_f = 0.5$), and particulate-chain composite ($\nu_f = 0.5$), where the symbols and line represent the experimental and calculated data, respectively.



Fig. 4.9	Variation of E_3^H with ν_f at $H_{Bias} = 40$ kA/m for continuous-fiber composites ($\nu_f = 0.2 - 0.7$), monolithic Terfenol-D, short-fiber composite ($\nu_f = 0.5$), and particulate-chain composite ($\nu_f = 0.5$), where the symbols and lines represent the experimental and calculated data, respectively.	115
Fig. 4.10	ν_f dependence of d_{33} at $H_{Bias} = 40$ kA/m for continuous-fiber composites ($\nu_f = 0.2 - 0.7$), monolithic Terfenol-D, short-fiber composite ($\nu_f = 0.5$), and particulate-chain composite ($\nu_f = 0.5$), where the symbols and lines represent the experimental and calculated data, respectively.	116
Fig. 4.11	ν_f dependence of k_{33} at $H_{Bias} = 40$ kA/m for continuous-fiber composites ($\nu_f = 0.2 - 0.7$), monolithic Terfenol-D, short-fiber composite ($\nu_f = 0.5$), and particulate-chain composite ($\nu_f = 0.5$), where the symbols and lines represent the experimental and calculated data, respectively.	118
Fig. 5.1	Conceptual design of the smart TVA.	124
Fig. 5.2	Simplified dynamic model for the conceptual design.	126
Fig. 5.3	Graphical illustration of the relationship between the frequency ratio (f / f_o), magnetic field ratio (H / H_{cr}) and force ratio (F / F_{cr}) of the smart TVA shown in Fig.5.1.	129
Fig. 5.4	A smart TVA prototype.	130
Fig. 5.5	Assembly diagram of the PE-MS sensor/actuator.	131
Fig. 5.6	Measurement setup for characterization of the smart TVA.	134
Fig. 5.7	Measured FRFs on the TVA under various magnetic tuning fields.	135
Fig. 5.8	Measured (symbol) and predicted (solid line) natural frequencies and predicted axial force (dotted line) as a function of dc tuning magnetic field.	136
Fig. 5.9	FRFs measured using the PE patch sensors and a commercial accelerometer at (a) 350 and (b) 690 Oe.	137



Fig. 5.10	PE patch sensor output signals at different dc tuning magnetic fields in response to a simulated resonance at 58 Hz.	138
Fig. 5.11	Test bed for vibration control using smart TVA.	139
Fig. 5.12	Measured FRFs for vibration control.	140
Fig. 5.13	Schematic diagram of the generic structure of magnetostrictive driver	144
Fig. 5.14	Explode view of a 64 kHz Terfenol-D composite transducer	146
Fig. 5.15	Meshed 2D magnetic simulation drawing	149
Fig. 5.16	Simulation result of magnetic field distribution analysis (a) without flux guide, (b) with flux guide	150
Fig. 5.17	Comparison between with and without magnetic flux guide	151
Fig. 5.18	Harmonic analysis result in x-, y- and z-axis displacement	155
Fig. 5.19(a)	3D design of front slab and back slab	156
Fig. 5.19(b)	Design of Terfenol-D composite and NdFeB permanent magnet	157
Fig. 5.19(c)	Design of solenoid, magnetic flux guide and external flux guide	157
Fig. 5.20	Terfenol-D continuous fiber composite, front slab and back slab	158
Fig. 5.21	Continuous-fiber composite transducer	158
Fig. 5.22	Electrical characteristic of transducer from 55 kHz to 80 kHz	160
Fig. 5.23	Strain coefficient against frequencies for 14mm long composite transducer	162



List of Table Captions

		<i>Page</i>
Table 2.1	Material properties of the monolithic Terfenol-D in Fig. 2.1 provided by the manufacturer.	41
Table 2.2	Process parameters of the WEDM in Fig. 2.2 for our Terfenol-D fibers.	44
Table 2.3	Some of the important material properties of Ciba-Geigy Araldite LY564/HY2954 epoxy at room temperature.	50
Table 2.4	Description of the fabricated continuous-fiber composites with dimensions 45 mm long and (12 mm × 12 mm) cross-section.	51
Table 3.1	Analytical model parameters.	91
Table 5.1	Some important geometric and material parameters of the MS composite actuator used in the sensor/actuator.	132
Table 5.2	Some important geometric and material parameters of the flexible beams-mounting frame structure.	132
Table 5.3	Magnetic Properties of the transducer for simulation.	148
Table 5.4	Material properties of the continuous-fiber composite for simulation.	152
Table 5.5	Material properties of the transducer parts for simulation.	153



Chapter 1

Introduction

1.1 Magnetism

The phenomenon of magnetostriction can be regarded as an intrinsic coupling between the magnetic and mechanical states of a ferromagnetic material [1]. Hence, an understanding of basic magnetism forms an introduction to ferromagnetic materials in general and to magnetostrictive materials in specific. In this section, a brief overview of magnetism, including the fundamentals of magnetic fields, magnetization and magnetization processes, is provided to facilitate the subsequent discussion of magnetostrictive materials and devices. For the purpose of this study, the overview is directed to ferromagnetic materials, which are characterized by the presence of a domain structure having nonzero spontaneous magnetization at temperatures below their paramagnetic-ferromagnetic phase transition temperatures called Curie temperatures (T_C). Typical materials of this class include the traditional transition metals: iron, steel, nickel, cobalt, and the giant magnetostrictive alloy: Terfenol-D ($\text{Tb}_{0.3}\text{Dy}_{0.7}\text{Fe}_{1.92}$).

The basis for the macroscopic effects of magnetism in ferromagnetic materials lies on the alignment of magnetic moments produced by the orbital motion of electrons around the nucleus and the spin of electrons about their own axis [2]. These materials exhibit an isotropic, disordered behavior in the paramagnetic (high-temperature) phase above T_C due to the random alignment of the atomic magnetic moments. As the materials are cooled through T_C , they show an isotropic, ordered



behavior in the ferromagnetic (low-temperature) phase so that alignment of the atomic magnetic moments results and allows a net magnetization at the macroscopic level [3].

1.1.1 Magnetic Fields

Magnetism at the macroscopic level is usually described by the presence and effects of magnetic fields: namely, magnetic field strength (H) (or H field for short) and magnetic induction (B) (or B field for short). These fields can be conceptualized as a spatial energy gradient with both magnitude and direction [4]. H is a physical quantity describing the generation of magnetic field due to moving electric charges. It can be measured using a Hall device and presented in SI units as ampere/meter (A/m) or in CGS units as Oersted (Oe). B is also a measurable physical quantity delineating the magnetic flux density due to an applied H . It can be evaluated by wrapping a search coil of N loops and area A around the sample and acquiring the time integral of the voltage induced in the search coil ($V_{Induced}$) based on the Faraday-Lenz law [5]:

$$V_{Induced} = -NA \frac{dB}{dt}. \quad (1.1)$$

B is given in Tesla (T), where $1 \text{ T} = 1 \text{ Henry} \cdot \text{ampere/meter}^2$ (H·A/m²) for the SI system or in Gauss (G) for the CGS system. The conversions between CGS and SI units for H and B are as follows:

$$1 \text{ Oe} = 1000 / 4 \pi \sim 79.58 \text{ A/m},$$

$$1 \text{ G} = 10^{-4} \text{ T}.$$

An establishment of the relationship between B and H is the first step to investigate the magnetic properties of a ferromagnetic material. Figure 1.1 shows a plot of B versus H with the typical sigmoid characteristic of many ferromagnetic

materials. This nonlinear and hysteretic (sigmoid) characteristic has to be interpreted as a multi-valued map rather than a function. Nevertheless, the relation of B and H can generally be established by the permeability of the material (μ) with units of H/m (SI) or G/Oe (CSG) as follows:

$$B = \mu H = \mu_o \mu_r H , \tag{1.2}$$

where μ_o is the permeability of free space ($= 4 \pi \times 10^{-7}$ H/m) and μ_r is the relative permeability of the material. It is noted that μ_r is greater than, less than, and equal to unity for paramagnetic, diamagnetic, and nonmagnetic materials, respectively.

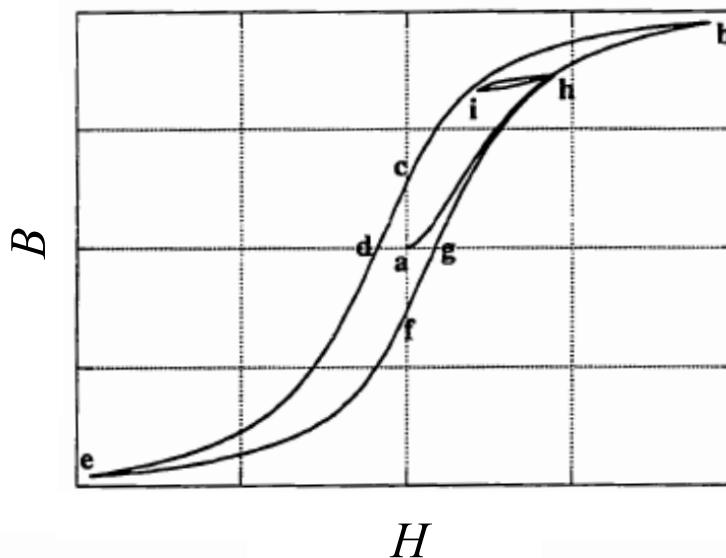


Fig. 1.1 Magnetic induction (B) versus magnetic field strength (H) for a theoretical ferromagnetic material. This B - H relation is called hysteresis loop [6].

Referring to Fig. 1.1, the initial application of an H field to a demagnetized ferromagnetic material increases B from point 'a' with an initial slope of μ_{int} called initial (differential) permeability. As H is increased to point 'b', the material becomes completely magnetized with saturation magnetic induction (B_S) and slope $\mu \sim \mu_o$ (i.e.,



$\mu_r \sim 1$). After H is reduced to zero, a residual B remains at point ‘c’ and is denoted as remanent magnetic induction (B_R). As the direction of H is reversed, the magnitude required to force the residual B from point ‘c’ to zero at point ‘d’ is the coercive field (H_C). As the magnitude of H further increases in the negative direction, the material is again magnetically saturated at point ‘e’ with negative B_S . An equivalent remanence B_R at point ‘f’ and an equivalent coercivity H_C at point ‘g’ are encountered when H is positively increased from point ‘e’. If H is kept cycling, the same trajectory ‘b’ \rightarrow ‘c’ \rightarrow ‘d’ \rightarrow ‘e’ \rightarrow ‘f’ \rightarrow ‘g’, known as the B – H hysteresis loop, will be traced out as long as all the conditions remain unchanged. The initial trajectory ‘a’ \rightarrow ‘b’ will not be followed unless the material is demagnetized and the above process is started again from the demagnetized state.

An interesting feature of the B – H hysteresis loop (Fig. 1.1) is that it shows the dependence of the current magnetic state of the material on its history. This means that the future magnetic state of the material is dependent not only on the current magnetic state but also on the previous magnetic history of how the material was magnetized. For example, the material remembers the initial trajectory ‘a’ \rightarrow ‘b’ and proceeds the subsequent trajectory ‘b’ \rightarrow ‘c’ \rightarrow ‘d’ \rightarrow ‘e’ \rightarrow ‘f’ \rightarrow ‘g’. This magnetic memory is a fascinating feature of ferromagnetic materials with great application values.

The “major” B – H hysteresis loop depicted in Fig. 1.1 with trajectory ‘b’ \rightarrow ‘c’ \rightarrow ‘d’ \rightarrow ‘e’ \rightarrow ‘f’ \rightarrow ‘g’ essentially describes the relationship between B and H for large symmetric H . If such a cyclic H with significantly reduced amplitude is used in conjunction with a static (or bias) H , an asymmetric “minor” B – H hysteresis loop



similar to the turnaround points ‘h’ and ‘i’ is traversed. While the shape and nominal slope of the “minor” B – H hysteresis loop varies considerably with the cyclic H , this “minor” loop exhibits closure in nearly all cases since its return leg takes it back through the initial turnaround points. The magnetic memory of the “minor” loop is “wiped out” in essence. In fact, these “major” and “minor” B – H hysteresis loops constitute the quasistatic and dynamic magnetic properties of our magnetostrictive composites to be described in Chapter 3 and Chapter 4, respectively.

1.1.2 Magnetization

In ferromagnetic materials, the magnetic moments are permanently aligned in regions known as domains. The net result of the moment alignment is a magnetization (M), defined as the magnetic moments per unit volume [7]. The domain magnetization is a constant for the material depending on the atomic structure. When the magnetic moments of these domains are randomly oriented, the net magnetization in the material is zero and the material is said to be in its demagnetization state. The application of an external H field to the material aligns collections of magnetic moments into one or more domains, resulting in a net magnetization. The action and dynamics of these magnetic domains provide the basic processes for the magnetization (and magnetostriction) of the material to be described in Section 1.1.3.

It is convenient to consider the magnetization of a ferromagnetic material as an intrinsic field resulting from ordering of magnetic domains in the material, which is distinct from the B and H fields described in Section 1.1.1. Physically, M is given in

A/m for the SI system and emu/c^3 for the CGS system. The relationship between B , H , and M can be expressed (for the SI system) as

$$B = \mu_0(H + M). \quad (1.3)$$

The magnetization hysteresis (M - H) loop shown in Fig 1.2 provides a measure of a ferromagnetic material and hence a key to modeling. It is noted that while the slope of the B - H loop approaches μ_0 as H becomes large in Fig. 1.1, the slope of the M - H loop goes to zero [8]. At points 'b' and 'e', M approaches saturation magnetization (M_S). This is referred to the technical saturation, which occurs when all the domain magnetizations are collinear with H and the material can be considered as a single domain. The "minor" B - H hysteresis loop (i.e., the turnaround points 'h' and 'i') in Fig. 1.1 that varies considerably with a dc-biased small cyclic H also leads to a corresponding "minor" M - H hysteresis loop with similar turnaround points 'h' and 'i' in Fig. 1.2.

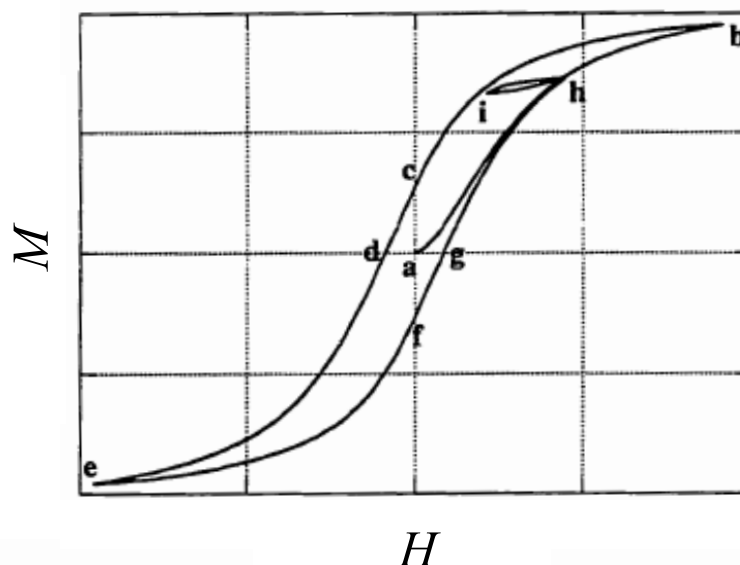


Fig. 1.2 Magnetization (M) versus applied magnetic field strength (H) for a theoretical ferromagnetic material [9].



1.1.3 Magnetization Processes

In order to minimize the magnetostatic energy of a ferromagnetic material, the magnetization breaks up into localized volumes or magnetic domains, where all the magnetic moments align parallel to one another. Within domains, the material is magnetically saturated with spontaneous magnetization (M_o). Domain alignment is often known as “long-range” order [10].

Since each domain has its M_o pointing in a direction different from its immediate neighbors, domains are separated by thin transition layers called domain walls. Domain walls can generally be classified by the 180° and non- 180° (e.g., 90°) domain walls where the magnetic moments undergo specific motions depending on whether the angle of spin rotation from the one domain to the other is near 180° or not [11].

The width of domain walls is determined by a delicate balance between the anisotropy energy and the Weiss-type interaction coupling energy of the atomic magnetic moments (also known as exchange interaction energy due to its quantum mechanical origin). The anisotropy tends to make walls thinner because the anisotropy energy is lowest when moments align along magnetically “easy” axes (such as the [100] axis in iron, the [111] axis in nickel, and the [111] in Terfenol-D). The interaction energy tends to make walls thicker since the interaction energy is minimized when magnetic moments are parallel.

In the demagnetized state ($M = 0$), ferromagnetic materials consist of a large number of domains oriented randomly in such a way that the vector sum of all the magnetization is zero. The domain orientations are in fact not exactly random; certain



crystallographic easy axes are more preferable. In the absence of an H field, the domains will find their energetically favorable to align along these axes because the total energy will be a minimum in such configuration. The application of an H field breaks the energy equilibrium and causes domains to rearrange, leading to a change in the total magnetization of the material. Paramagnetic materials also have permanent atomic magnetic moments, but they do not exhibit long-range alignment (i.e., their atomic magnetic moments are randomly aligned in the absence of an H field).

The magnetization processes of a ferromagnetic material can change reversibly or irreversibly with an H field. Reversible magnetization processes are energetically conservative since the material returns to its original magnetization state upon application and removal of the H field. On the other hand, irreversible magnetization processes are dissipative in such a way that an external restoring force has to be applied to bring the magnetization back to its original value. Experimental evidence on ferromagnetic materials indicates that reversible magnetization processes occur only for relatively small H increments and a transition towards irreversible magnetization processes occurs as H is increased to an intermediate level. This implies that both reversible and irreversible magnetization processes take place in most practical cases and the magnetization hysteresis loops similar to those in Figs. 1.1 and 1.2 appear as an H field is used.

The magnetization processes, either reversible or irreversible, can be explained by two interrelated mechanisms of domain wall motions. These mechanisms, including (1) the 180° domain wall motion and (2) the non- 180° domain wall motion, are discussed separately as follows [12].

(1) The 180° Domain Wall Motion:

With an applied H field, individual magnetic moments within domains rotate more easily into neighboring domains oriented close to the H direction than entire domains. This is because a fine balance between the anisotropy and exchange energies results in the directions of magnetic moments within the domain walls, whereas the magnetic moments are locked into particular directions by the interaction coupling in the body of the domains. A change in the field energy ($E = -\mu_o \vec{m} \cdot \vec{H}$) can then alter the energy balance in the wall and make the moments to rotate.

Consider the illustration of a 180° domain wall motion in Fig. 1.3. As a small H is applied in the direction shown, the magnetic moments within the unfavorably orientated domain will not change direction because they are at the bottom of a deep energy well associated with the strong exchange energy that holds the moments parallel. Within the domain wall, however, the magnetic energy is sufficient to tip the balance in favor of the direction of H . The magnetic moments originally located within the wall gradually rotate into the H direction, producing the effect of the domain wall ‘moving’ to the right. The domain wall is conventionally treated as an entity by itself so that its motion through the material is analyzed in terms similar to that of interfaces such as elastic membranes.

An additional factor that determines how domain walls move is the presence of inclusions or pinning sites such as crystal imperfection, stress concentration, voids, and cracks. Pinning sites act as an anchor to the walls

since magnetostatic energy decreases when domain walls attach to the pinning sites. The 180° domain wall motion is reversible at low to moderate H levels, in which the walls bow while remaining attached to pinning sites. The domain walls act in this case like a flexible membrane and so they return to the planar position upon removal of the H . As H is further increased, however, the domain wall energy overcomes the pinning energy and the wall deforms until it dislocates irreversibly from the pinning sites. In order to minimize the total energy, the wall translates and attaches to remote pinning sites where it will remain attached until additional energy is supplied to produce a dislocation. The energy lost to pinning as the domain walls translate itself in the form of magnetization hysteresis.

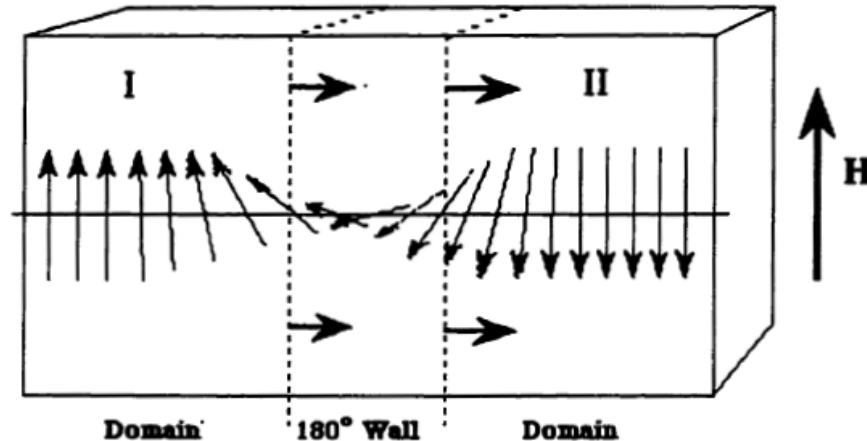


Fig. 1.3 Transition of magnetic moments at a 180° domain wall moving to the right under the influence of an applied H field pointed up.

(2) The Non- 180° Domain Wall Motion:

When the magnetization vector of an entire domain changes direction as a result of the competition between the anisotropy energy and the field



energy, the rotation of domains other than the movement of the 180° ones described above occurs. In fact, a substantial amount of field energy is necessary for the rotation to occur. At lower H levels, the direction of magnetization will only displace slightly from the original orientation, and reversible (coherent) rotation is achieved. When H levels are sufficiently high to overcome the (magnetocrystalline or stress) anisotropy energy, the domains rotate from their original easy axes closest to the H direction. Upon removal of the H , the magnetization will not return to the original configuration since magnetic moments will be trapped in energy wells associated with the easy axes. The magnetization processes are, in such circumstances, irreversible. Near saturation, the material behaves as a single domain with the magnetization vectors aligning along the H direction. The precession is due to thermal activation and becomes greater as the temperature increases. As H is further increased, the field energy overcomes the thermal energy and so the precession is reduced. As H is removed, the precession is re-established in a reversible way.

The term magnetic anisotropy refers to the dependence of magnetic properties on the direction in which they are measured. Anisotropy strongly affects the magnetization of materials, particularly the non- 180° domain wall motion, and thus has an important effect on magnetostriction. Magnetic anisotropy can be of several kinds, including magnetocrystalline anisotropy, stress anisotropy, and shape anisotropy.



1.2 Magnetostriction

Magnetostriction is a property of ferromagnetic materials describing shape changes or strain generation when subjected to an applied magnetic field [13]. In order to understand the phenomenon of magnetostriction, one must have a basic understanding of the magnetostriction processes, which are rooted in the interaction of electron spins and orbital angular momenta with the crystal lattice. Heavy rare earths of the lanthanide series, such as terbium (Tb) and dysprosium (Dy), exhibit large magnetic moments due to the strong coupling between their electron spins and orbital angular momenta. [14]. As a result, the lattice spacing and overall dimensions in these materials are strongly influenced by the states of magnetization. The fundamental magnetization of magnetostrictive materials involves regions of $10^{12} - 10^{18}$ atoms, which achieve common alignment of their magnetic moments to form magnetic domains through the long-range interaction, termed the Weiss mean field. The size and number of magnetic domains as well as their orientations are governed by the energy equilibrium between the magnetocrystalline anisotropy, elastic interaction, and applied fields [15].

In practice, the general term “magnetostriction” refers to strains generated during the paramagnetic-ferromagnetic phase transitions (T_C) [16] or in response to magnetization changes upon applied H fields below T_C with the constitution of magnetoelastic (or magnetomechanical) coupling. Three fundamental phenomena of interest are the spontaneous magnetostriction (λ_o), saturation magnetostriction (λ_s), and Joule magnetostriction (λ) below saturation.

1.2.1 Spontaneous Magnetostriction

The spontaneous magnetostriction (λ_o) quantifies strains generated and domains formed when a ferromagnetic material is cooled from its high-temperature paramagnetic phase through its T_C to its low-temperature ferromagnetic phase. Above T_C , thermal energy overcomes the Weiss mean field so that the alignment of magnetic moments is disrupted and the formation of magnetic domains is prevented. Below T_C , magnetic moments change from isotropic, disordered paramagnetic regions to ordered ferromagnetic domains. As shown in Fig. 1.4, the presence of λ_o is modeled using the isotropic, disordered paramagnetic regions by spheres for $T > T_C$ [Fig. 1.4(a)] and the still isotropic but ordered ferromagnetic domains by ellipsoids for $T < T_C$ [Fig. 1.4(b)]. If the total spontaneous strain is labeled as ε , the change in length due to the transition from a sphere to an ellipsoid with major axis at θ is

$$\varepsilon(\theta) = \varepsilon \cos^2 \theta, \tag{1.4}$$

and the spontaneous magnetostriction is

$$\lambda_o = \int_{-\pi/2}^{\pi/2} \varepsilon \cos^2 \theta \sin \theta d\theta = \frac{\varepsilon}{3}. \tag{1.5}$$

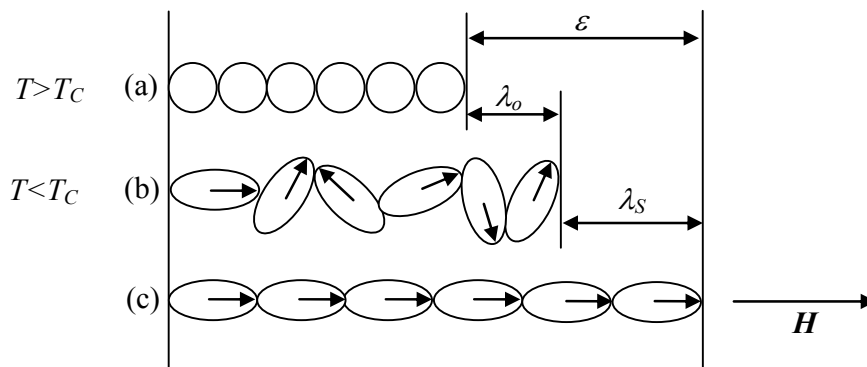


Fig. 1.4 (a) Spheres used to model isotropic, disordered material behavior in the paramagnetic phase at $T > T_C$. (b) Ellipsoids representing the isotropic, ordered ferromagnetic domains at $T < T_C$, leading to λ_o . (c) λ_s and ε due to the maximal alignment of the ferromagnetic domains in the H direction.



1.2.2 Saturation Magnetostriction

Besides the effect of temperature, the use of an external H field also manifests magnetostriction. Referring to Fig. 1.4(c), when the ordered ferromagnetic domains in the material are maximally aligned along the H direction, saturation magnetostriction (λ_S) is produced. In the macroscopic perspective, this λ_S indicates the maximal expansion in length ($\Delta\ell_S$) of a magnetostrictive material due to saturation magnetization (M_S) divided by the original length (i.e., $\lambda_S = \Delta\ell_S / \ell$) as illustrated in Fig. 1.5. This λ_S , together with λ_o , gives rise to the total allowable strain (ε) in the material (Fig. 1.4) as follows:

$$\varepsilon = \lambda_o + \lambda_S. \quad (1.6)$$

From Eqs. (1.5) and (1.6), we have

$$\lambda_S = \varepsilon - \lambda_o = \frac{2}{3} \varepsilon. \quad (1.7)$$

Hence, the values of ε and λ_o can be deduced for a given λ_S .

In fact, the behavior of λ_S depends on both the anisotropy of the material and the angle θ at which it is measured relative to H . Combining Eqs. (1.4) – (1.7) yields

$$\lambda_S(\theta) = \frac{3}{2} \lambda_S \left(\cos^2 \theta - \frac{1}{3} \right), \quad (1.8)$$

Equation (1.8) quantifies λ_S at an angle θ from H . It is noted that Eq. (1.8) has parallel saturation magnetostriction ($\lambda_{S//}$) of λ_S at $\theta = 0^\circ$ and perpendicular saturation magnetostriction ($\lambda_{S\perp}$) of $-\lambda_S / 2$ at $\theta = 90^\circ$, giving an ultimate ε in agreement with Eq. (1.7) as follows:

$$\varepsilon = \lambda_{S//} - \lambda_{S\perp} = \frac{3}{2} \lambda_S. \quad (1.9)$$

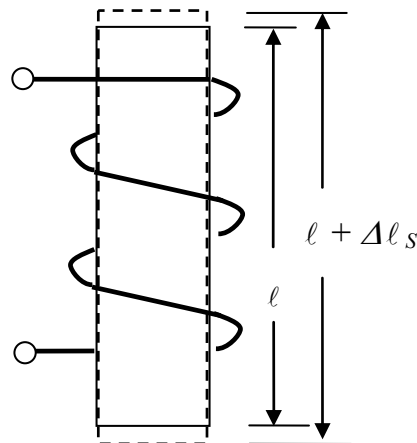


Fig. 1.5 Technical saturation magnetostriction ($\lambda_S = \Delta\ell_S / \ell$) caused by a saturating H .

1.2.3 Joule Magnetostriction

The Joule magnetostriction (λ) characterizes intermediate strains due to non-saturating H [17]. It is the magnetostrictive property of ferromagnetic materials that provides them with actuator applications. In general, λ is more difficult to be quantified since these intermediate strains are highly dependent on magnetization states and the underlying crystalline structure. One case that can be directly quantified is that of strains due to 90° domain rotation which is typically a result of either magnetocrystalline or stress anisotropy. An example of the former is the moment rotation in a uniaxial compound in response to an H applied perpendicular to the easy axis. The second case is important to transducer and actuator designs which employ external stress loading (or prestress) mechanisms, for instance, tensile stresses in nickel or compressive stresses in Terfenol-D, so as to overcome magnetocrystalline anisotropy and orient moments perpendicular to H for facilitating the maximal degree of 90° (or non- 180° in general) domain wall motion. To model the strains due to the domain rotation, Eqs. (1.4) and (1.7) are combined to yield



$$\lambda(\theta) = \frac{3}{2} \lambda_s \cos^2 \theta. \quad (1.10)$$

Following the relation

$$M = M_s \cos \theta, \quad (1.11)$$

we have

$$\frac{\lambda}{\lambda_s} = \frac{3}{2} \left(\frac{M}{M_s} \right)^2. \quad (1.12)$$

Hence, λ exhibit a quadratic dependence on M .

1.2.4 Magnetization and Magnetostriction Processes

Taking a closer and combined look at the magnetization and magnetostriction processes of a magnetostrictive material in a plane parallel to the easy axis, Fig. 1.6 shows the progression from the demagnetized state to the saturation as an H field is applied in the longitudinal direction of the material. Stage '0' in Fig. 1.6 represents the initial condition where the material is in a demagnetized state. The magnetic domain vectors are not collectively oriented and sum to zero magnetization. Upon application of a relatively small H in Stage '1', domains more closely aligned with H grow at the expense of less favorably oriented domains. This phenomenon, which mainly results in M but not in λ , is dominated by the 180° domain wall motion (Section 1.1.3). As H is increased further, Stage '2' is reached, where the material becomes one domain rotating into alignment with the easy axis, giving rise to both M and λ . This phenomenon is preferably described by the non- 180° domain wall motion (Section 1.1.3). Completing the magnetization and magnetostriction processes, Stage

'3' develops with an additional increment in H . At this point, technical saturation is reached.

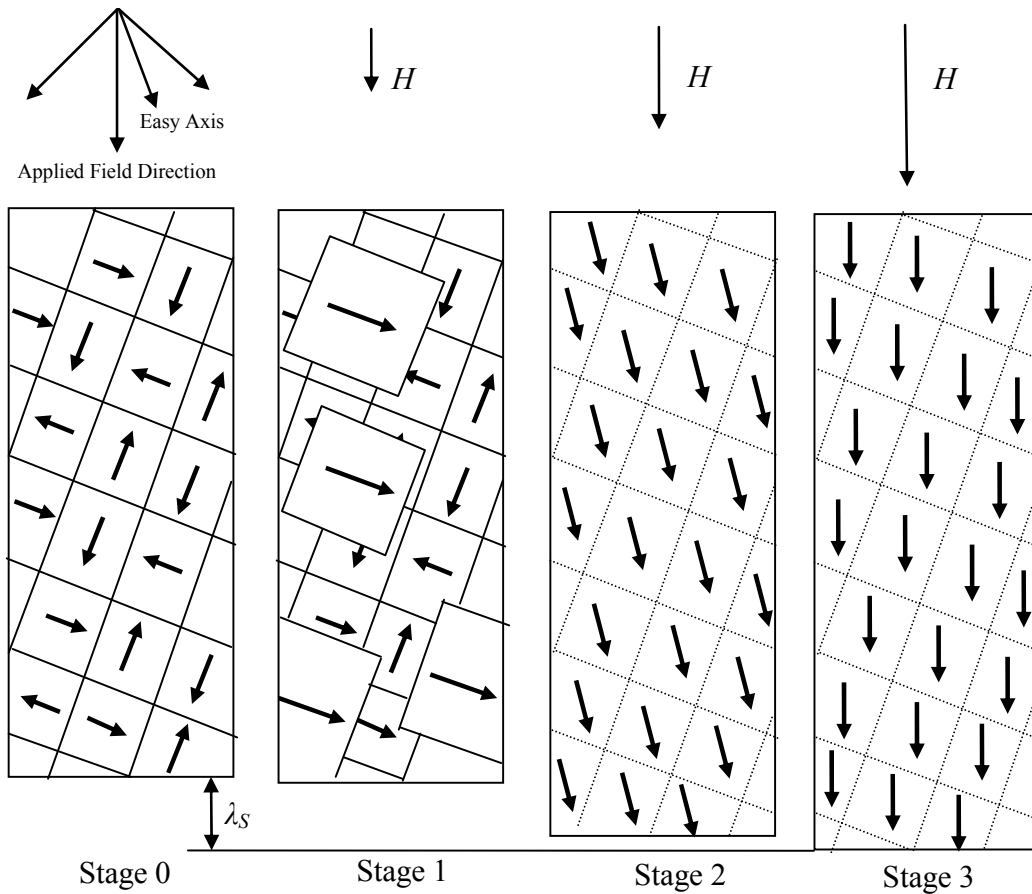


Fig. 1.6 Magnetization and magnetostriction processes with applied H fields.

The initial magnetization and magnetostriction processes of the material shown in Fig. 1.6 are presented in a graphical format in Fig. 1.7. In Stage '1', as M slowly increases from zero with the motion of the relatively preferable 180° domain walls so that λ remains comparatively ineffective. Stage '2' follows with the rapid development of M and λ as a result of the contribution of the available non- 180° domain wall motion, leading to the obvious burst regions of the magnetization and magnetostrictive processes. In Stage '3', M and λ increase at a diminishing rate after

reaching their technical saturations M_s and λ_s . Beyond these technical saturations, only slight increases in M and λ occur as magnetic moments are forced out of procession into complete alignment with H . As a general rule of thumb, the initial 180° domain wall motion produces M without accompanying λ , while the later non- 180° domain wall motion produces changes in both M and λ .

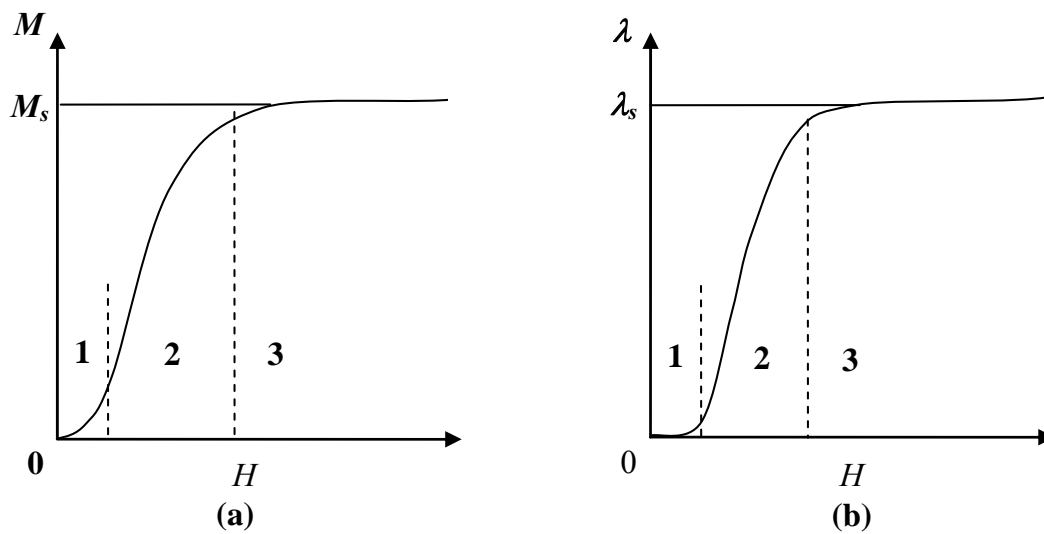


Fig. 1.7 Graphical representations of the initial (a) magnetization (M) and (b) magnetostriction (λ) with applied H fields.

Following the effect of applied H fields described in Figs. 1.4 – 1.7, Fig. 1.8 relates the combined effect of external stress loadings and applied H fields on a magnetostrictive material at $T < T_C$. The isotropic but ordered ferromagnetic domains, which are depicted as ellipsoids in Fig. 1.4(b), are now re-presented in Fig. 1.8(a). In the absence of external stress loadings, these ordered ferromagnetic domains are capable of producing λ_s in the material when they are maximally aligned along the H direction [Figs. 1.4(c) and 1.8(a)]. Now, when an optimal external stress loading (σ) is applied along the longitudinal direction of the material (also the H direction) without

involving any H field [Fig. 1.8(b)], the ordered ferromagnetic domains in Fig. 1.8(a) will be maximally aligned perpendicular to the H direction, leading to a σ -induced compressive strain of $-\lambda_s/2$. This negative strain is owed to the maximal production of 90° domain walls in the material. When the material is subject to a saturating H under such an optimal σ , the total allowable strain (ε) will be as high as $3\lambda_s/2$ [Fig. 1.8(c)]. It is important to note that this ε represents the resultant of the first σ -induced strain ($= -\lambda_s/2$) and the latter H -induced strain ($= \lambda_s$) due to the complete motion of the available 90° domain walls. Figure 1.9 provides an illustration of λ - H plot for the combined effect of the external stress loadings and applied H fields on the material [18].

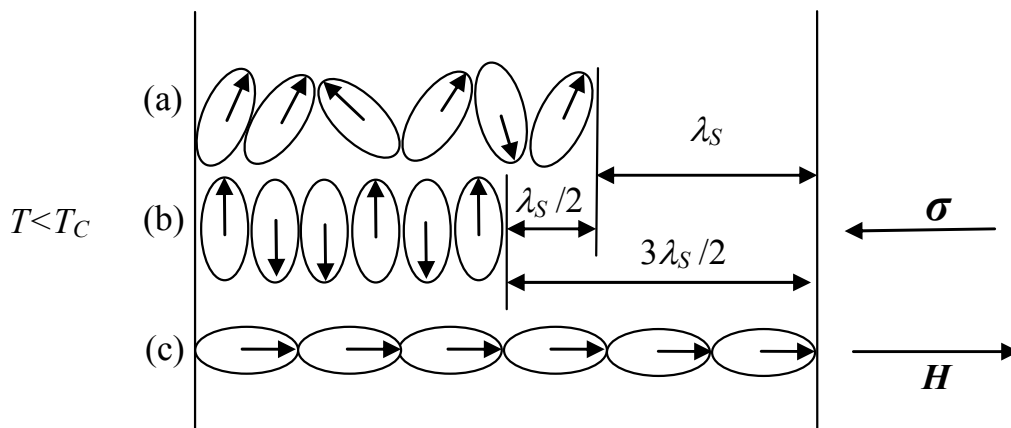


Fig. 1.8 (a) Ellipsoids for the isotropic, ordered ferromagnetic domains at $T < T_C$. λ_s is produced in the applied H direction due to the maximal alignment of the ferromagnetic domains. (b) σ -induced negative strain ($= -\lambda_s/2$) due to the maximal production of the available 90° domain walls in the material. (c) Total allowable strain ($= 3\lambda_s/2$) due to the complete motion of the available 90° domain walls under a saturating H and an optimal σ .

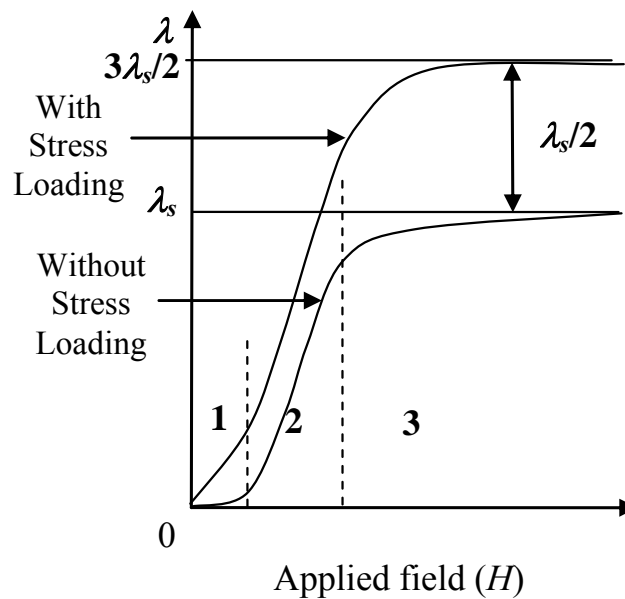


Fig. 1.9 A typical λ - H plot showing the combined effect of the external stress loading and applied H fields on a magnetostrictive material.

Figure 1.10 shows the λ - H plot of a monolithic Terfenol-D rod measured at various constant stress loadings from 0 to 18.9 MPa [19]. It is clear that when the material is not compressed as in Fig. 1.4(c) or Fig. 1.8(a), the magnetostrictive strain saturates at about 1150 ppm. When the stress loading is increased to 7.6 MPa, the saturation strain increases to about 1650 ppm. Further increase in the stress loading to 18.9 MPa does not substantially increase the saturation strain output; it just goes up slightly to about 1800 ppm as in Fig. 1.8(c). Nevertheless, the stress loading in the range of 7.6 to 18.9 MPa can effectively increase the saturation strain output by a factor of about 3/2 compared to the case without stress loading [19, 20].

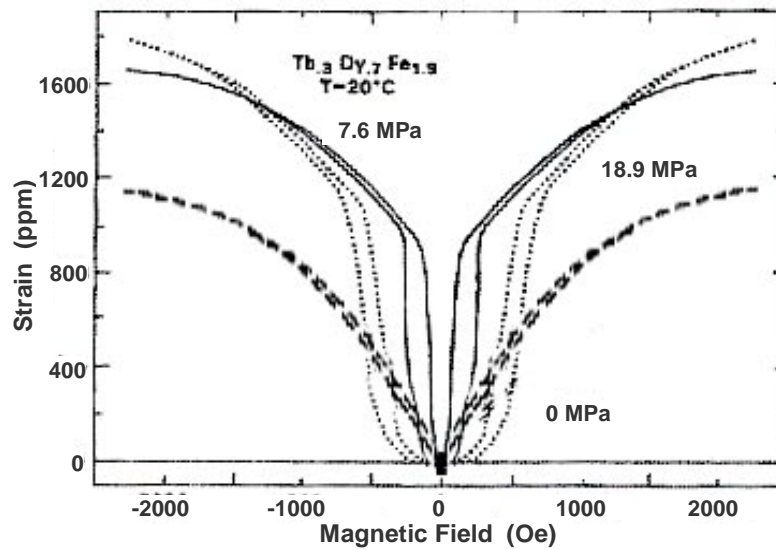


Fig. 1.10 λ - H plot of a monolithic Terfenol-D rod measured at various constant stress loadings from 0 to 18.9 MPa [19].

1.3 Review of Magnetostrictive Materials

Figure 1.11 shows the evolution of magnetostrictive materials from 1842 to 2002. The evolutionary stage essentially goes through various important types of magnetostrictive materials, including transition metals, rare earth single crystals, rare earth-iron alloys, Terfenol-D, and epoxy-bonded Terfenol-D composites. The epoxy-bonded Terfenol-D composites can generally be classified into laminated composites, particulate and particulate-chain composites, and short-fiber composites. The development of these materials is reviewed in this section.

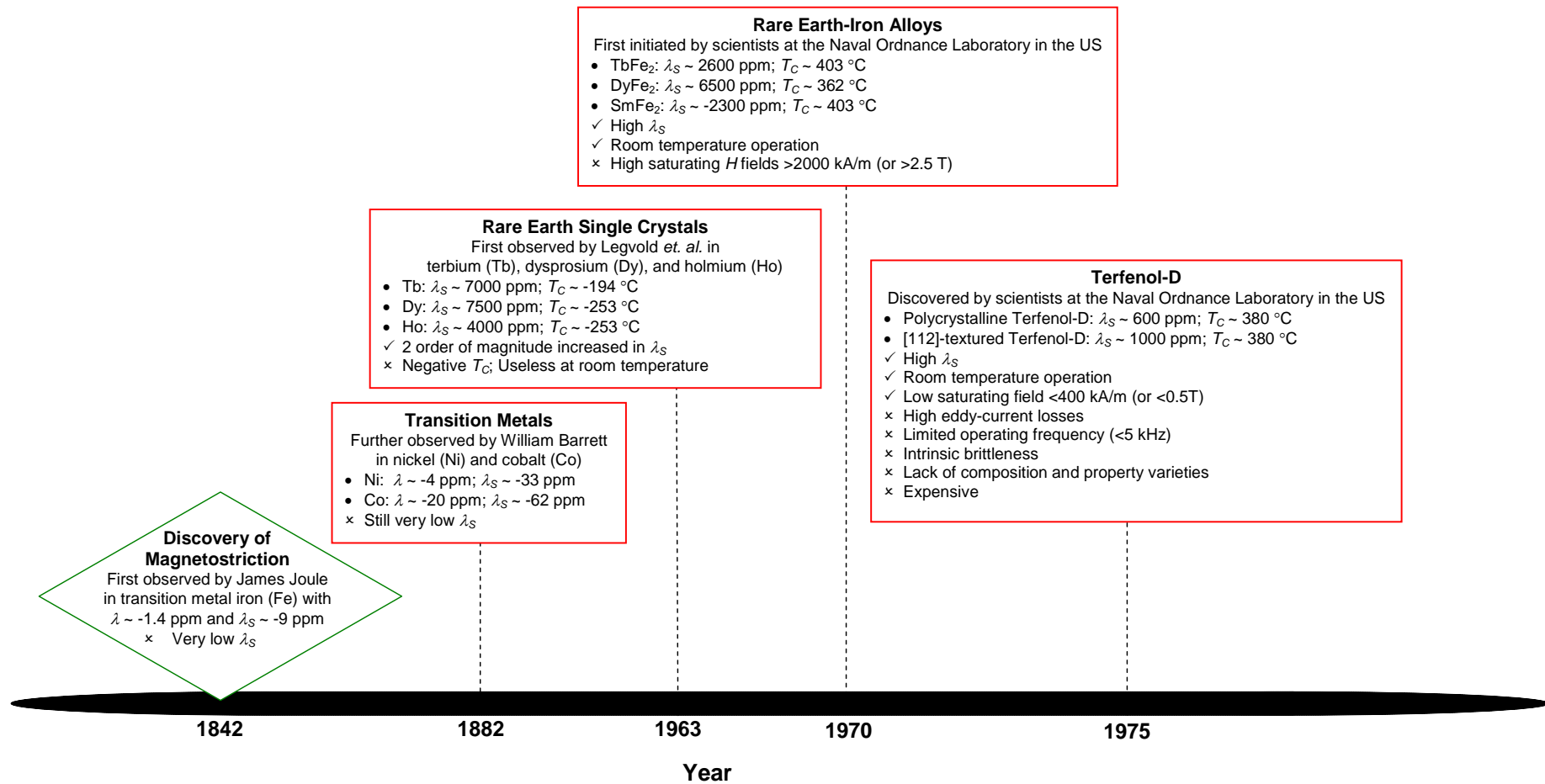


Fig. 1.11 The evolution of magnetostrictive materials from 1842 to 2002 [13-21].

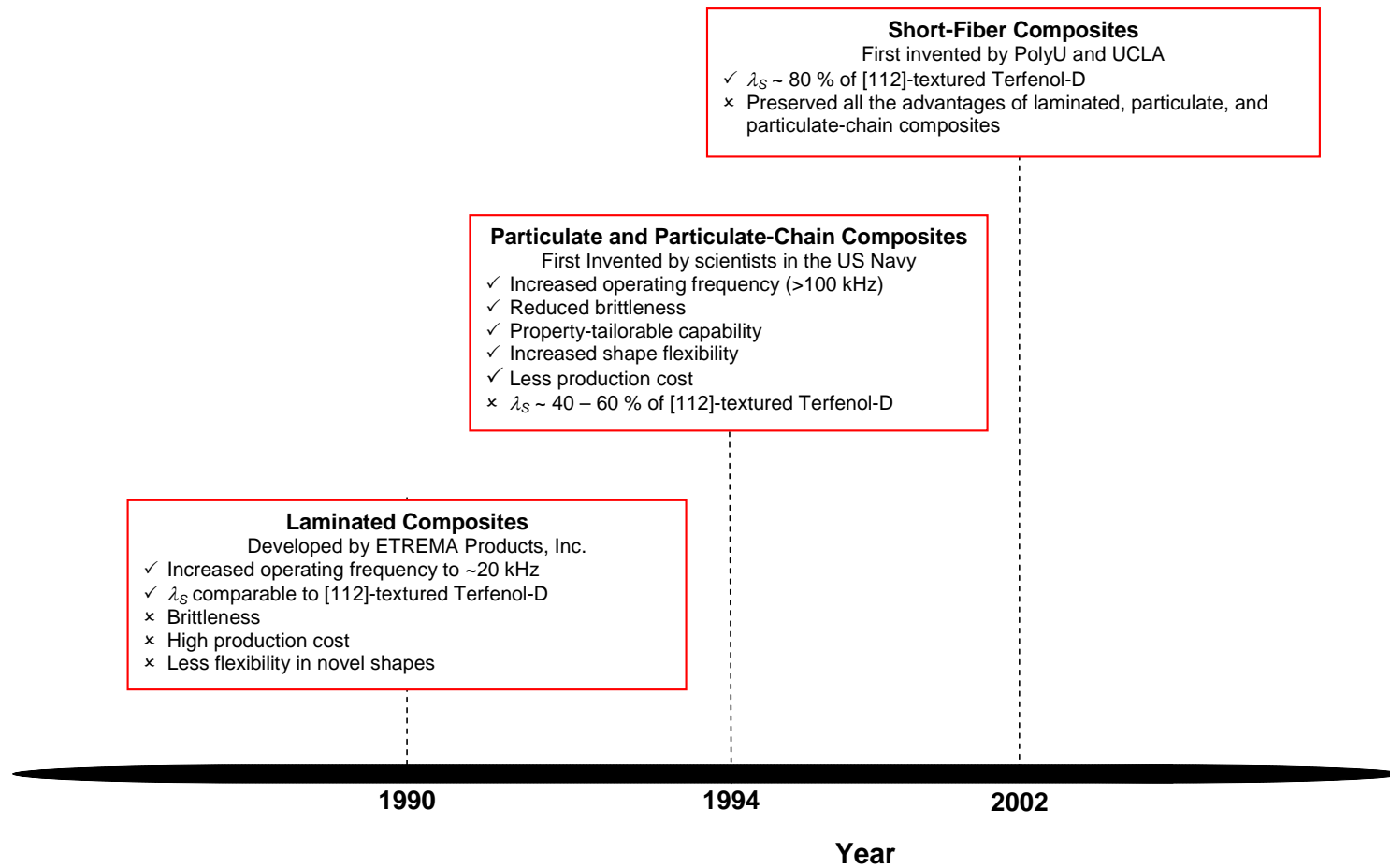


Fig. 1.11(con't) The evolution of magnetostrictive materials from 1842 to 2002 [13-21].



1.3.1 Transition Metals

The magnetostriction was first observed in iron (Fe), a common transition metal, by James Prescott Joule in 1842. Joule used “nitric acid” batteries and a long copper solenoid to generate an H field to a Fe bar and measured the induced displacement value by a lever system with 3000 times amplification. Using this simple setup, Joule found a reduction in length of $1/720000$, corresponding to -1.4 ppm magnetostriction, in the Fe bar when magnetized. The phenomenon was labeled as “Joule magnetostriction” (also see Section 1.2.3). Further investigation of magnetostrictive materials into the 1880s led to the discovery of other common transition metals, including nickel (Ni) and cobalt (Co) with very limited Joule magnetostrictions of -4 and -20 ppm, respectively by William Fletcher Barrett [21]. Later studies found λ_S of about -9, -33, and -62 ppm in Fe, Ni, and Co, respectively [22]. Initial sonar transducers were contemplated for exploiting these transition metals but were left unexplored due to the discovery and rapid development of high-strain piezoelectric quartz in 1916, barium titanate (BaTiO_3) in 1941, and lead zirconate titanate (PZT) in 1954 [22].



1.3.2 Rare Earth Single Crystals

The era of giant magnetostriction began in the 1960s when Legvold *et al.* measured positive λ_S of 7500 ppm and T_C of $-253\text{ }^\circ\text{C}$ in dysprosium (Dy) single crystal, together with positive λ_S of 4000 ppm and T_C of $-253\text{ }^\circ\text{C}$ in holmium (Ho), in 1963 [23]. Clark *et al.*, in the same year, measured magnetostriction of the same order in yttrium iron garnet (YIG) single crystal [24]. Two years later, Clark *et al.* studied the thermal expansion and magnetostriction in Dy single crystal [25] and measured positive λ_S of 7000 ppm and T_C of $-194\text{ }^\circ\text{C}$ in terbium (Tb) single crystal [26].

The observed λ_S in all of these rare earth single crystals were two orders of magnitude greater than any previously reported transition metals. However, these crystals possessed $T_C < 0^\circ\text{C}$, which imposed a significant restriction to their operating temperatures to even below $T_C < 0^\circ\text{C}$. Nevertheless, the discovery of rare earth magnetostriction gave a clear direction for the development of rare earth(s)-based alloys in the 1970s. In general, rare earths exhibit three distinct regions of behavior on temperature. In the coldest region below T_C , the rare earths are ferromagnetic with a hexagonal close packed (hcp) structure. Above T_C , they demonstrate antiferromagnetic behavior with null net magnetization due to the compensation of each “positive” magnetic moment with a “negative” magnetic moment in a long-range



order. At a certainly higher temperature called the Néel temperature (T_N), they become paramagnetic and the magnetic moments are independent and do not possess long-range order.

1.3.3 Rare Earth-Iron Alloys

The ultra-low temperature magnetostriction of rare earth single crystals stimulated researchers into synthesizing compounds of rare earths and transition metals so as to elevate T_C above room temperature in the 1970s by scientists at the Naval Ordnance Laboratory in the United States (US).

Initial studies on synthesizing rare earth-transition metal compounds led to the formulation of a number of stable systems [27]. Among them, the most promising systems for magnetostrictive applications were those with Fe; the most stable formulations were RFe_2 , RFe_3 , and R_2Fe_{17} , where R represents a rare earth including Tb, Dy, Ho, Er, Tm, and Sm; and the largest λ_S at room temperature was observed in the RFe_2 formulation with positive λ_S of 2600 ppm and T_C of 438 °C in $TbFe_2$ compound and with positive λ_S of 6500 ppm and T_C of 362 °C in $DyFe_2$ compound. Some of the compounds exhibited negative magnetostriction of which $SmFe_2$ exhibited the largest negative λ_S of 2300 ppm and T_C of 403 °C. The RFe_3 formulation



showed saturation magnetostrictions of only a half of the RFe_2 formulation. Unfortunately, the saturating fields were as large as 800 – 2000 kA/m in DyFe and over 2000 kA/m in TbFe₂ because of the existence of huge magnetocrystalline anisotropy in the rare earth-Fe compounds.

This enormous magnetocrystalline anisotropy hindered the use of the rare earth-Fe compounds in practical applications since the magnetic fields required to observe magnetostrictions were limited to laboratory magnets at low frequencies. However, an interesting idea to create technologically useful compounds was ignited by developing tertiary compounds of two different rare earths and Fe. From torque magnetometer measurements, it was known that some RFe_2 compounds possess positive anisotropy constants and some of them have negative anisotropy constants. The following section describes the discovery of a giant $RR'Fe$ ($R \neq R'$) alloy having giant magnetostriction and nearly zero net magnetocrystalline anisotropy by compensating the large positive anisotropy constant of Tb with the large negative anisotropy constant of Dy.



1.3.4 Terfenol-D

The modern era of magnetostrictive materials began in the early 1970s when scientists at the Naval Ordnance Laboratory in the US discovered unusually large or “giant” magnetostriction by alloying Fe with Tb and Dy. The culmination of research on basic materials for an engineering alloy was reached in 1975 with Terfenol-D ($\text{Tb}_{0.3}\text{Dy}_{0.7}\text{Fe}_{1.92}$) [21], a $RR'\text{Fe}$ alloy exhibiting giant positive λ_s in excess of 1000 ppm at low fields (~ 400 kA/m) and high T_C of 380 °C. Terfenol-D was named after terbium (Ter), iron (fe), Naval Ordnance Laboratory (nol), and dysprosium (D).

Monolithic Terfenol-D using the free-stand-zone melt process possesses a cubic crystal structure. Terfenol-D has a positive magnetostriction and features a large magnetostrictive anisotropy in accordance with its crystallographic structure. Magnetostrictive anisotropy dictates the material’s preferred magnetic domain orientation through energy minimization and is determined in part by the material stoichiometry. Figure 1.12 illustrates a schematic of the crystallographic structure of Terfenol-D within the confines of a cylindrical shaped sample. The collective group of $\langle 111 \rangle$ axes constitutes the easy axes. That is, the magnetocrystalline anisotropy favors alignment of the magnetic domains along these axes. Considering magnetization vectors in the $[100]$ plane, the $[111]$ vector is within 19.5° of the rod

axis. Since Terfenol-D exhibits positive magnetostriction, domain rotation into the direction of the $[11\bar{1}]$ vector causes the rod to lengthen. The $[11\bar{1}]$ vector, which points in a direction nearly perpendicular to the rod axis, is also an easy axis. Application of compressive stress along the longitudinal axis of the rod favors the alignment of magnetic domains in the $[11\bar{1}]$ direction. It is noted that magnetostriction in Terfenol-D is the product of the 90° domain rotation. As a result, magnetization due to an applied H field in either the $[11\bar{2}]$ or $[112]$ direction leads to a positive magnetostriction.

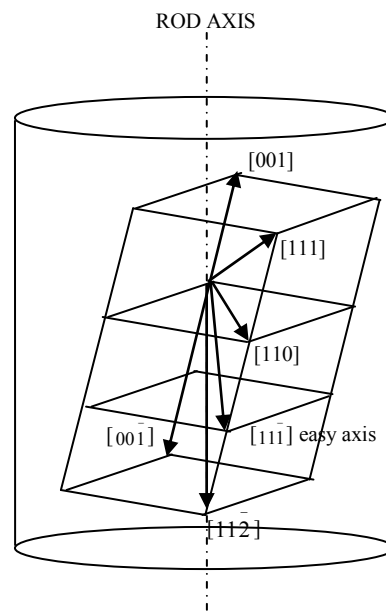


Fig. 1.12 Crystallographic structure of Terfenol-D.



The US Navy generally recognized Terfenol-D as a promising material of enormous value to high-power sonar transducers and, indeed, numerous studies were conducted to investigate its microstructure, domain process, preparation methods, magnetostrictive properties and practical viability. While the material and its associated devices have been commercially available since the late 1980s [28], four crucial problems have significantly impeded their use. The first is the limitation of the operating frequency to a few kilohertz due to the presence of eddy-current losses; the second is the difficulties in machining and fabricating devices owing to the brittleness nature of the material; the third is the lack of composition and property varieties; and the fourth is the high material cost.

1.3.5 Epoxy-Bonded Terfenol-D Composites

In response to these shortcomings, much research effort in the 1990s shifted to developing a complementary material to monolithic Terfenol-D, by extending its high-frequency range into the ultrasonic regime (≥ 20 kHz), increasing its durability, expanding its composition and property variability, and reducing its cost. The most promising solution was to fabricate epoxy-bonded Terfenol-D composites.

1.3.5.1 Laminated Composites

The principal motivation for the development of epoxy-bonded Terfenol-D composites is the reduction of electron conduction path length in the magnetostrictive phase and provides a subsequent reduction in eddy current-induced heating at high frequencies [29]. Monolithic Terfenol-D rods with a diameter of several millimeters work reasonably well in applications up to several kilohertz. For higher frequencies, eddy currents appear, which not only heat up the material but also prevent the applied magnetic field from penetrating the material.

By simply cutting monolithic Terfenol-D into thin sheets and then laminating the sheets using a passive epoxy, laminated composites were produced by ETREMA Products, Inc. in the US in 1990 to elevate the operational frequency to about 20 kHz (Fig. 1.13) [28]. However, these significant cutting and lamination processes involved high production cost and less flexibility in novel shapes.

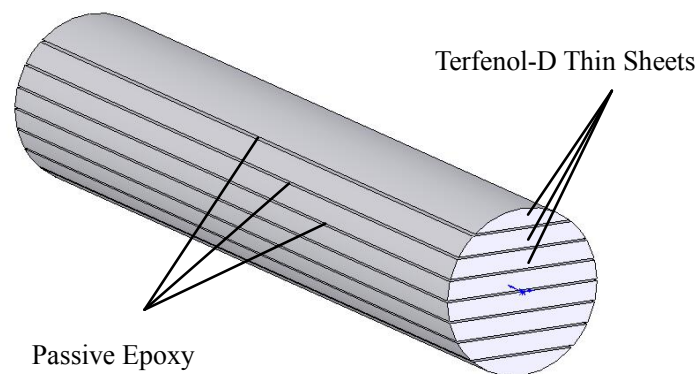


Fig. 1.13 Schematic diagram of a laminated composite.



1.3.5.2 Particulate and Particulate-Chain Composites

Researchers in the US Navy in 1994 incorporated ball-milled, random-shaped, random-oriented Terfenol-D particles with poly-distributed sizes of 10 – 300 μm in at least one dimension into a passive epoxy matrix to form particulate and particulate-chain composites (Fig. 1.14) [30, 31]. They claimed that the high electrically resistant epoxy matrix ($\sim 10^{14} \Omega\cdot\text{m}$) embedding the low electrically resistant Terfenol-D particles ($0.6 \times 10^{-6} \Omega\cdot\text{m}$) increases composite resistivity, reduces eddy current losses at high frequencies, and broadens the operational bandwidth. Moreover, the resulting materials are relatively simple, inexpensive, durable, machinable, and property-tailorable. Particulate (i.e., dispersing particles in the matrix) and particulate-chain (i.e., aligning Terfenol-D particles in the matrix) based on the 0–3 and pseudo 1–3 architectures were produced. This invention attracted considerable interest in furthering research into both types of composites, especially in the Europe and US. Remarkable progress was achieved by the University of Brighton and the University of California, Los Angeles (UCLA) on the particulate and particulate-chain composites, respectively [32].

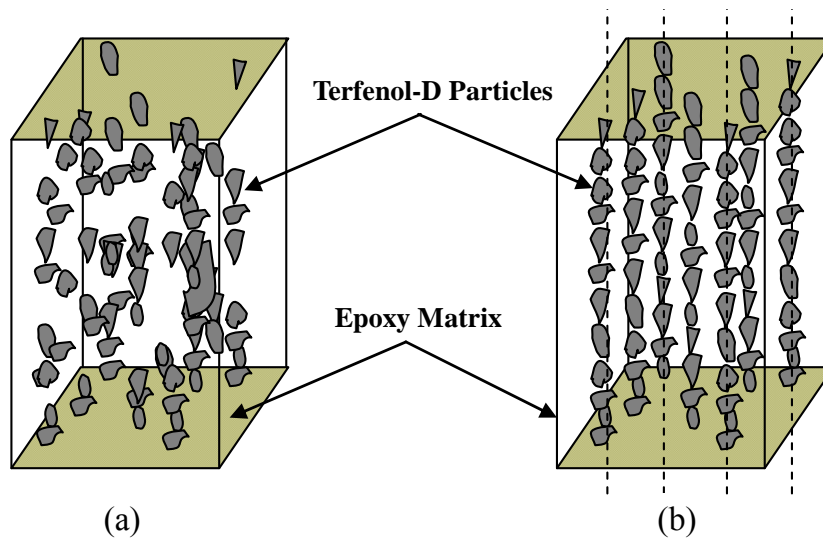


Fig. 1.14 Schematic diagrams of (a) a particulate composite and (b) a particulate-chain composite.

Today, it is generally known that particulate-chain composites have magnetostrictive properties generally higher than the particulate composites due to their anisotropic nature. Moreover, both types of composites usually attain their optimal property values when their particulate volume fractions reach 0.6 or above. Furthermore, they possess increased operational bandwidths to the hundred kilohertz range. In addition, they have reduced mechanical brittleness, added property-tailorable capability, and reduced material costs compared to monolithic Terfenol-D. Unfortunately, their magnetostrictions fall short of the Terfenol-D by at least 30 %.

1.3.5.3 Short-Fiber Composites

On the horizon of improving state-of-the-art composites, a significant discovery of short-fiber composites (Fig. 1.15), with magnetostrictive properties reaching about 80 % of the monolithic Terfenol-D and preserved advantages of particulate and particulate-chain composites, was made by a collaborative effort between The Hong Kong Polytechnic University (PolyU) and University of California, Los Angeles (UCLA) in 2002 [33]. The improved magnetostrictive properties in these short-fiber composites was directly ascribed to the presence of a [112] preferential particulate orientation.

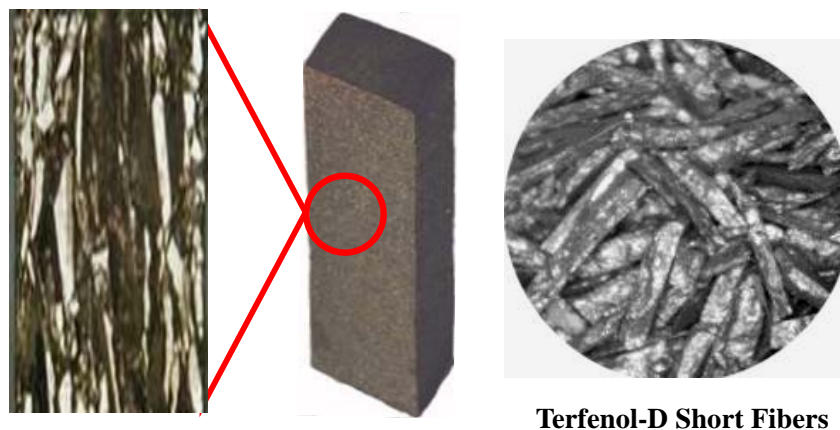


Fig. 1.15 A short-fiber composite and its needle-shaped, [112]-oriented Terfenol-D short fibers [33].

Prior to this discovery, the particulate and particulate-chain composites were fabricated with irregularly shaped, randomly oriented particles ball-milled from a



commercially available [112]-textured monolithic material. As a result, the best reported behavior of these composites is polycrystalline behavior about the same as for polycrystalline Terfenol-D and is much lower than for [112]-textured Terfenol-D. In order to enable [112]-texturing in composites, an innovative and promising approach utilizing magnetic shape anisotropy and needle-shaped, [112]-oriented Terfenol-D short fibers of about 3 mm long and 0.8 mm wide (length-to-wide aspect ratio of 3.7:1) was implemented by PolyU and UCLA. It is noted that magnetic shape anisotropy arises from the difference in energies associated with magnetizing a finite-sized specimen along different directions. Magnetocrystalline anisotropy, which also plays an active role in particulate orientation, is minimal in Terfenol-D, and thus particulate orientation is dominated by magnetic shape anisotropy. For a needle-shaped short fiber, magnetic shape anisotropy tends to orient the fiber along its longest geometric axis where the demagnetizing field is minimized. This implies that [112]-oriented short-fiber composites can be fabricated by preparing needle-shaped Terfenol-D short fibers with their longest geometric axes oriented along the highly magnetostrictive [112] crystallographic direction, and then applying magnetic shape anisotropy to preferentially orient these particles with their long axes aligned along the longitudinal direction of the composites.



1.4 Objective of Project

Following the evolutionary stage of magnetostrictive materials described in Section 1.3, it is the main objective of the present study to develop a promising new type of epoxy-bonded Terfenol-D continuous-fiber composite system with a preferred [112] crystallographic orientation. These crystallographically oriented continuous-fiber composites are expected to demonstrate improved magnetostrictive properties compared to the monolithic Terfenol-D, in addition to preserving the desired benefits of the state-of-the-art particulate-chain and short-fiber composites. Emphases are placed on the fabrication, characterization, and optimization of these composites, as well as on the applications of these composites to smart transducers and actuators.

1.5 Scope of Project

To facilitate the development, investigation, and applications of the proposed epoxy-bonded, [112]-oriented Terfenol-D continuous-fiber composites, the following sequence is followed.

- (1) [112]-oriented Terfenol-D continuous fibers of 45 mm long and (1 mm × 1 mm) square cross section are prepared and used to fabricate bar-shaped, epoxy-bonded, [112]-oriented Terfenol-D continuous-fiber composites of 45



mm long and (12 mm × 12 mm) square cross section with six Terfenol-D volume fractions ranging from 0.2 to 0.7. State-of-the-art epoxy-bonded Terfenol-D short-fiber and particulate-chain composites of the same dimensions are also prepared for comparison. (Chapter 2)

- (2) The quasistatic magnetic and magnetostrictive properties of the continuous-fiber composites are evaluated as functions of applied magnetic field, Terfenol-D volume fraction, and post-curing temperature with zero external stress loading and at room temperature. The measurement results are compared to those of the short-fiber and particulate-chain composites, and the enhanced magnetostrictive properties are explained by a physical model.

(Chapter 3)

- (3) The dynamic magnetic and magnetostrictive properties of the continuous-fiber composites are also measured as functions of frequency, magnetic bias field, and Terfenol-D volume fraction. The measurement results are again compared to those of the short-fiber and particulate-chain composites and explained theoretically. (Chapter 4)

- (4) Two distinct smart devices, including a tunable vibration absorber for active absorption of vibrations in vibrating structures and a 64 kHz sandwich



transducer for sonic and ultrasonic driving, are developed to demonstrate the application potential of the developed continuous-fiber composites. Details of the structure, operational principle, design modeling/simulation, fabrication, and characterization of the smart devices are disclosed. (Chapter 5)

- (5) Conclusions and suggestions for future work are given. (Chapter 6)



Chapter 2

Fabrication of Epoxy-Bonded Terfenol-D Continuous-Fiber Composites

2.1 Introduction

As mentioned in the previous chapter, epoxy-bonded Terfenol-D short-fiber composites with [112]-oriented Terfenol-D short fibers (3 mm long and 0.8 mm wide) possess the distinct advantages of reduced eddy-current losses, increased operating frequency, reduced mechanical brittleness, improved shape novelty, added property-tailorable capability, and reduced material costs compared to monolithic Terfenol-D in general. These short-fiber composites also exhibit the best magnetostrictive properties with the largest magnetostrictive strain outputs reaching about 80% of the monolithic Terfenol-D as compared with their laminated, particulate, and particulate-chain composites in particular. By increasing the fiber length and preparing [112]-oriented Terfenol-D continuous (or long) fibers of 45 mm long and 1 mm wide, it is practically viable to push the magnetostrictive composite technology toward the extreme type of the crystallographically oriented continuous-fiber composite system. This extreme type of composite system is expected to demonstrate even larger magnetostrictive strains than the monolithic Terfenol-D, besides having the desired advantages of the traditional magnetostrictive composites.



In this chapter, we address the preparation of Terfenol-D elements and epoxy matrix as well as the fabrication of epoxy-bonded, [112]-oriented Terfenol-D continuous-fiber composites for performance study and applications in later chapters. The organization of this chapter is as follows: First, the preparation and preservation of Terfenol-D continuous fibers, short fibers, and particles are described. Second, a brief review on the preparation and material properties of the epoxy matrix is presented. Third, the fabrication of the Terfenol-D continuous-fiber composites is disclosed, together with the short-fiber and particulate-chain composites.

2.2 Preparation of Terfenol-D Elements

2.2.1 Material Used

Giant magnetostrictive alloy Terfenol-D was used as the active phase in our continuous-fiber, short-fiber, and particulate-chain composites. [112]-textured monolithic Terfenol-D plates, with the nominal composition of $Tb_{0.3}Dy_{0.7}Fe_{1.92}$ and the desired dimensions of 45 mm long, 30 mm wide, and 1 mm thick, were commercially supplied by Baotou Rare Earth Research Institute, Inner Mongolia, China (Fig. 2.1). The as-supplied monolithic Terfenol-D had the highly magnetostrictive [112] crystallographic axis oriented along the long (or the 3) direction. The material properties of the monolithic Terfenol-D provided by the manufacturer are summarized in Table 2.1 [34].

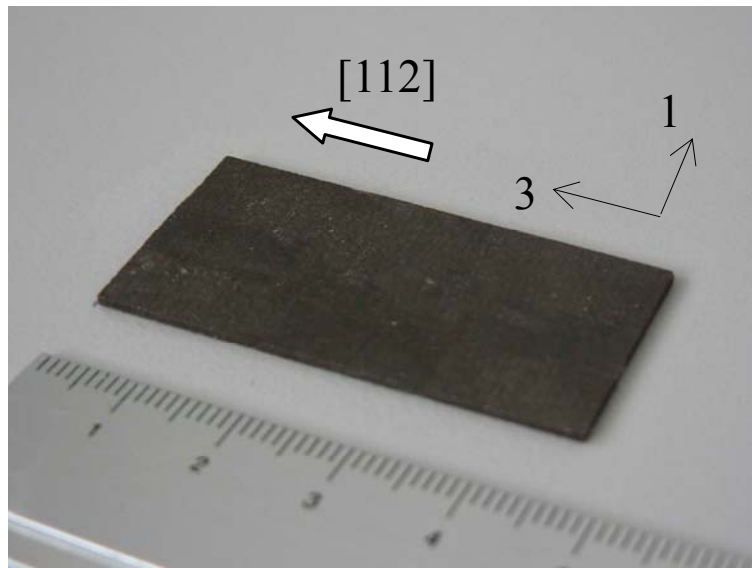


Fig. 2.1 Photograph of an [112]-textured monolithic Terfenol-D plate with dimensions 45 mm long, 30 mm wide, and 1 mm thick.

Table 2.1 Material properties of the monolithic Terfenol-D in Fig. 2.1 provided by the manufacturer [34].

Magnetostriction (ppm)	≥ 700 ppm (100 kA/m, 0 MPa) ≥ 1000 ppm (100 kA/m, 10 MPa)
Young's Modulus (GPa)	25 – 65
Tensile Strength (MPa)	≥ 25
Compressive Strength (MPa)	≥ 260
Thermal Expansion Coefficient ($\times 10^{-6}/^{\circ}\text{C}$)	8 – 12
Thermal conductivity (J/ $^{\circ}\text{C}/\text{m}/\text{s}$)	10.5 – 10.8
Curie Temperature ($^{\circ}\text{C}$)	380
Coupling Factor	0.65 – 0.75
Sound Velocity (m/s)	1700 – 2600
Operating Temperature ($^{\circ}\text{C}$)	-40 – 150
Density (kg/m^3)	9150 – 9250
Energy Density (kJ/m^3)	14 – 25
Relative Permeability	5 – 10
Electrical Resistivity ($\mu\Omega\cdot\text{m}$)	0.6
Heat Capacity ($\text{kJ}/\text{kg}\cdot\text{K}$)	0.35
Response Time (μs)	< 1
Response Range of Frequency (kHz)	1 – 10



2.2.2 [112]-Oriented Terfenol-D Continuous Fibers

To produce engineering magnetostrictive composites with the preferred [112]-textured behavior as in monolithic Terfenol-D, it is necessary to prepare high aspect-ratio Terfenol-D continuous (or long) fibers with their long direction coincided with their highly magnetostrictive [112] crystallographic axis (Fig. 1.12).

As monolithic Terfenol-D is hard and brittle and has very extremely low electrical resistivity of $0.6 \mu\Omega\cdot\text{m}$ (Table 2.1), it has been found that the traditional mechanical cutting based on diamond saw is incapable of producing Terfenol-D fibers with length-to-width aspect ratio greater than 5:1 [33]. It can typically produce short fibers with an average aspect ratio of 3.7:1 instead. In fact, the lately reported epoxy-bonded Terfenol-D short-fiber composites are exactly based on such an average aspect ratio [35]. In our study, high aspect ratio fibers of 45:1 (45 mm long, 1 mm wide) were produced using a wire electrical discharge machining (WEDM) process rather than the traditional mechanical cutting process based on diamond saw.

WEDM is an advanced machining technique primarily used for hard metals or metals which are not compatible with traditional machining techniques. WEDM relies on a nontraditional technique of removing material by a series of rapidly recurring electric arcing discharges between an electrode wire (usually made of brass or molybdenum) and the work piece in the presence of an energetic electric field [36]. The electrically charged wire is guided along the desired path very close to (but not touch) the work piece. Consecutive sparks produce a series of micro-craters on the work piece, thereby removing material along the cutting path through melting and vaporization. The material particles are washed away by the continuously flushing water. It is noted that a similar micro-crater is also formed on the surface of the



electrode, the debris from which must thus be flushed away. These micro-craters result in the gradual erosion of the wire so that constant replacement of the wire by feeding from a spool is needed.

One critical concern about the use of WEDM is that it only works with materials that are electrically conductive. This means that WEDM does not work with most ceramics and polymers. Fortunately, our Terfenol-D is a good electrical conductor that fits well with the WEDM process. On the other hand, null force or stress should be imposed on the highly brittle Terfenol-D in order to produce high aspect ratio fibers. The zero force nature of the WEDM process is thus a proper machining technique to handle Terfenol-D.

To produce the [112]-oriented Terfenol-D continuous fibers, the monolithic Terfenol-D in Fig. 2.1 was placed inside the water bath a WEDM equipment (MITSUBISHI SX-20) as shown in Fig. 2.2 such that it could be sliced along the [112] crystallographic direction (also the long direction) of the monolithic Terfenol-D plate. The plate was slice repeatedly, and a total of 29 fibers with dimensions 45 mm long and (1 mm × 1 mm) cross-section could generally be obtained based on an as-supplied monolithic Terfenol-D of 45 mm long, 30 mm wide, and 1 mm thick (Fig. 2.3). The process parameters of the WEDM for our Terfenol-D fibers are listed in Table 2.2.



Fig. 2.2 A commercial wire electrical discharge machining (WEDM) equipment used to prepare our [112]-oriented Terfenol-D continuous fibers.

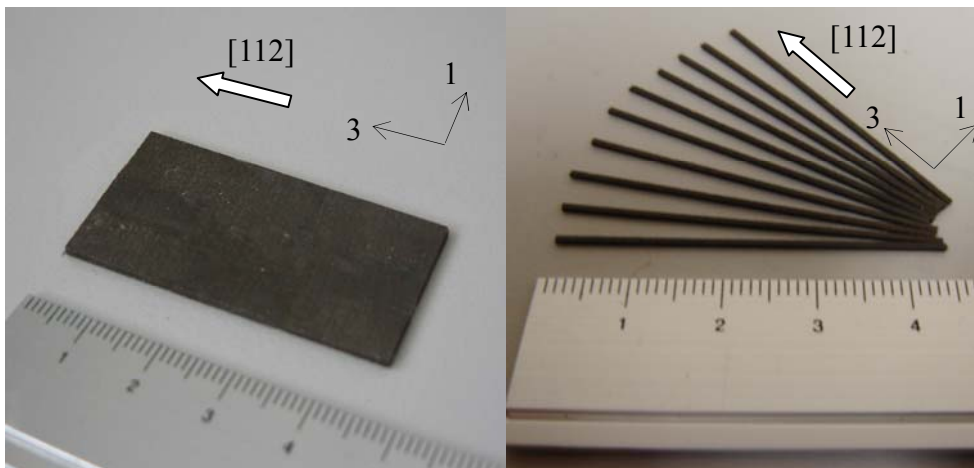


Fig. 2.3 An as-supplied monolithic Terfenol-D plate (left) and WEDM-processed, [112]-oriented Terfenol-D continuous fibers of 45 mm long and (1 mm × 1 mm) cross-section (right).

Table 2.2 Process parameters of the WEDM in Fig. 2.2 for our Terfenol-D fibers.

Cutting Speed (mm^2/min)	100
Discharge Current (A)	4
Wire Diameter (mm)	0.2
Wire Tension (N)	10
Wire Feeding Speed (m/s)	8
Surface Roughness (μm)	Ra 10
Cutting Fluid Type	Emulsion
Cutting Degree ($^\circ$)	0



The WEDM-processed continuous fibers were “washed” using lint-free laboratory wipes and pure alcohol. This cleaning process was designed to remove some of the fine dusts ($< 1 \mu\text{m}$ size) adhered on the fibers and to provide much cleaner surfaces for later binding with the epoxy matrix in our composites. The scanning electron micrograph (SEM) in Fig. 2.4 indicates that the edges of the resulting fibers are quite smooth without obvious chipping.

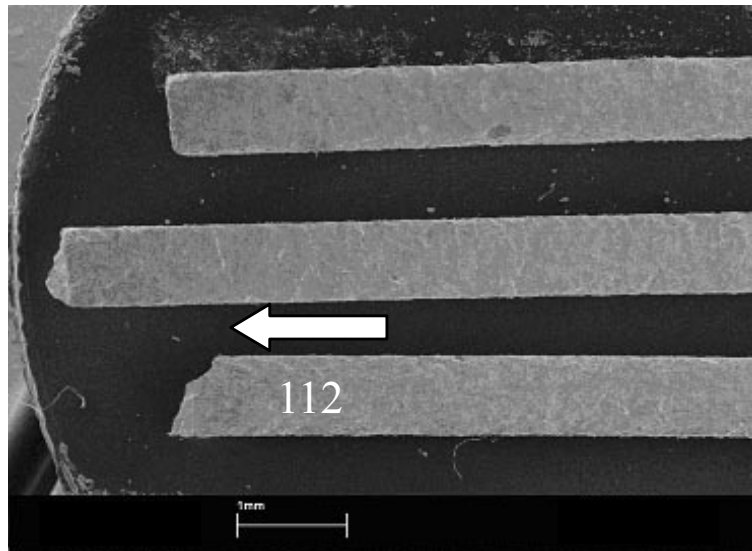


Fig. 2.4 Scanning electron micrograph (SEM) showing three pieces of [112]-oriented Terfenol-D continuous fibers after the WEDM and cleaning processes. The WEDM process is well-controlled so that the edges of the fibers are quite smooth without obvious chipping.

Since Terfenol-D contains a significant amount of iron (Fe), the increased surface area in the Terfenol-D continuous fibers (Figs. 2.3 and 2.4) is much susceptible to oxidation and corrosion if the Terfenol-D continuous fibers are not properly stored. Hence, our Terfenol-D continuous fibers were stored in a sealed glass container of inert gas and placed in an environmental chamber (Procan PD63) with humidity and temperature control.



In order to confirm whether the quality of the resulting continuous fibers could be preserved after the WEDM and cleaning processes, the quasistatic magnetostrictive strain (λ) as a function of applied magnetic field (H_3^{QS}) for some of the as-supplied monolithic Terfenol-D plates and continuous fibers was measured at 0.1 Hz frequency, room temperature, and zero stress loading. Details of the quasistatic measurements are available in Chapter 3. It is clear from Fig. 2.5 that the magnetostrictive response of the continuous fibers agrees well with that of the as-supplied monolithic Terfenol-D plates. Also, their λ values at 100 kA/m are found to be about 800 ppm, which coincides with the manufacturer's data of ≥ 700 ppm at 100 kA/m (Table 2.1). These agreements indicate the existence of neglectable effects before and after the WEDM and cleaning processes.

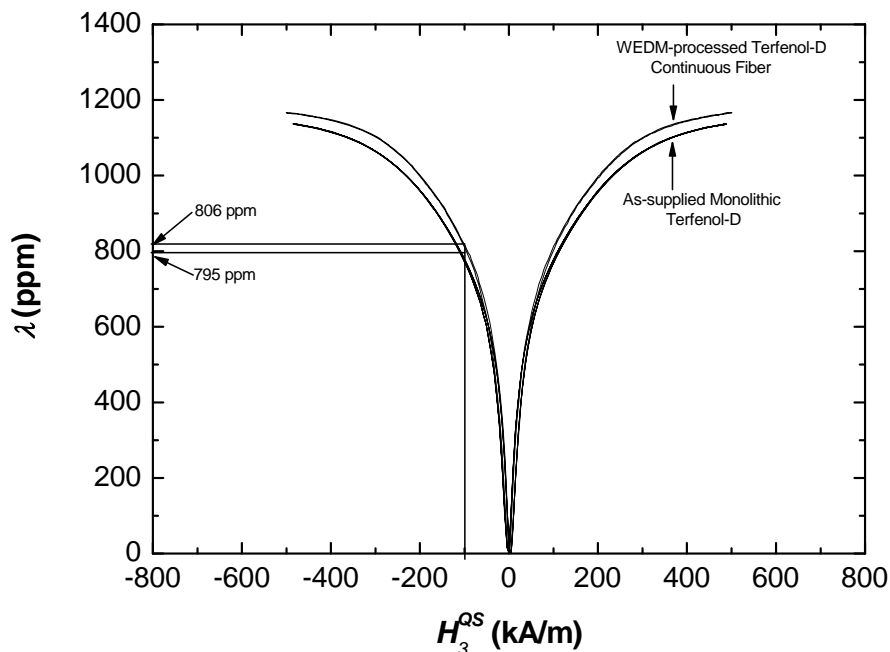


Fig. 2.5 Quasistatic magnetostrictive strain (λ) as a function of applied magnetic field (H_3^{QS}) for an as-supplied monolithic Terfenol-D plate and a continuous fibers measured at 0.1 Hz frequency, room temperature, and zero stress loading.



2.2.3 [112]-Oriented Terfenol-D Short Fibers

[112]-oriented Terfenol-D short fibers with lengths of 4 mm and cross section of (1 mm × 1 mm) (Fig. 2.6) were also prepared for further fabrication into [112]-oriented short-fiber composites in Section 2.4.2. The preparation of these short fibers was relatively simple; they were actually collected during the WEDM process for slicing the [112]-oriented Terfenol-D continuous fibers described above. The brittleness nature of Terfenol-D may occasionally lead to imperfection of fiber slicing, resulting in a small amount of broken fibers. These broken fibers preserved the desired [112] crystallographic orientation of their continuous fibers even through their length-to-width aspect ratio was reduced to 4:1.



Fig. 2.6 Optical micrograph of [112]-oriented Terfenol-D short fibers for 4 mm long and (1 mm × 1 mm) cross-section.



2.2.4 Random-Oriented Terfenol-D Particles

Irregularly shaped, randomly oriented Terfenol-D particles with poly-distributed sizes ranging from 10 to 300 μm (Fig. 2.7) were produced by ball-milling the broken fibers mentioned above in an argon gas environment to prevent of oxidation. It should be noted that these particles do not possess any preferred crystallographic orientation; they have polycrystalline behavior with properties substantially lower than the [112]-textured behavior exhibited by monolithic Terfenol-D and Terfenol-D continuous and short fibers [37].

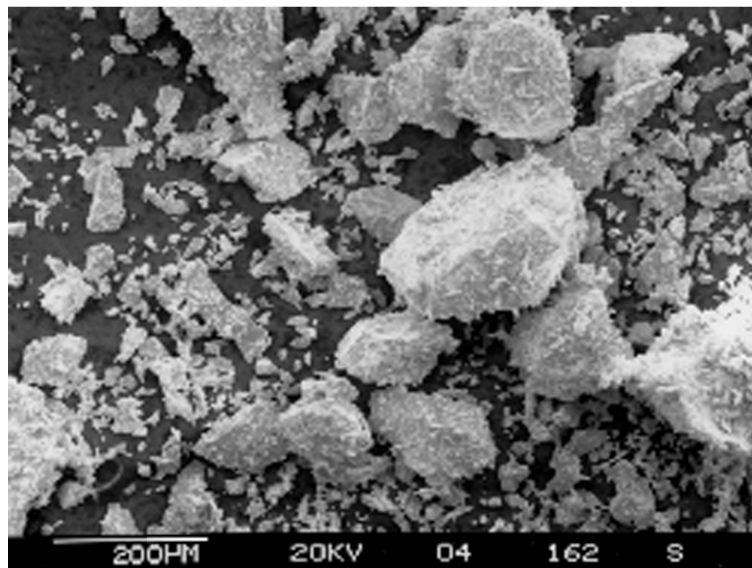


Fig. 2.7 Scanning electron micrograph (SEM) of ball-milled, irregularly shaped, randomly oriented Terfenol-D particles with poly-distributed sizes of 10 – 300 μm .



2.3 Preparation of Epoxy Matrix

Epoxy of Araldite LY564 resin with hardener HY2954 supplied by Ciba-Geigy Hawthorne, New York was chosen as the composite matrix. Araldite LY564/HY2954 epoxy is a high heat resistant (deflection temperature = 180 – 200 °C), high wear resistant (Shore hardness = D85 – D90), and low viscosity (620 mPa·s) thermosetting polymer system at room temperature [24]. The high temperature handling capability imposes limited changes in its properties, thereby increasing the degree of thermal stability of the resulting composites and transducers. The high wear resistant ensures both constituent materials are removed almost equally during cutting and grinding the fabricated composites. The low viscosity makes it easily to fill with the gaps between the Terfenol-D fibers or particles. After Araldite LY564/HY2954 is cured, it is machinable and transparent so that any air bubbles or other imperfections trapped in the composites can be observed.

In the present study, Araldite LY564 resin was mixed thoroughly with HY2954 hardener in a container using a mixing ratio of 100 to 35 by weight. After mixing, the Araldite LY564/HY2954 epoxy was degassed under vacuum for about 10 min. The degassed epoxy was stored in a refrigerator at 4 °C for later use as the matrix phase in the composite fabrication in Section 2.4. Table 2.3 summarizes some of the important material properties of Ciba–Geigy Araldite LY564/HY2954 epoxy at room temperature [38]. These properties will be used in conjunction with those of Terfenol-D for designing composites in Chapters 3 and 4.



Table 2.3 Some of the important material properties of Ciba–Geigy Araldite LY564/HY2954 epoxy at room temperature [39].

Relative Permittivity (at 1 kHz)	3.27
Density (kg/m ³)	1097
Longitudinal Wave Velocity (m/s)	1874
Shear Wave Velocity (m/s)	943
Longitudinal Stiffness Coefficients $c_{11} = c_{22} = c_{33}$ (GPa)	3.852
Shear Stiffness Coefficients $c_{44} = c_{55} = c_{66}$ (GPa)	0.970
Cross-Plane Stiffness Coefficients $c_{12} = c_{21} = c_{23} = c_{32} = c_{13} = c_{31}$ (GPa)	1.898
Longitudinal Compliance Coefficients $s_{11} = s_{22} = s_{33}$ (pm ² /N)	384.6
Shear Compliance Coefficients $s_{44} = s_{55} = s_{66}$ (pm ² /N)	977.0
Cross-Plane Compliance Coefficients $s_{12} = s_{21} = s_{23} = s_{32} = s_{13} = s_{31}$ (pm ² /N)	127.0
Coefficient of Linear Thermal Expansion (°C)	60×10^{-6}
Young's Modulus (GPa)	2.600

2.4 Fabrication of Epoxy-Bonded Terfenol-D Composites

2.4.1 Continuous-Fiber Composites

Terfenol-D continuous fibers and Ciba-Geigy Araldite LY564/HY2954 epoxy prepared and described in Sections 2.2 and 2.3 were used as the active and passive phases, respectively in the fabrication of continuous-fiber composites. Six batches of continuous-fiber composites with nominal Terfenol-D volume fractions (v_f) ranging from 0.2 to 0.7 in steps of 0.1 were fabricated using a vacuum cold casting technique [33]. The advantage of this fabrication technique is that the placement and hence the crystallographic orientation of the fibers in the composites can be readily controlled while this thermosetting polymer is still in the liquid phase.

The fabrication process of the continuous-fiber composites is presented in Fig. 2.8. Appropriate number of continuous fibers, in accordance with those shown in Table 2.4, were placed in acrylic casting molds with cavity dimensions 45 mm long



and (12 mm × 12 mm) cross-section. The epoxy was agitated in its container for 10 min to guarantee the uniformity of mixing between the resin and the hardener before being poured into the casting molds. The molds with fiber-epoxy mixture were put in a vacuum chamber for degassing under vacuum for 20 min in order to ensure that they were free of air bubbles by visual observation.

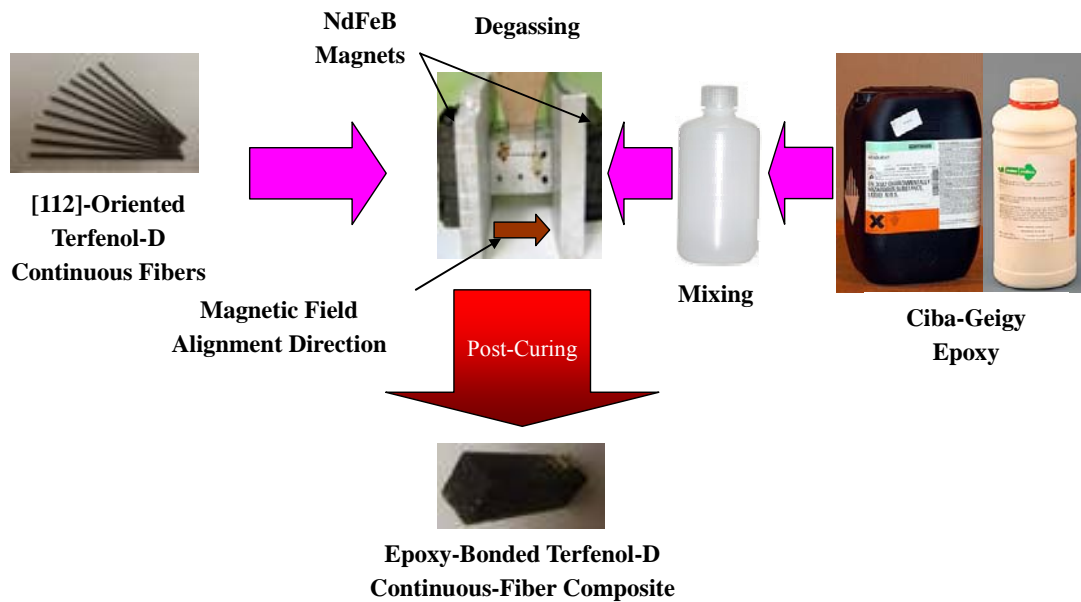


Fig. 2.8 Schematic diagram of the fabrication of epoxy-bonded Terfenol-D continuous-fiber composites.

Table 2.4 Description of the fabricated continuous-fiber composites with dimensions 45 mm long and (12 mm × 12 mm) cross-section.

Terfenol-D Volume Fraction (ν_f)	Number of Terfenol-D Continuous Fibers	Weight of Composite (g)
0.2	29	18.64
0.3	43	21.17
0.4	58	23.70
0.5	72	26.23
0.6	86	28.76
0.7	101	31.29



To maximally align the fibers along the length of the resulting composites, the molds were sealed and screwed with top covers and then placed longitudinally in a static magnetic alignment field of about 30 kA/m produced by a pair of neodymium-iron-boron (NdFeB) permanent magnets (Fig. 2.8). After the fibers were sufficiently aligned, the entire mold-magnet assemblies were placed in a temperature-controlled chamber (Mettmert ULE 400) at 30 °C for 12 h before de-molding. This allowed the fibers to be magnetically aligned while epoxy cure, thereby forming the epoxy-bonded Terfenol-D continuous-fiber composites (Fig. 2.9). The Terfenol-D volume fractions (v_f) of the fabricated composites were confirmed based on the Archimedes' principle and rule-of-mixture formulation (Table 2.4). Moreover, their masses are measured using an analytical balance (AB204-S, METTLER TOLEDO, Switzerland).

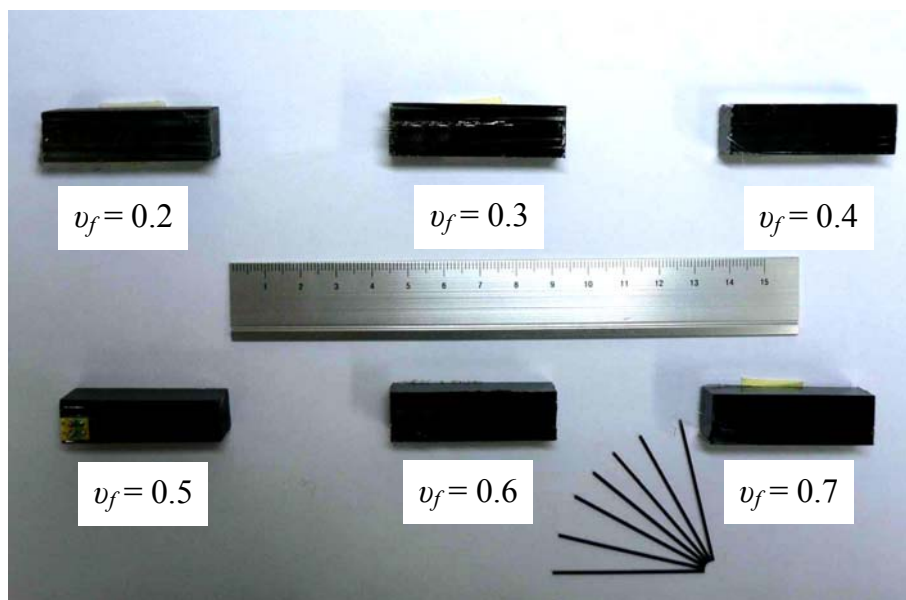


Fig. 2.9 The family of the fabricated epoxy-bonded Terfenol-D continuous-fiber composites.



In order to intentionally create a built-in or residual compressive stress in the embedded continuous fibers via the post-curing of the epoxy matrix, and to enable a systematic investigation of the effects of the post-curing-induced residual compressive stresses on the material properties of our continuous-fiber composites, the de-molded continuous-fiber composites after cured at 30 °C for 12 h were subject to the quasistatic and dynamic measurements to be reported in Chapter 3 and Chapter 4, respectively. The alternation of post-curing and measurements was performed for six successive post-curing temperatures of 30, 40, 50, 60, 70, and 80 °C, each for 12 h.

2.4.2 Short-Fiber and Particulate-Chain Composites

Besides the continuous-fiber composites, short-fiber and particulate-chain composites with 0.5 volume fraction of Terfenol-D short fibers and particles prepared in Section 2.2.3 and Section 2.2.4, respectively were also fabricated using the fabrication technique adopted for the continuous-fiber composites described above, except the magnetic alignment method. It is important to mention that the magnetic alignment field required for aligning short fibers and particles was about 150 kA/m, which is approximately 5 times greater than that required for the continuous-fibers. The reason is attributed to the reduction in fiber length or particle size which, in turn, requires a larger field not only to facilitate the fiber or particle alignment in the epoxy matrix for the production of short-fiber or particulate chains in the epoxy matrix but also to maintain the fiber or particle suspension in the matrix (Fig. 2.10).

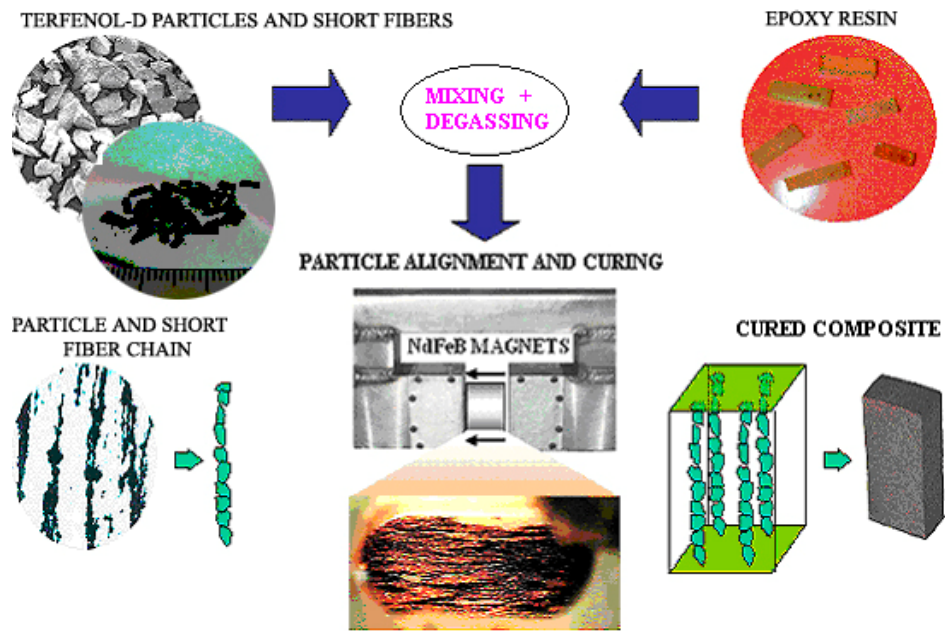


Fig. 2.10 Schematic diagram of the fabrication of epoxy-bonded Terfenol-D short-fiber and particulate-chain composites.



Chapter 3

Quasistatic Material Properties of Continuous-Fiber Composites

3.1 Introduction

By considering the constructive effects of improved stress transfer in high aspect-ratio fibers and preferred [112]-texturing in monolithic Terfenol-D, we have fabricated bar-shaped epoxy-bonded Terfenol-D continuous-fiber composites with six different Terfenol-D volume fractions of 0.2, 0.3, 0.4, 0.5, 0.6, and 0.7 in Chapter 2. In fact, the magnetization and magnetostriction processes described in Chapter 1 (Section 1.2.4) have stated that the magnetostrictive properties of a magnetostrictive material can be maximized by imposing an optimal external stress loading on the material so as to facilitate the maximal motion of the non-180° (90° in specific) domain walls upon applied magnetic fields. Following this idea, we have aimed in the study to intentionally create a built-in or residual compressive stress in the embedded Terfenol-D continuous fibers via the post-curing of the epoxy matrix. To enable a systematic investigation of the effects of the post-curing-induced residual compressive stresses on the material properties of our continuous-fiber composites, the as-fabricated composites in Chapter 2 have first been cured at 30 °C prior to the quasistatic and dynamic measurements to be reported in Chapter 3 and Chapter 4, respectively. This alternation of post-curing process and measurements is preformed with six successive post-curing temperatures of 30, 40, 50, 60, 70, and 80 °C.



In this chapter, the quasistatic magnetic and magnetostrictive properties of the continuous-fiber composites are measured as functions of applied magnetic field, Terfenol-D volume fraction, and post-curing temperature with zero external stress loading and at room temperature. The measured properties are compared with those of the monolithic Terfenol-D, short-fiber, and particulate-chain composites, if any. The observed improvement in the magnetostrictive properties of the continuous-fiber composites is explained by a physical model developed according to the composite mechanics with the requirements for temperature-dependent stress equilibrium within the composites and for stress-dependent saturation strain of Terfenol-D.

3.2 Quasistatic Measurements

3.2.1 Experimental Arrangement and Method

An in-house automated measurement system was used to measure the quasistatic magnetic and magnetostrictive properties of the fabricated composites (Fig. 3.1). This system was also utilized to determine the quasistatic properties of the monolithic Terfenol-D. As shown in Fig. 3.2, this system can generally be divided into two basic parts: (1) the magnetic field generation part and (2) the signal detection and conditioning part. A dynamic signal analyzer (Ono Sokki CF5220), a constant-current-supply amplifier (AE Techron 7572), and a water-cooled, U-shaped electromagnet (Myltem PEM-8005K) form the magnetic field generation part. A Hall probe (PAA71-1908-05) with a Gaussmeter (F. W. Bell 7030), a strain gauge (Measurement Group EA-06-031CF-120-P) with a strain signal conditioner



(Measurement Group Vishay 2360), and a search coil with an integrating fluxmeter (Walker LDJ MF-10) constitute the signal detection and conditioning part.

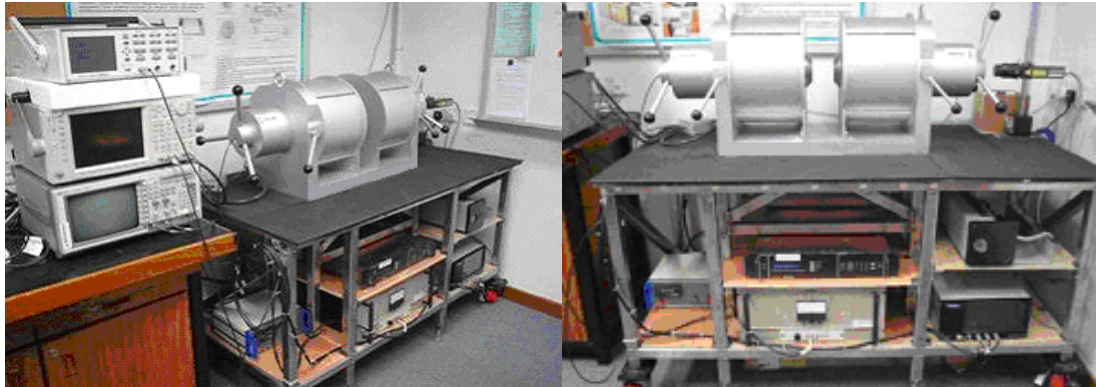


Fig. 3.1 Photographs of the in-house automated quasistatic measurement system.

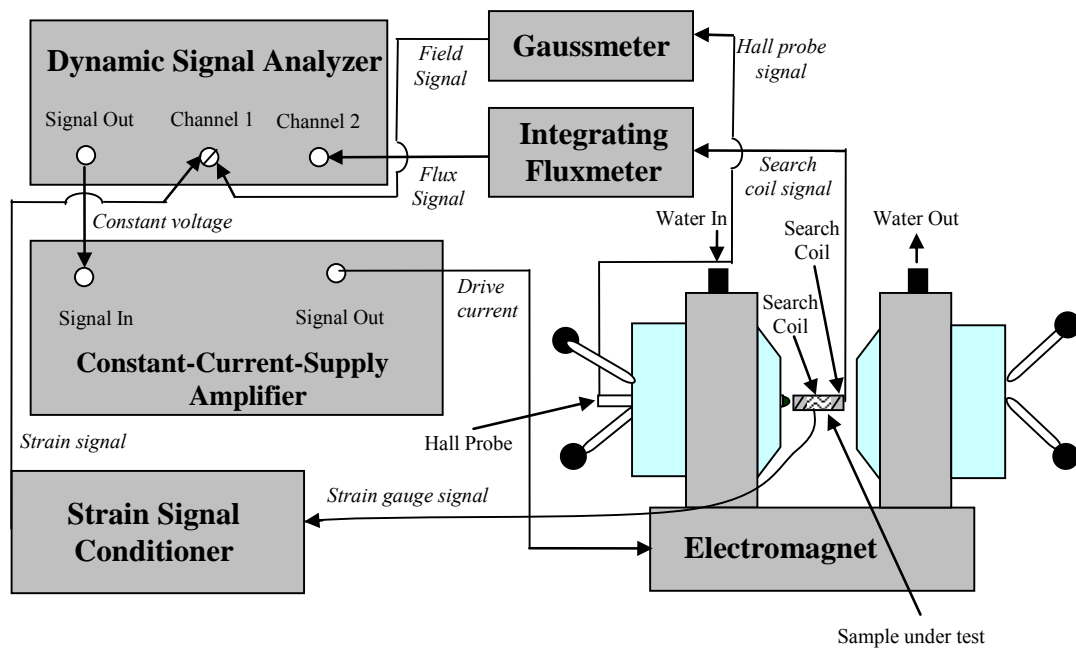


Fig. 3.2 Schematic diagram of the in-house automated quasistatic measurement system in Fig. 3.1.



The quasistatic magnetic and magnetostrictive properties of the samples were measured in the longitudinal direction at room temperature and with zero stress loading. A cyclic magnetic field (H_3^{QS}) with the maximum amplitude of 450 kA/m and a frequency of 0.1 Hz was generated in the longitudinal direction of the samples by the electromagnet driven by the dynamic signal analyzer via the constant-current-supply amplifier. H_3^{QS} was monitored by the Hall probe placed adjacent to the samples and connected to the Gaussmeter. The magnetostriction or magnetostrictive strain (λ) was measured using the strain gauge attached to the center of the samples [Fig. 3.3(a)] and connected to the strain signal conditioner. The magnetic induction (B_3^{QS}) was evaluated by the search coil wrapped around the sample [Fig. 3.3(b)] and linked to the integrating fluxmeter. All quantities were sampled and recorded by the dynamic signal analyzer and stored in a computer. The $B_3^{QS} - H_3^{QS}$ and $\lambda - H_3^{QS}$ curves were obtained directly from the corresponding measured quantities as described. The quasistatic (differential) strain coefficient (d_{33}^{QS}) of the samples was determined from the $\lambda - H_3^{QS}$ curves using

$$d_{33}^{QS} = \frac{\partial \lambda}{\partial H_3^{QS}}. \quad (3.1)$$

The quasistatic (differential) relative permeability (μ_{r33}^{QS}) was found from the $B_3^{QS} - H_3^{QS}$ curves using the relation

$$\mu_{r33}^{QS} = \frac{1}{\mu_o} \frac{\partial B_3^{QS}}{\partial H_3^{QS}}, \quad (3.2)$$



where $\mu_o = 4 \pi \times 10^{-7}$ H/m is the permeability of free space. The magnetization (M_3^{QS}) associated with the captured B_3^{QS} and H_3^{QS} was calculated from

$$M_3^{QS} = \frac{B_3^{QS}}{\mu_o} - H_3^{QS} . \quad (3.3)$$

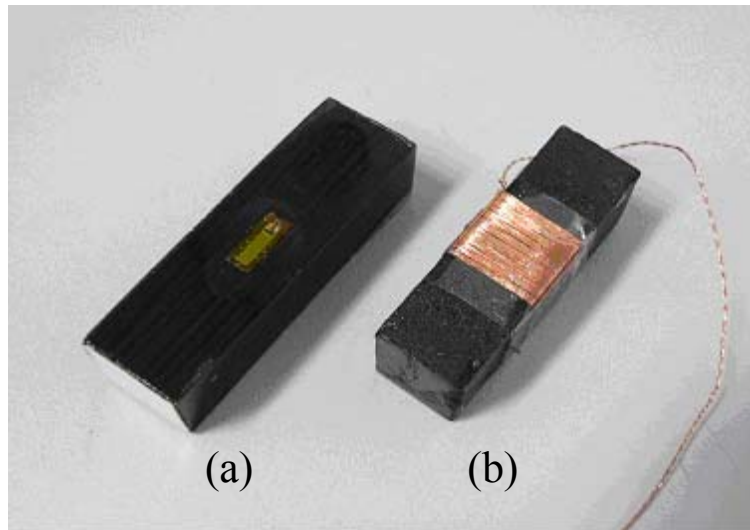


Fig. 3.3 Photograph showing (a) a continuous-fiber composite sample with a strain gauge for the strain-field ($\lambda-H_3^{QS}$) measurement and (b) another sample with a search coil for the flux-field ($B_3^{QS} - H_3^{QS}$) measurement.

3.2.2 Results and Discussion

3.2.2.1 Magnetostrictive Properties

The magnetostriction or magnetostrictive strain (λ) as a function of applied magnetic field (H_3^{QS}) for the continuous-fiber composites with different Terfenol-D volume fractions (v_f) is shown in Fig. 3.4 for various post-curing temperatures (T_{PC}). The $\lambda-H_3^{QS}$ curve for the monolithic Terfenol-D is also included in Fig. 3.4 for comparison. All reported values are the second cycle results that discard the effects of an unknown initial magnetic domain state on λ . It is clear that all samples readily



reach their saturation magnetostrictions or saturation magnetostrictive strains (λ_S) at $H_3^{QS} = 450$ kA/m. The expected large recoverable strains with relatively small hystereses are confirmed in all the samples. At $T_{PC} = 30$ °C [Fig. 3.4(a)], the $\lambda-H_3^{QS}$ curves and hence the λ_S (at 450 kA/m) of our composites demonstrate stable increasing trends with increasing ν_f . None of the composites can surpass the values of λ (for a given H_3^{QS}) and $\lambda_S (= 1150$ ppm) in monolithic Terfenol-D due to the existence of neglectable thermal-induced residual compressive stresses in the composites as described in Section 3.1. When T_{PC} is increased to 40, 50, 60, 70, and 80 °C in Fig. 3.4(b), (c), (d), (e), and (f), respectively, λ and λ_S in the composites increase accordingly with λ_S converging towards a colossal value of about 1610 ppm at an elevated T_{PC} of 80 °C in the composites having $\nu_f \geq 0.3$ [Fig.3.4(f)]. The obvious development of λ and λ_S in the composites with increasing T_{PC} is a result of the increased motion of the non-180° domain walls (see Section 1.2.4) due to the increased residual compressive stresses developed in the continuous fibers during epoxy cure. While the phenomenal effect will further be explained in the following sections, it is important to note that λ_S in our composites is improved by at least 1.4 times the λ_S in the monolithic Terfenol-D. This 1.4-times increment agrees well with the theoretical total allowable strain ($\varepsilon = 3\lambda_S/2$) in an optimally loaded monolithic Terfenol-D upon the complete motion of the available 90° domain walls under fields (see Figs. 1.8 and 1.9). Therefore, the improvement of λ_S in our composites is mainly due to the motion of 90° domain walls in specific and the motion of non-180° domain walls in general.

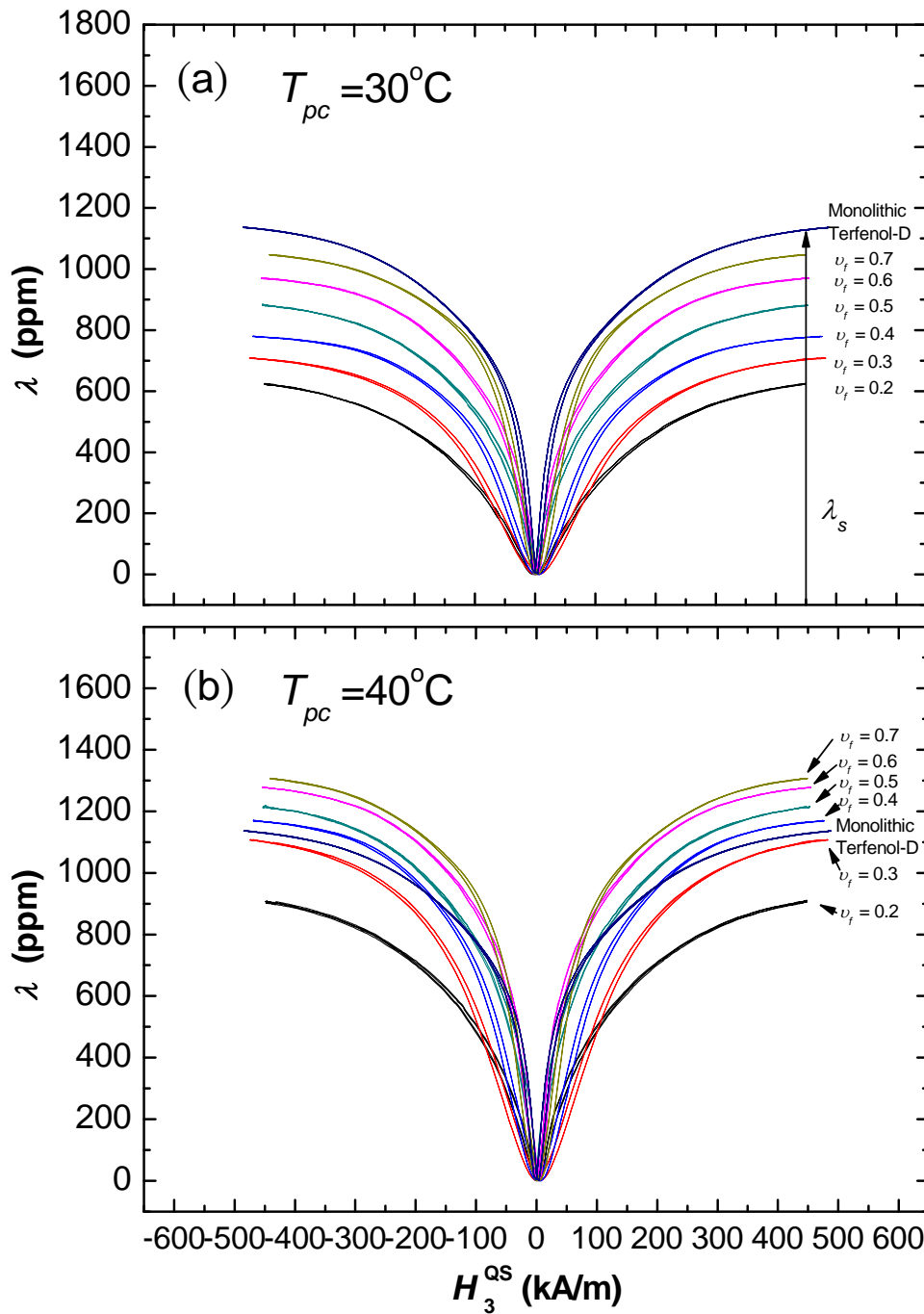


Fig. 3.4 $\lambda - H_3^{QS}$ curves for continuous-fiber composites with different ν_f for $T_{PC} =$ (a) 30, (b) 40, (c) 50, (d) 60, (e) 70, and (f) 80 °C. The $\lambda - H_3^{QS}$ curve for monolithic Terfenol-D is also enclosed for comparison. [To be continued]

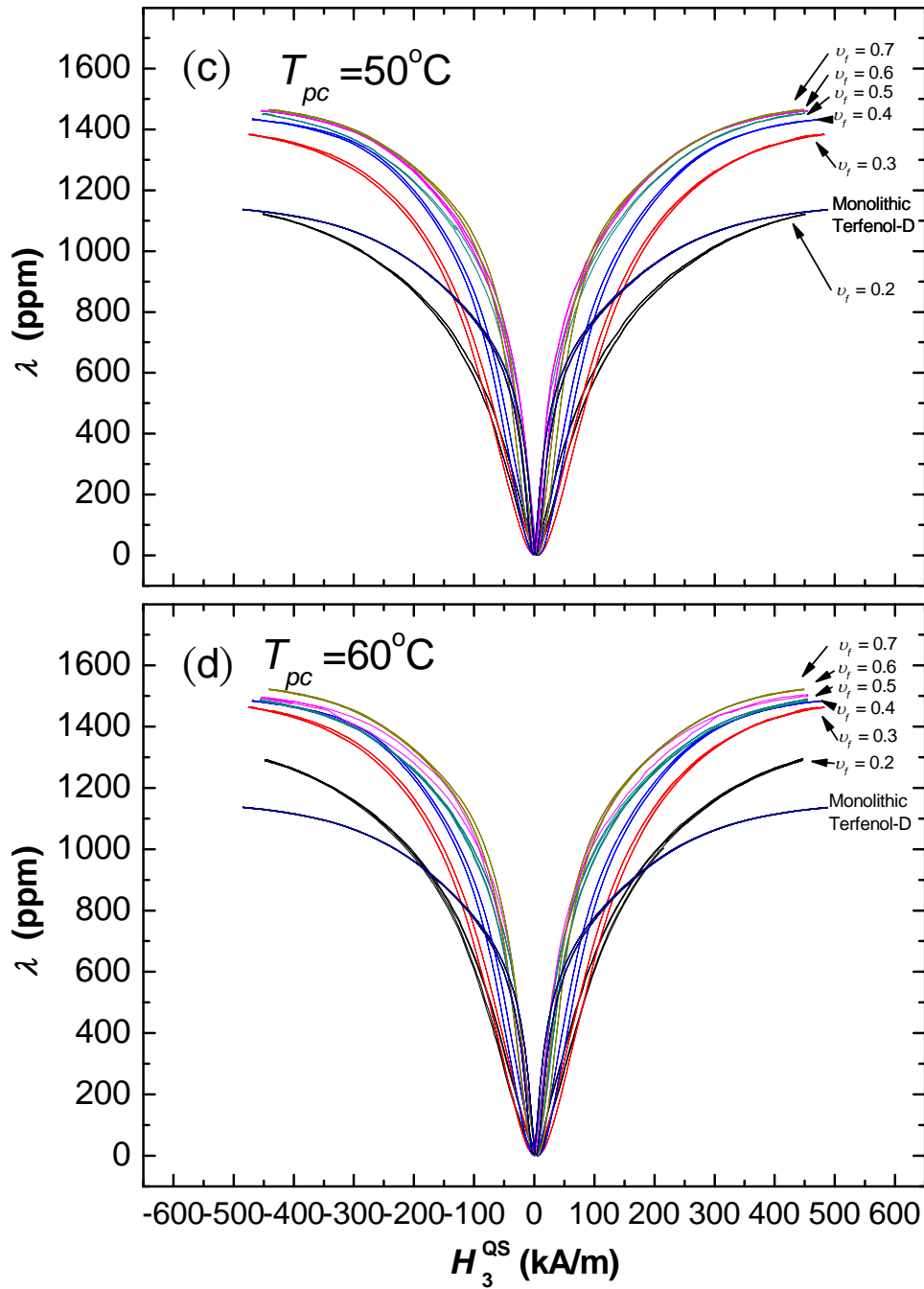


Fig. 3.4 $\lambda - H_3^{QS}$ curves for continuous-fiber composites with different v_f for $T_{PC} =$ (a) 30, (b) 40, (c) 50, (d) 60, (e) 70, and (f) 80 °C. The $\lambda - H_3^{QS}$ curve for monolithic Terfenol-D is also enclosed for comparison. [To be continued]

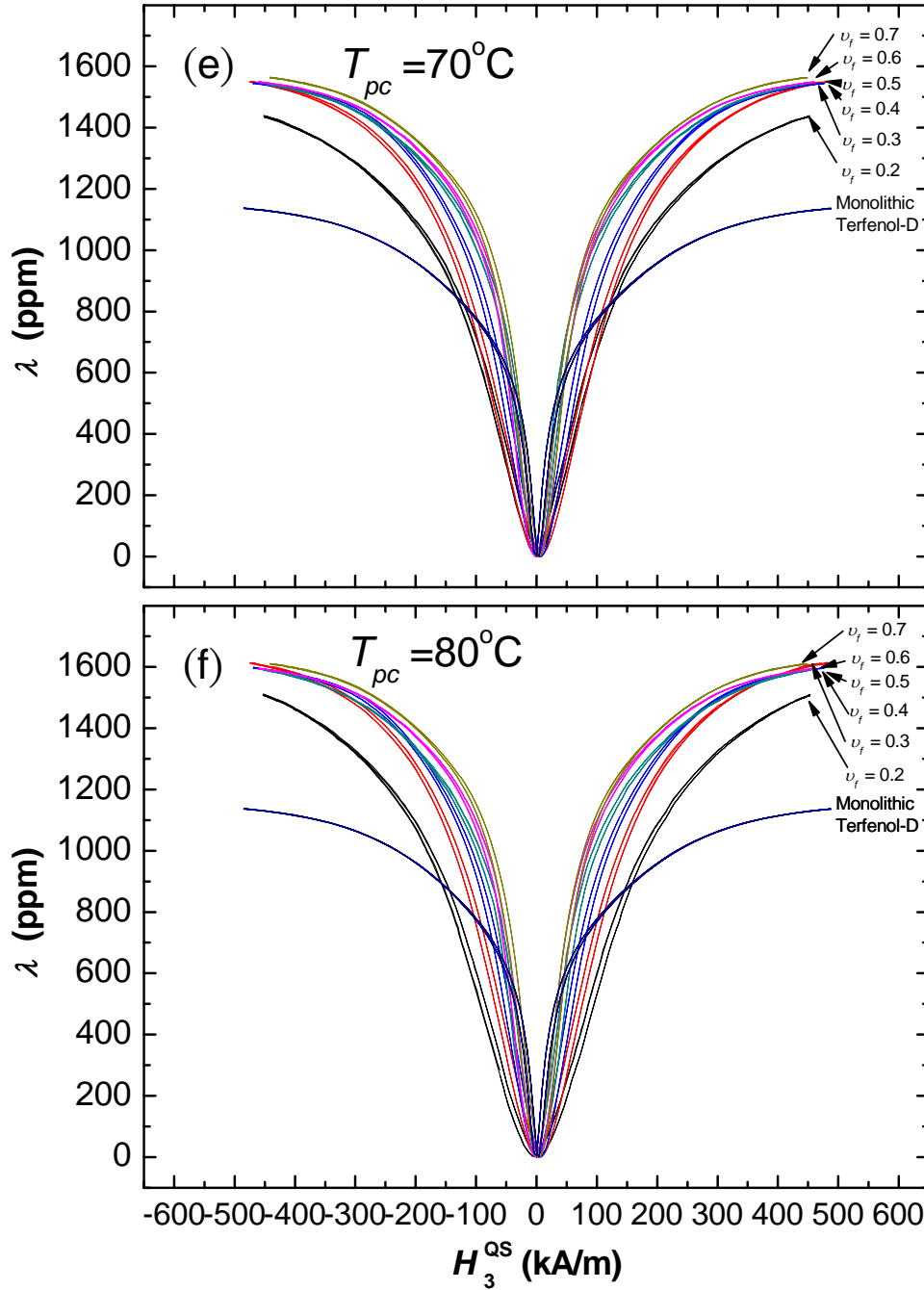


Fig. 3.4 $\lambda - H_3^{QS}$ curves for continuous-fiber composites with different ν_f for $T_{PC} =$ (a) 30, (b) 40, (c) 50, (d) 60, (e) 70, and (f) 80 °C. The $\lambda - H_3^{QS}$ curve for monolithic Terfenol-D is also enclosed for comparison.



Figure 3.5 shows similar $\lambda-H_3^{OS}$ plots of Fig. 3.4 at different T_{PC} for various ν_f . In Fig. 3.5(a), the continuous-fiber composite with $\nu_f = 0.2$ has a relatively small λ_S of 622 ppm at $T_{PC} = 30$ °C. This λ_S undergoes a quite steady development to 907, 1120, 1288, 1434, and 1510 ppm for the T_{PC} of 40, 50, 60, 70, and 80 °C, respectively. In Fig. 3.5(b)–(f), the composites with higher ν_f exhibit similar increasing trends with increasing T_{PC} owing to the effect of thermal-induced residual compressive stresses on domains in the continuous fibers through the epoxy curing process. In fact, these stresses are rather effective at low T_{PC} (e.g., 30 – 50 °C) than at higher T_{PC} (i.e., 60 – 80 °C).

For the composites with $\nu_f \geq 0.3$, the increase in λ_S is more rapid for $T_{PC} \leq 50$ °C. In the low T_{PC} range of ≤ 50 °C, the thermal-induced residual compressive stresses in the composites are developing with increasing T_{PC} . These stresses act on the Terfenol-D continuous fibers within the composites and thereby “preset” the corresponding numbers of non-180° domains as the effect of external stress loading on domains introduced in Section 1.2.4. Upon progressing towards an optimal residual stress level, the non-180° domain walls available in the composites are practically formed, and the increase in λ_S tends to be slowing down in the higher T_{PC} range of > 50 °C. In general, the composites with $\nu_f = 0.2 - 0.7$ possess large λ_S of 1510 – 1610 ppm at 450 kA/m. These λ_S are 34 and 43 % larger than the monolithic Terfenol-D (= 1130 ppm).

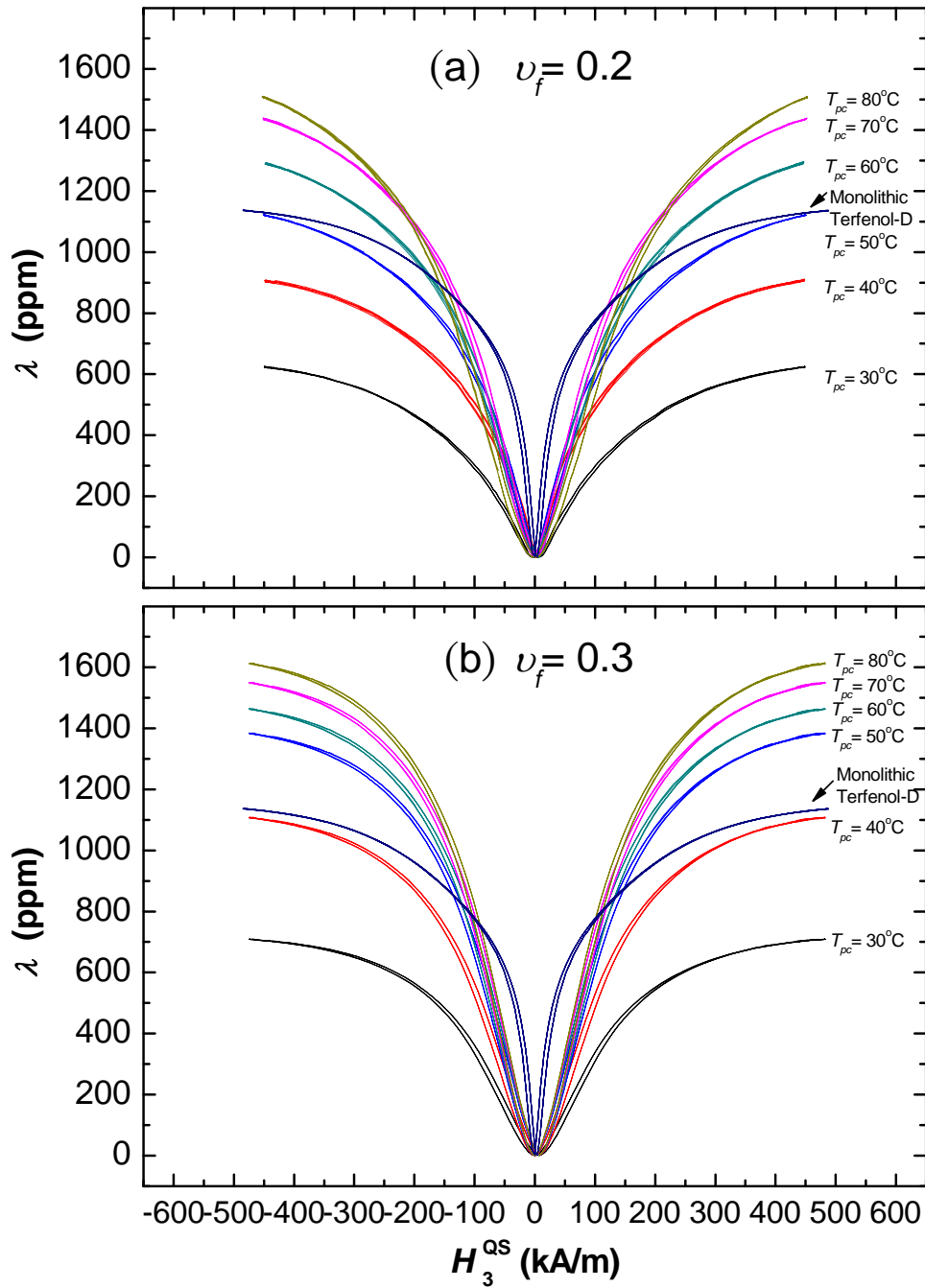


Fig. 3.5 $\lambda - H_3^{QS}$ curves for continuous-fiber composites with different T_{PC} for $\nu_f =$ (a) 0.2, (b) 0.3, (c) 0.4, (d) 0.5, (e) 0.6, and (f) 0.7. The $\lambda - H_3^{QS}$ curve for monolithic Terfenol-D is also enclosed for comparison. [To be continued]

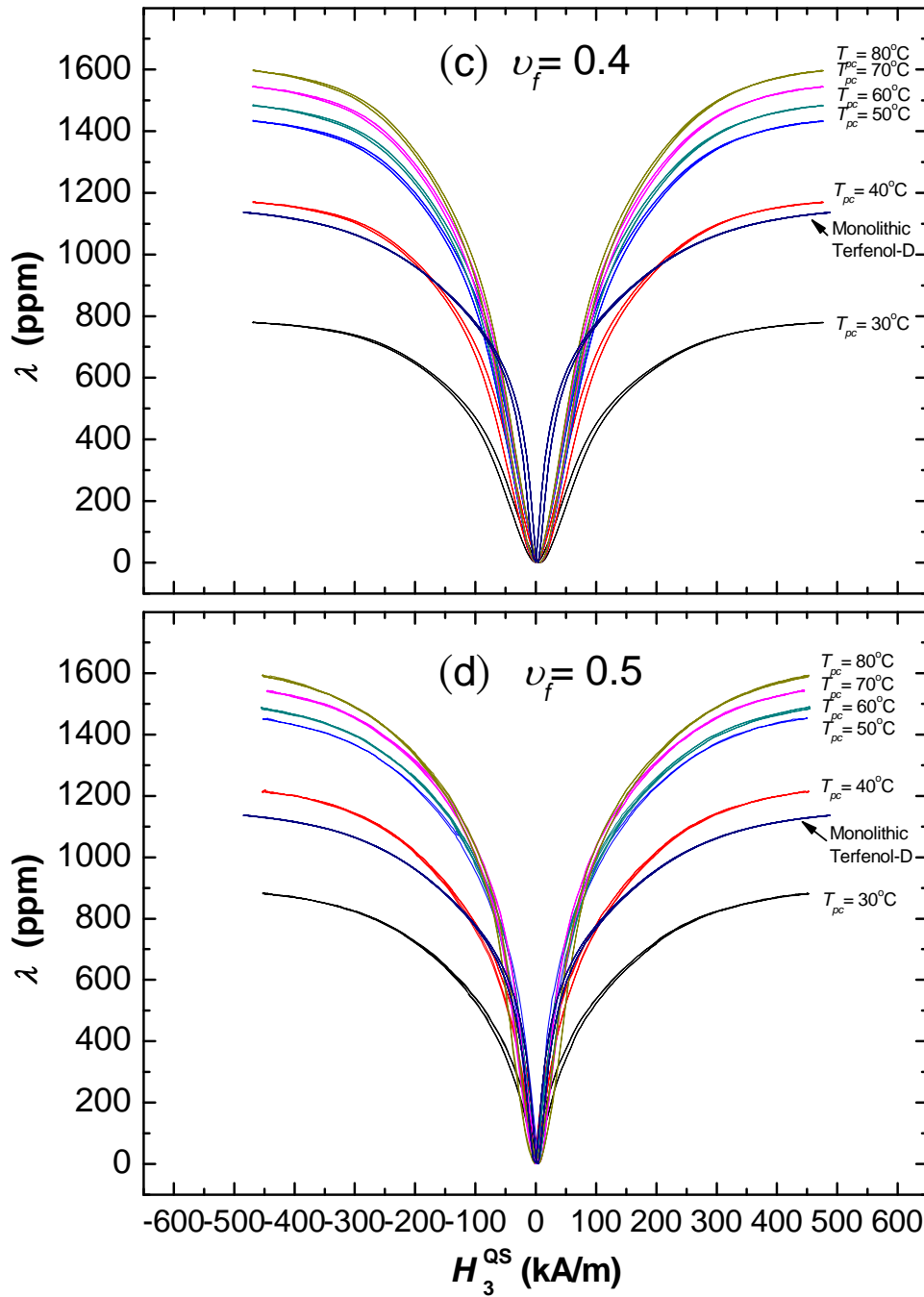


Fig. 3.5 $\lambda - H_3^{QS}$ curves for continuous-fiber composites with different T_{PC} for $\nu_f =$ (a) 0.2, (b) 0.3, (c) 0.4, (d) 0.5, (e) 0.6, and (f) 0.7. The $\lambda - H_3^{QS}$ curve for monolithic Terfenol-D is also enclosed for comparison. [To be continued]

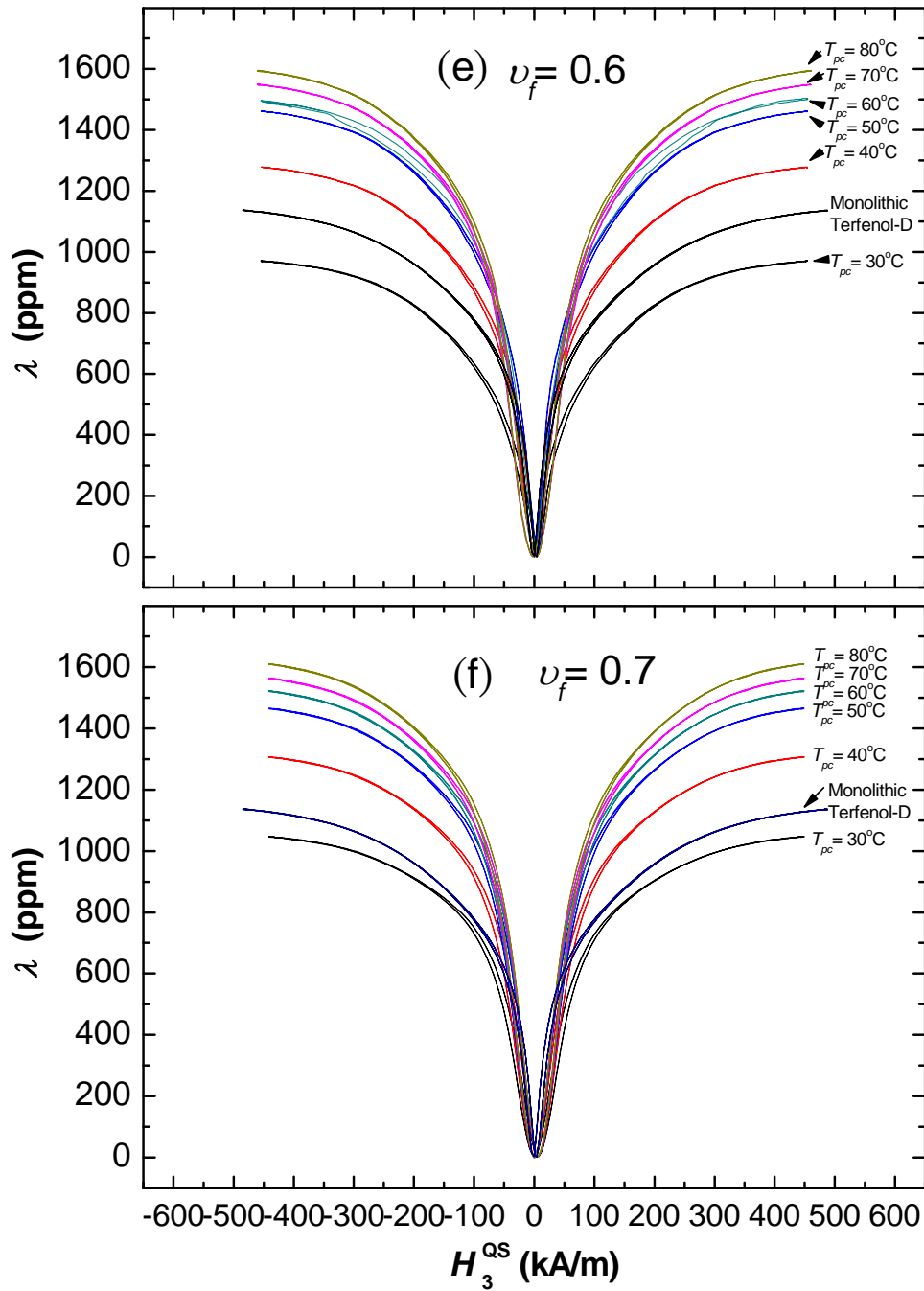


Fig. 3.5 $\lambda - H_3^{QS}$ curves for continuous-fiber composites with different T_{PC} for $\nu_f =$ (a) 0.2, (b) 0.3, (c) 0.4, (d) 0.5, (e) 0.6, and (f) 0.7. The $\lambda - H_3^{QS}$ curve for monolithic Terfenol-D is also enclosed for comparison.



Figure 3.6 displays the zoom-in plot of Fig. 3.4(f) for $T_{PC} = 80$ °C. It is clear that the magnetization jumping regions, which are the regions having nearly linear λ with H_3^{QS} and are mainly characterized by the motion of the non-180° domain walls, occur at relatively low H_3^{QS} levels of < 200 kA/m. The results can also be understood since the 180° domain wall motion produces magnetization without accompanying λ , while the non-180° domain wall motion produces changes in both magnetization and λ (Section 1.2.4). After the magnetization jumping regions (i.e., $H_3^{QS} > 200$ kA/m), the associated domains are relatively irreversible and immobile (Section 1.1.3); they can only be aligned under an elevated H_3^{QS} . For the composites with $\nu_f \geq 0.6$, almost common linear regions are observed for $H_3^{QS} < 50$ kA/m. The observations agree with what we have discussed and shown in Stages ‘2’ of Figs. 1.6 and 1.7 that the domain wall motion is principally controlled by the non-180° (or even 90°) domain state. Stage ‘1’ of Figs. 1.6 and 1.7, which is governed by the 180° domain wall motion, can also be seen at low H_3^{QS} of < 10 kA/m. However, the phenomenon becomes insignificant for the composites with $\nu_f > 0.5$.

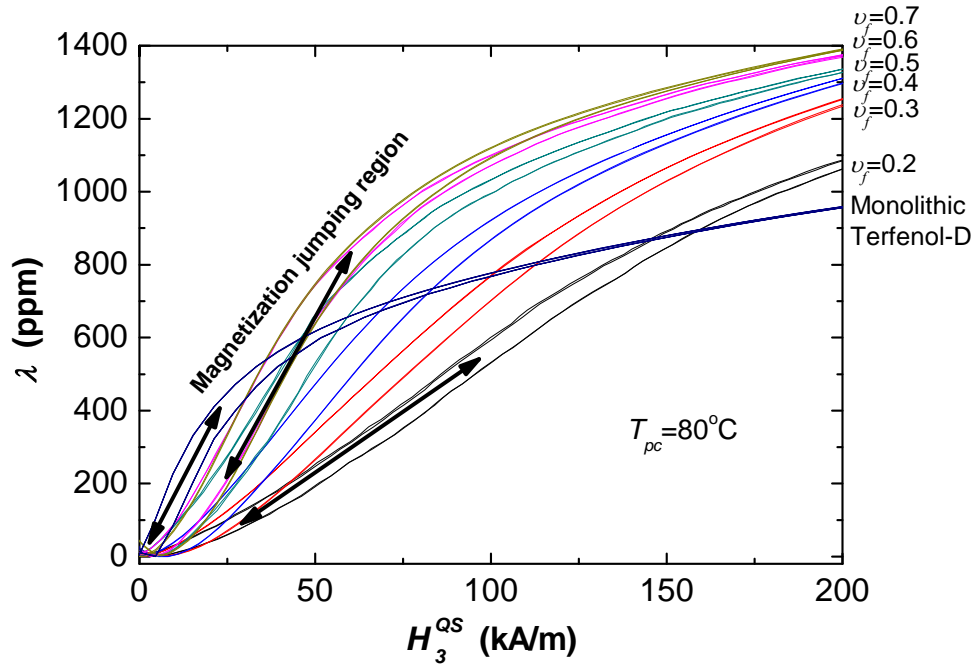


Fig. 3.6 $\lambda-H_3^{QS}$ curves for continuous-fiber composites ($T_{PC} = 80^\circ\text{C}$) and monolithic Terfenol-D. This is a zoom-in plot of Fig. 3.4(f) for $H_3^{QS} \leq 200$ kA/m. The arrows are drawn to indicate the magnetization jumping region characterized by the non- 180° domain wall motion.

Figure 3.7 shows the comparison of the $\lambda-H_3^{QS}$ response between the continuous-fiber composite, monolithic Terfenol-D, short-fiber composite, and particulate-chain composite. All the composites have the same ν_f of 0.5 and been post-cured at 80°C . It is seen that while all samples readily reach their λ_s at 450 kA/m, the continuous-fiber composite shows the largest $\lambda-H_3^{QS}$ response for almost the whole H_3^{QS} range and saturates with the highest λ_s of 1608 ppm. Importantly, this significantly large λ_s is 44, 56, and 144 % larger than the monolithic Terfenol-D (1115 ppm), short-fiber composite (1030 ppm), and particulate-chain composite (660 ppm), respectively. The higher λ_s when compared with the monolithic Terfenol-D is mainly attributed to the thermal-induced residual compressive stresses developed in



the continuous fibers during the thermal cure of the epoxy matrix. These built-in residual compressive stresses effectively create a preferred non-180° domain state in the continuous-fiber composite similar to the case of applying an external stress loading to assert an initial non-180° domain state in the monolithic Terfenol-D. By contrast, the unloaded monolithic material has comparatively little initial non-180° domains since the only internal stresses come from the ones generated by crystal defects and material processing [40]. The generally larger $\lambda-H_3^{QS}$ response, together with the higher λ_S , in comparison with both the short-fiber and particulate-chain composites is primarily due to a longer fiber length (a higher aspect ratio), which not only allows greater stress transfer from the continuous fibers to the epoxy matrix (Figs. 2.3 and 2.8) but also mitigates more effectively the effect of demagnetization fields arisen from the reduced fiber aspect ratio [33]. The overall enhancement as obtained in the fiber composites rather than in the particulate-chain composite is a result of the [112]-texturing in the fiber composites even though both the increased effect of λ (and λ_S) and decreased effect of demagnetization fields in the higher aspect ratio fibers are still active [33]. It is noted that the [112]-texturing, which has been shown to effectively increase deformation contributions from non-180° domain-wall motion in the short-fiber composites [40], should also have a significant effect on the continuous-fiber composite. The influence of stress will be discussed in more detail in Section 3.3.

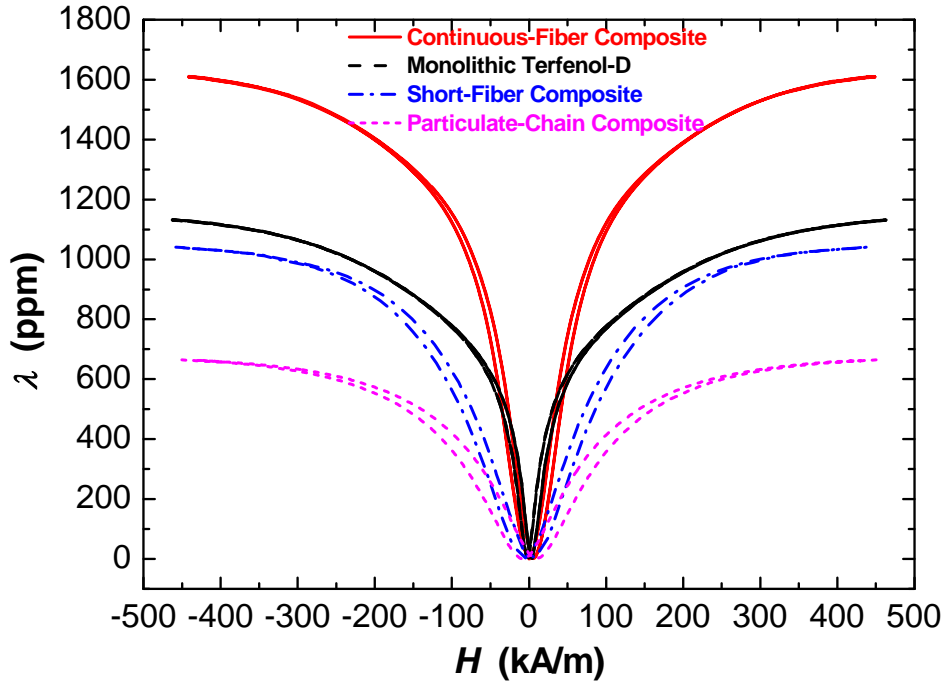


Fig. 3.7 $\lambda-H_3^{QS}$ curves for continuous-fiber composite, monolithic Terfenol-D, short-fiber composite, and particulate-chain composite. All the composites have the same ν_f of 0.5 and been post-cured at 80 °C.

Figure 3.8 relates λ_S and ν_f of the continuous-fiber composites at different T_{PC} . The λ_S values of the monolithic Terfenol-D, short-fiber composite ($\nu_f = 0.5$), particulate-chain composite ($\nu_f = 0.5$), and epoxy are also included. The prediction of λ_S based on the classical composite formulations for the lower and upper bounds as expressed, respectively, in Eqs. (3.1) and (3.2) are plotted on the same figure as well.

$$E_3^H = \frac{E_3^{T-D} E^{Epoxy}}{\nu_f E^{Epoxy} + (1 - \nu_f) E_3^{T-D}}, \quad (3.1)$$

$$E_3^H = \frac{\nu_f E_3^{T-D}}{\nu_f + (1 - \nu_f) \frac{S_{33}^{T-D}}{S_{11}^{Epoxy}}}. \quad (3.2)$$

It is clear that the λ_S values of the continuous-fiber composites at $T_{PC} = 30$ °C follow readily with the predication of the upper bound formulation, reflecting the successful



embedding the one-dimensionally aligned continuous fibers (fiber aspect ratio = 45:1) in a three-dimensionally connected epoxy matrix. However, the upper bound formulation is unable to predict the dramatically increased λ_S values at elevated T_{PC} of 40 – 80 °C. Although the short-fiber composite ($\nu_f = 0.5$) has a reduced fiber aspect ratio of 4:1, the residual compressive stresses developed during the post-curing process at 80 °C have improved its λ_S value to slightly exceed the values of the continuous-fiber composite ($\nu_f = 0.5$) at $T_{PC} = 30$ °C and the upper bound formulation. The particulate-chain composite ($\nu_f = 0.5$) shows the quasi-behavior bounded by the upper and lower bound predictions. It is likely for the low- ν_f particulate-chain composites ($\nu_f < 0.5$) to follow the trend of the lower bound formulation and for the high- ν_f particulate-chain composites ($\nu_f > 0.5$) to pursue the trend of the upper bound formulation. The mechanism and trends of λ_S at elevated T_{PC} in our continuous-fiber composites will be discussed with a physical model in Section 3.3.

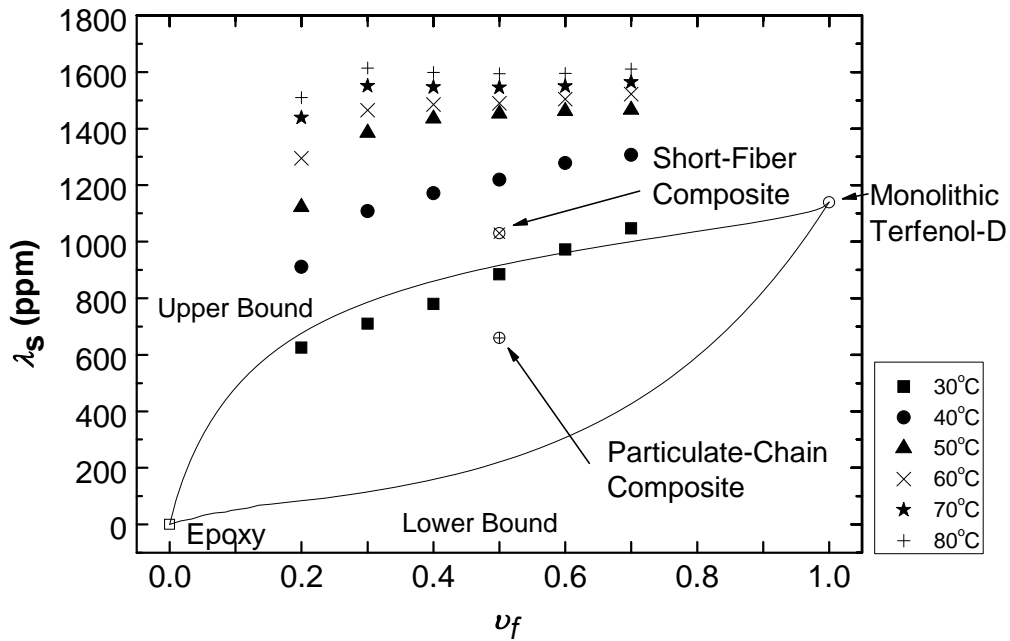


Fig. 3.8 λ_s versus ν_f for continuous-fiber composites ($\nu_f = 0.2 - 0.7$) at different T_{PC} , monolithic Terfenol-D, short-fiber composite ($\nu_f = 0.5$) at $T_{PC} = 80^\circ\text{C}$, particulate-chain composite ($\nu_f = 0.5$) at $T_{PC} = 80^\circ\text{C}$, and epoxy, where the symbols and lines represent the experimental and calculated data, respectively.

Figure 3.9 illustrates the H_3^{QS} dependence of the quasistatic (differential) strain coefficient (d_{33}^{QS}) for the continuous-fiber composites at different T_{PC} . All composites exhibit similar quantitative increasing trends with increasing T_{PC} , except for the composite with $\nu_f = 0.2$. The reduction in $d_{33}^{QS\max}$ at $T_{PC} = 80^\circ\text{C}$ indicates the use of exceedingly large residual compressive stresses in the composite. The optimal T_{PC} should be 70°C instead of 80°C . The discussion will be more detail in Section 3.3.

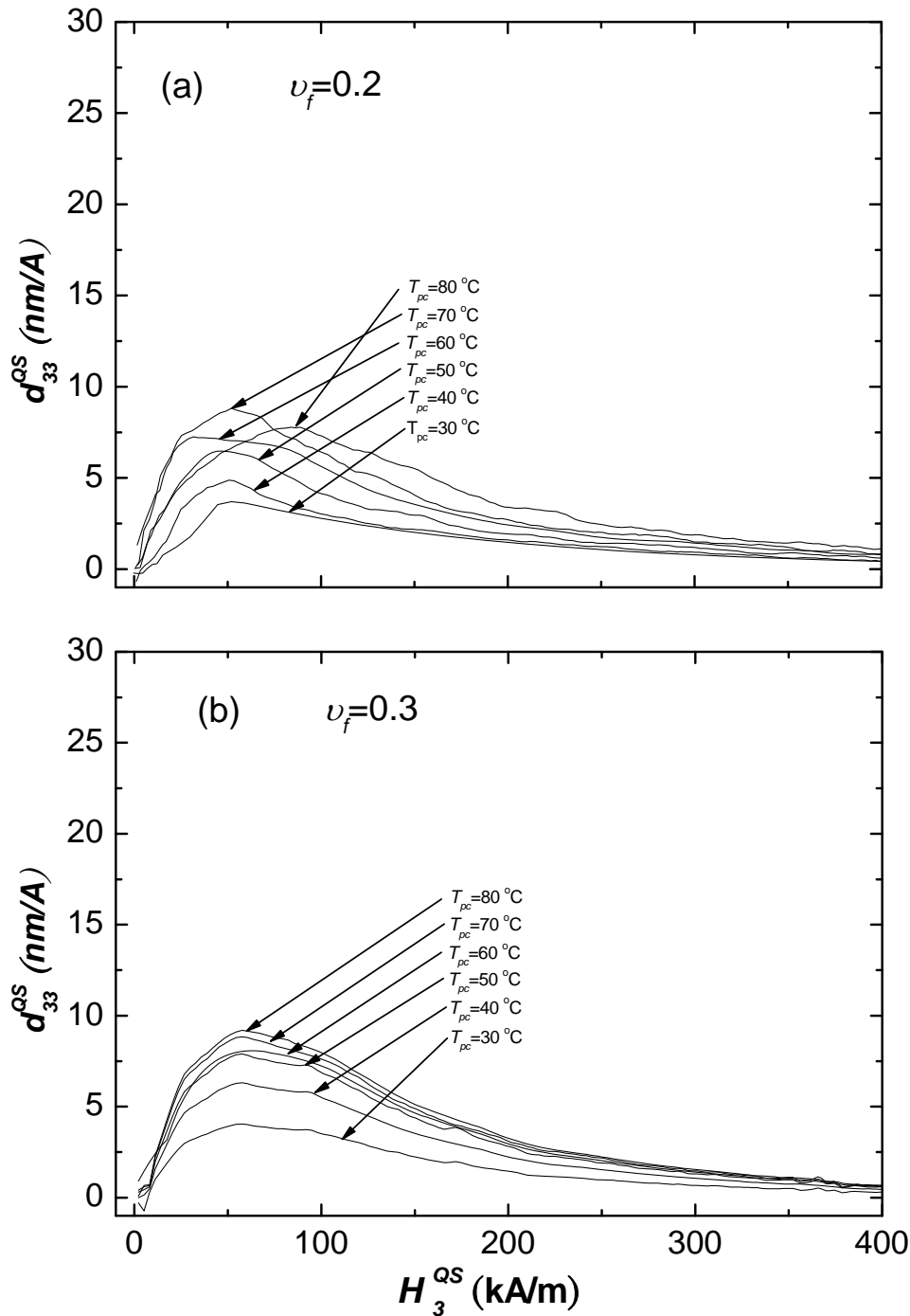


Fig. 3.9 $d_{33}^{QS} - H_3^{QS}$ curves for continuous-fiber composites with different T_{PC} of 30 to 80 °C for v_f = (a) 0.2, (b) 0.3, (c) 0.4, (d) 0.5, (e) 0.6, and (f) 0.7. [To be continued]

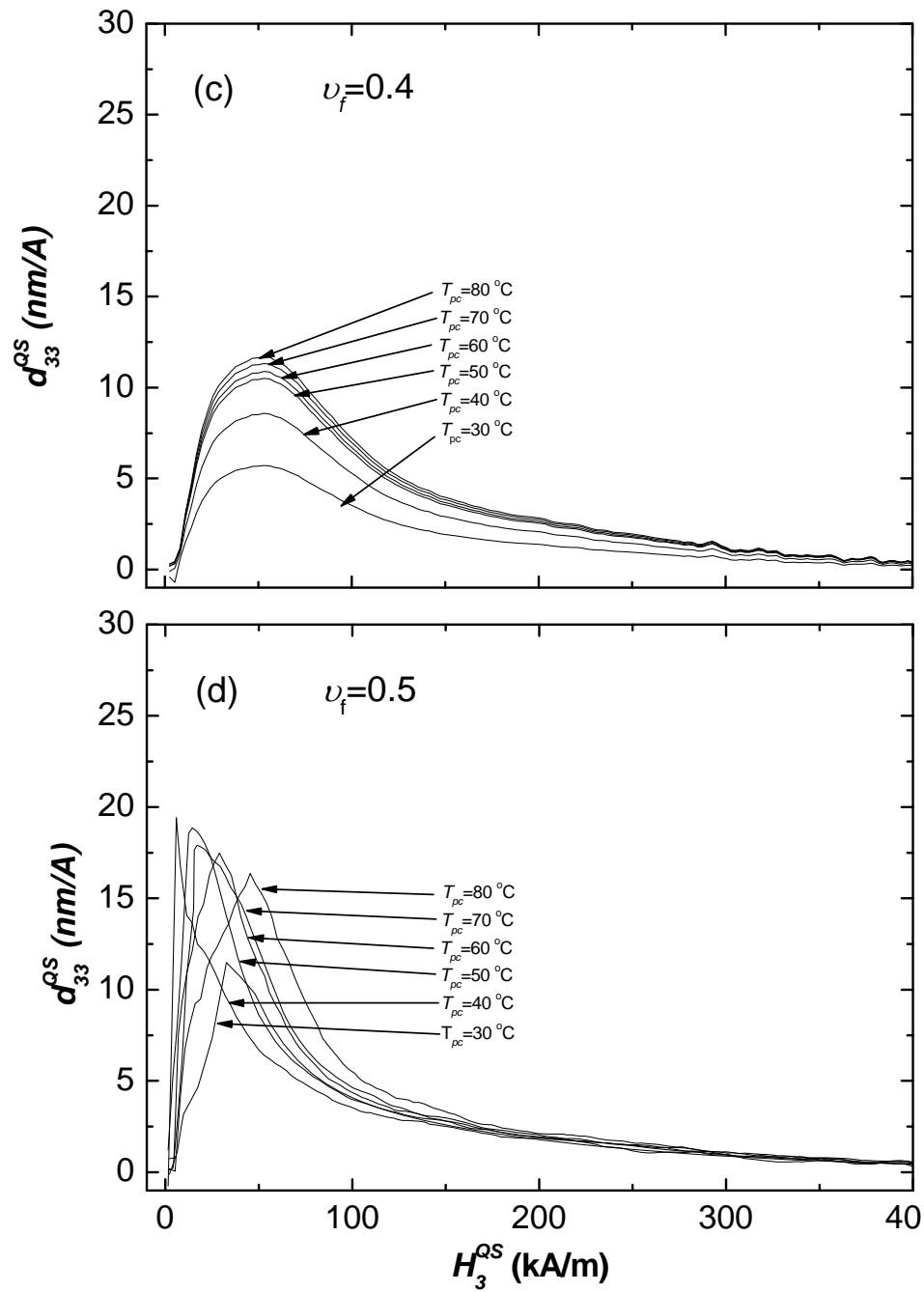


Fig. 3.9 $d_{33}^{QS} - H_3^{QS}$ curves for continuous-fiber composites with different T_{PC} of 30 to 80 °C for $v_f =$ (a) 0.2, (b) 0.3, (c) 0.4, (d) 0.5, (e) 0.6, and (f) 0.7. [To be continued]

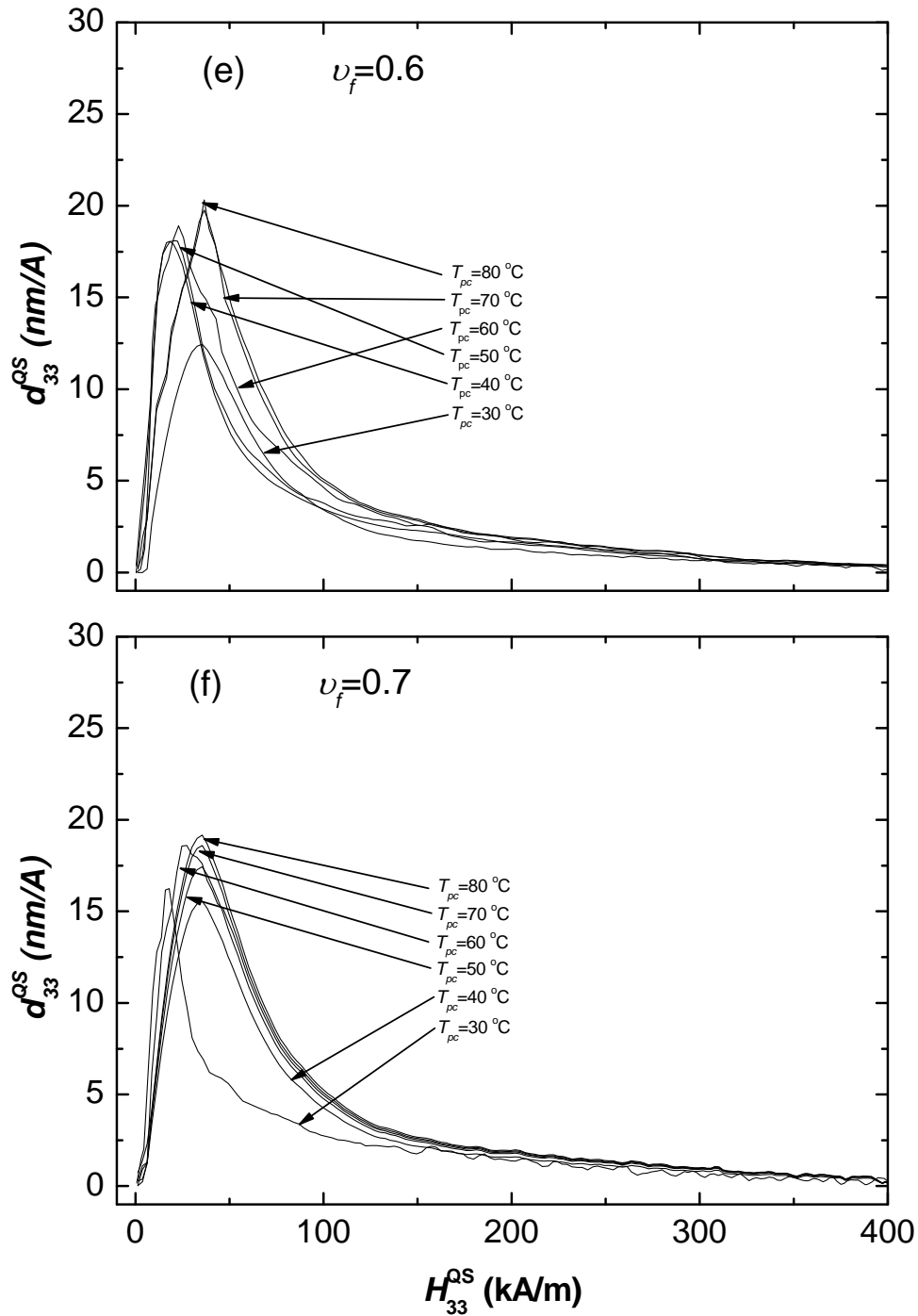


Fig. 3.9 $d_{33}^{QS} - H_3^{QS}$ curves for continuous-fiber composites with different T_{PC} of 30 to 80 °C for $\nu_f =$ (a) 0.2, (b) 0.3, (c) 0.4, (d) 0.5, (e) 0.6, and (f) 0.7.

Fig. 3.10 shows $d_{33\max}^{QS}$ versus ν_f for the continuous-fiber composites at different T_{PC} . The values of $d_{33\max}^{QS}$ for the monolithic Terfenol-D, short-fiber



3. Quasistatic Material Properties of Continuous-Fiber Composites

THE HONG KONG POLYTECHNIC UNIVERSITY

composite ($\nu_f = 0.5$, $T_{PC} = 80^\circ\text{C}$), particulate-chain composite ($\nu_f = 0.5$, $T_{PC} = 80^\circ\text{C}$), and epoxy are included, in conjunction with the classical composite formulations for the lower and upper bounds as stated in Eqs. (3.3) and (3.4), respectively.

$$d_{33\max}^{QS} = \frac{d_{33\max}^{T-D} d_{33\max}^{Epoxy}}{\nu_f d_{33\max}^{Epoxy} + (1 - \nu_f) d_{33\max}^{T-D}}, \quad (3.3)$$

$$d_{33\max}^{QS} = \frac{\nu_f d_{33\max}^{T-D}}{\nu_f + (1 - \nu_f) \frac{S_{33}^{T-D}}{S_{11}^{Epoxy}}}. \quad (3.4)$$

Only the continuous-fiber composites with sufficiently high $\nu_f (>0.5)$ can exceed the upper bound's $d_{33\max}^{QS}$ by balancing the magnetic and mechanical energies.

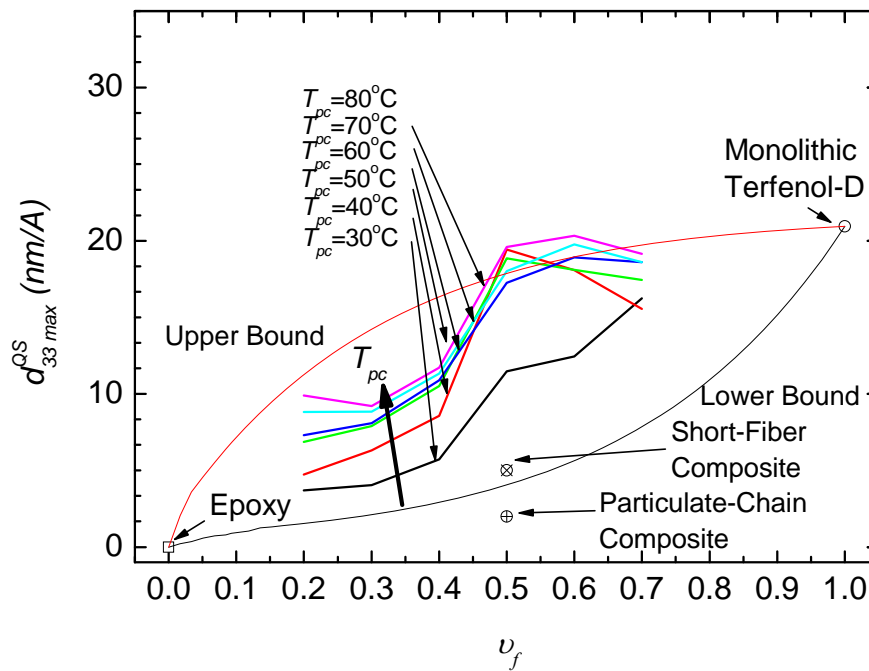


Fig. 3.10 $d_{33\max}^{QS}$ versus ν_f for continuous-fiber composites ($\nu_f = 0.2 - 0.7$) at different T_{PC} , monolithic Terfenol-D, short-fiber composite ($\nu_f = 0.5$) at $T_{PC} = 80^\circ\text{C}$, particulate-chain composite ($\nu_f = 0.5$) at $T_{PC} = 80^\circ\text{C}$, and epoxy, where the symbols and lines represent the experimental and calculated data, respectively.



3.2.2.2 Magnetic Properties

Since the thermal residual compressive stresses induced in the continuous-fiber composites mainly influences the non-180° domain state rather than the 180° domain state, the magnetic properties, which are more dependent on the 180° domain state, are only presented for $T_{PC} = 80$ °C for simplicity reason in this section.

Figure 3.11 shows the $B_3^{QS} - H_3^{QS}$ loops of the continuous-fiber composites and the monolithic Terfenol-D. The saturation magnetic induction (B_3^{QS}) of each sample as measured at $H_3^{QS} = 320$ kA/m is extracted from Fig. 3.11 and shown in Fig. 3.12 as a function of ν_f . From Fig. 3.12, B_3^{QS} is approximately linear proportional to its ν_f , elucidating that the magnetization processes only relate to the soft magnetic material Terfenol-D. The value of each B_3^{QS} is much lower than the most common pure soft magnetic material iron of 2.2 T. Monolithic Terfenol-D possesses the highest B_3^{QS} and B_{3s}^{QS} with the same H_3^{QS} .

It is showed in Fig. 3.12 that B_3^{QS} is almost a linear function of ν_f . This is originated from that the magnetization is only related to the magnetic material Terfenol-D in the composites. By the rule of mixture, B_3^{QS} can be determined by:

$$B_3^{QS} = \nu_f B_3^{QST-D} + (1 - \nu_f) B_3^{QSEpoxy} , \quad (3.5)$$

where the superscripts T-D and Epoxy denote the Terfenol-D and epoxy phases, respectively. The measured B_3^{QS} values in Fig. 3.12 agree reasonably with the predicted values using Eq. (3.5).

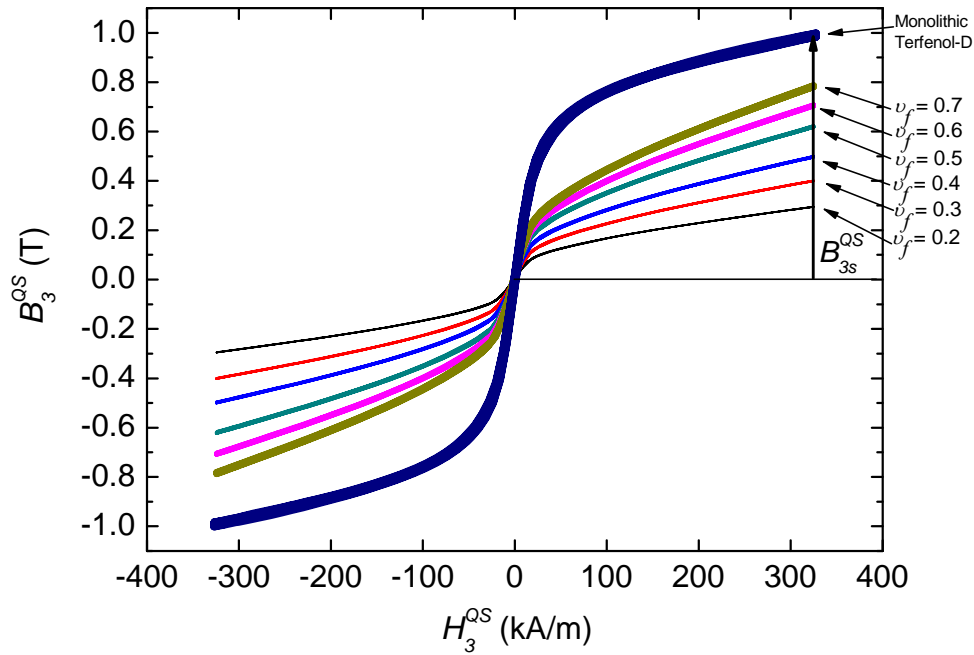


Fig. 3.11 $B_3^{QS} - H_3^{QS}$ loops of continuous-fiber composites ($T_{PC} = 80 \text{ }^\circ\text{C}$) and monolithic Terfenol-D.

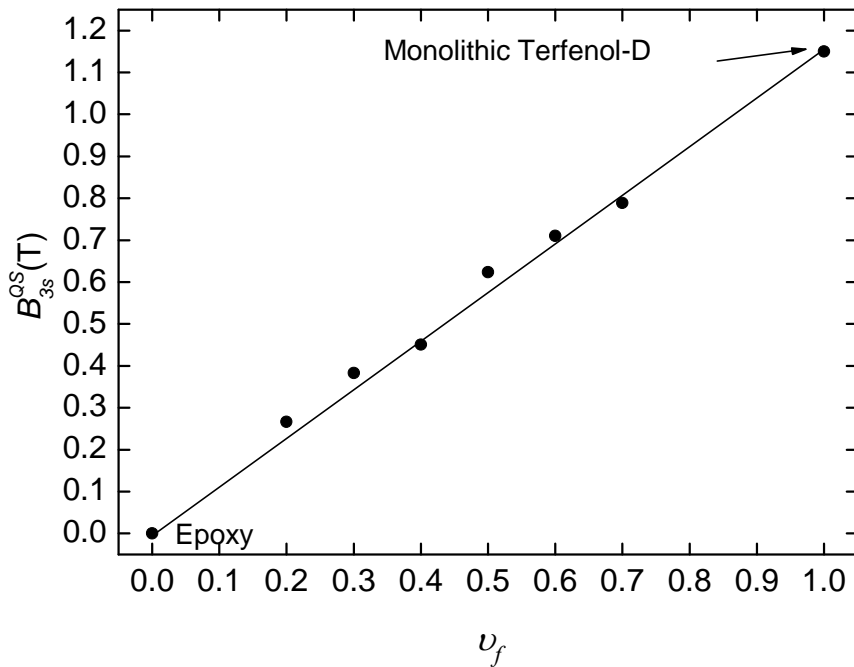


Fig. 3.12 B_{3s}^{QS} versus v_f for continuous-fiber composites, Terfenol-D, and epoxy. The symbols and line represent the experimental and calculated data, respectively.



Figure 3.13 plots μ_{r33}^{QS} as a function of H_3^{QS} . μ_{r33}^{QS} increases to its maximum value ($\mu_{r33 \max}^{QS}$) at H_3^{QS} of about 5 kA/m. Thereafter, μ_{r33}^{QS} decreases with increasing H_3^{QS} . When most of the domain-wall motions are complete, there often remain domains with nonzero components of magnetization at certain angles to the H_3^{QS} direction. The magnetization in these domains must be aligned along the H_3^{QS} direction to minimize the potential energy described by $M_3^{QS} \cdot B_3^{QS}$. This process generally requires more energy than domain-wall motions because it involves displacing the magnetization away from an “easy” direction. When H_3^{QS} is sufficiently large, the sample is in a state of magnetic saturation $B_{3s}^{QS} = \mu_0 (H_3^{QS} + M_{3s}^{QS})$ (Fig. 3.11). From Fig. 3.14, composites with higher ν_f maintain higher μ_{r33}^{QS} and $\mu_{r33 \max}^{QS}$. Specifically, $\mu_{r33 \max}^{QS}$ is also approximately linear proportional to ν_f , as in the case of B_{3s}^{QS} in Fig. 3.12.

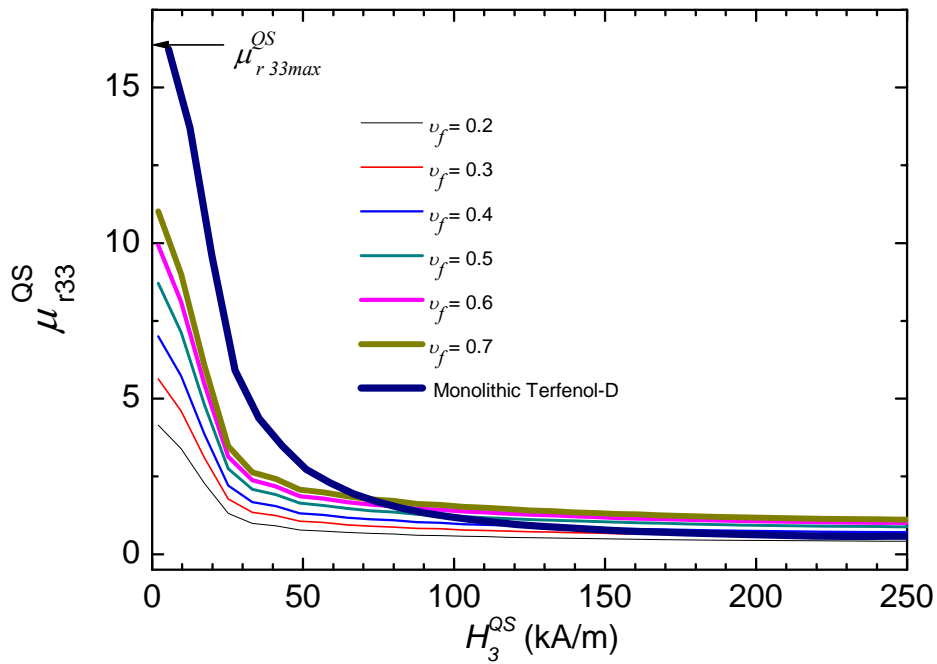


Fig. 3.13 μ_{r33}^{QS} versus H_3^{QS} for continuous-fiber composites ($T_{PC} = 80\text{ }^\circ\text{C}$) and monolithic Terfenol-D.

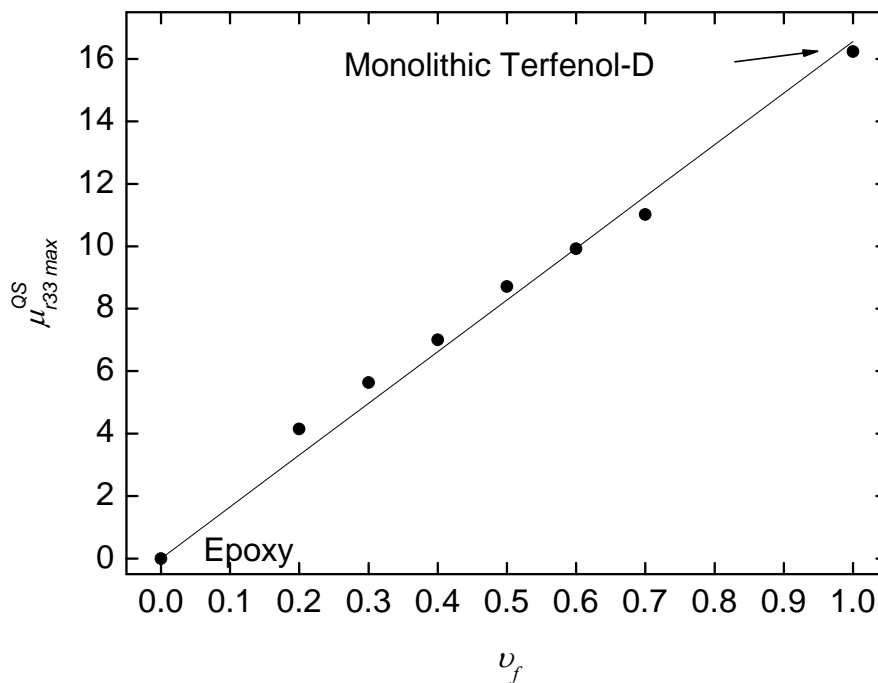


Fig. 3.14 $\mu_{r33\text{max}}^{QS}$ versus v_f for continuous-fiber composites, Terfenol-D, and epoxy. The symbols and line represent the experimental and calculated data, respectively.



Application of a relatively weak H_3^{QS} produces motion of domain walls so as to expand the volume of those domains having the largest component of M_3^{QS} along the H_3^{QS} direction. (The macroscopic form of the energy of an atomic moment μ_m in a B field, $U = -\mu_m \cdot B$, is $NU = -\mu_m \cdot BV$, where V is the volume of the domain of magnetization M [37].) The $M_3^{QS} - H_3^{QS}$ loops of continuous-fiber composites and monolithic Terfenol-D are plotted in Fig. 3.15. As expected, M_3^{QS} increases with ν_f . The rapid increase of M_3^{QS} in high- ν_f composites with increasing H_3^{QS} shows the behavior of 180° domain-wall motion, which is equivalent to a large $\mu_{r33 \max}^{QS}$ in Fig. 3.13. Oppositely, M_3^{QS} of low- ν_f composites increases more slowly with H_3^{QS} due to the large amount of work done by the non- 180° process. Fig. 3.16 reveals that M_{3s}^{QS} remains a proportional relationship with ν_f .

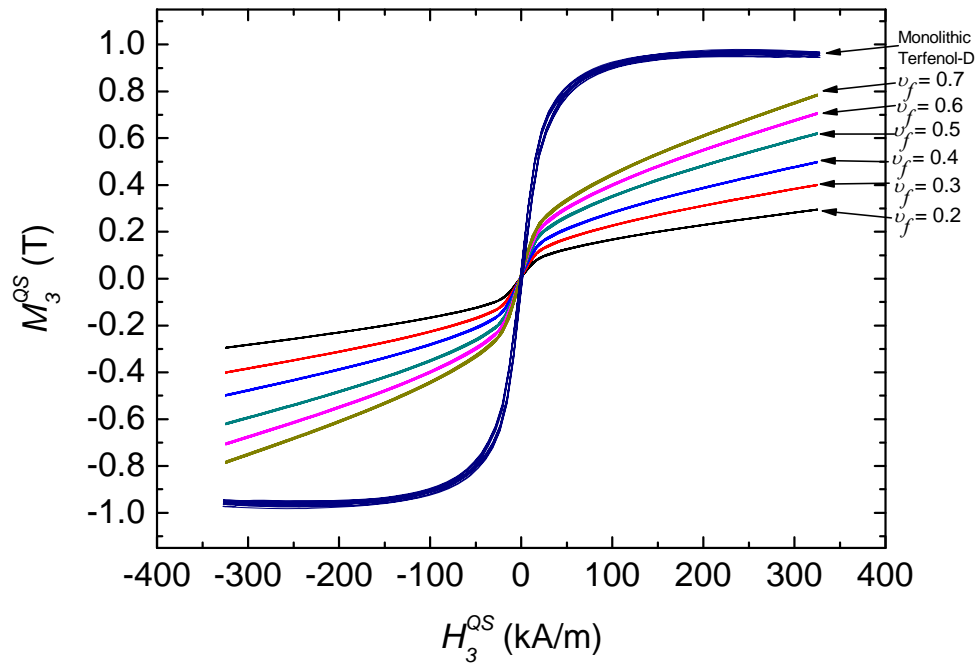


Fig. 3.15 $M_3^{QS} - H_3^{QS}$ loops of continuous-fiber composites ($T_{PC} = 80 \text{ }^\circ\text{C}$) and monolithic Terfenol-D.

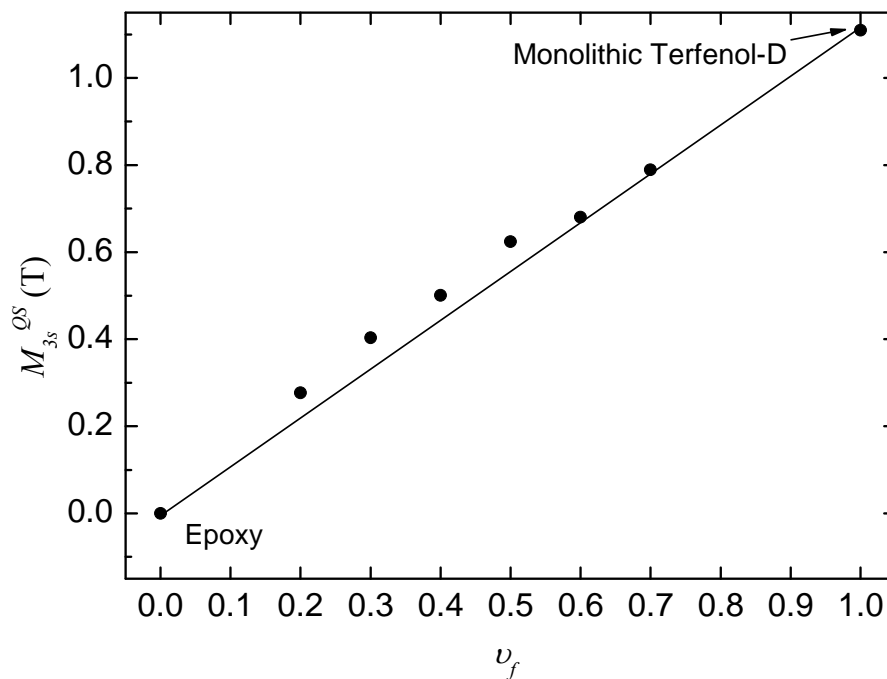


Fig. 3.16 M_{3s}^{QS} versus ν_f for continuous-fiber composites, Terfenol-D, and epoxy. The symbols and line represent the experimental and calculated data, respectively.



3.2.2.3 Magnetization and Magnetostriction Processes

To determine the relevance between the observed magnetization and magnetostriction processes in the previous sections, and to explain the observed processes based on Section 1.2.3, the related data have been extracted from Fig. 3.4(f) and Fig. 3.15 to construct Fig. 3.17 and Fig. 3.18. The $\lambda - M_3^{QS}$ curves in Fig. 3.17 demonstrates that M_3^{QS} in the continuous-fiber composites is fully controlled by the M_3^{QS} of the Terfenol-D fibers. In the low field region, the faster magnetization process in high- ν_f composites gives rise to steep slope for the $M_3^{QS} - H_3^{QS}$ curves in Fig. 3.18, which bring the higher values of M_3^{QS} / M_{3s}^{T-D} , where M_{3s}^{T-D} is the saturation magnetization of monolithic Terfenol-D, resulting in a relatively larger λ compared to that of low- ν_f composites. The magnetostriction versus magnetization relation that has been described in Section 1.2.3 is as follow:

$$\frac{\lambda}{\lambda_s} = \frac{3}{2} \left(\frac{M_3^{QS}}{M_{3s}^{QS}} \right)^2. \quad (3.6)$$

Equation (3.6) is drawn in Figs. 3.18 for comparison with our samples. It is found that composite with $\nu_f \geq 0.5$ is close to Eq. (3.6), which is the optimal stress loading curve. The composites with $\nu_f < 0.5$ show flattening in the low M_3^{QS} / M_{3s}^{T-D} region, indicating an excessive stress loading on the composites. With increasing M_3^{QS} / M_{3s}^{T-D} , λ approaches to its λ_s upon the completion of the non-180° domain wall motion. However, the magnetization processes continue until the alignment of all domains along the H_3^{QS} direction so that the curves become steeper in the middle region and approach a saturated state when M_3^{QS} / M_{3s}^{T-D} is close to 1.



The curves for composites with lower ν_f are located below those of higher ν_f samples, suggesting the formation of different demagnetized states by the residual compressive stresses in the composites.

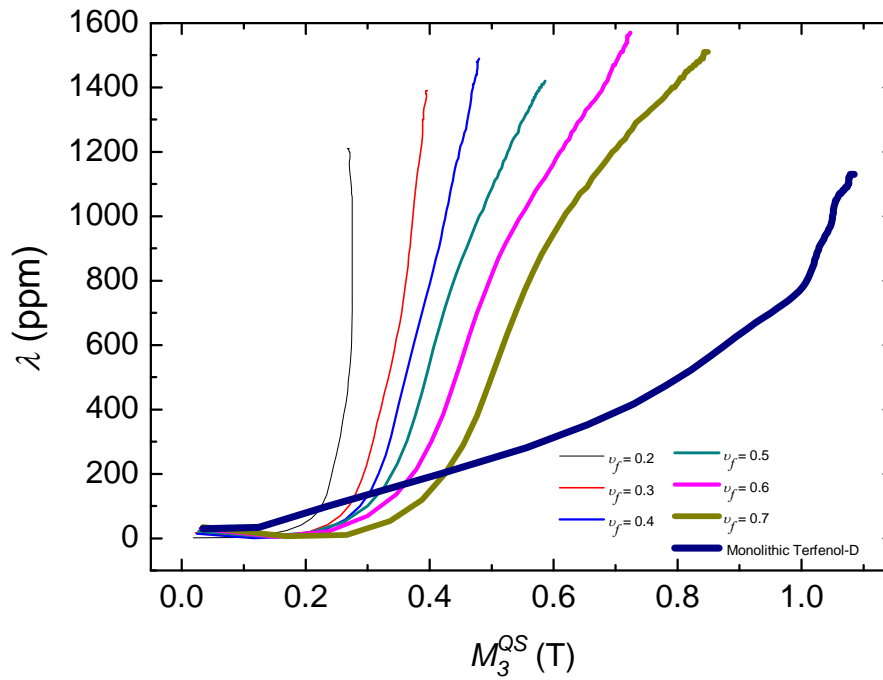


Fig. 3.17 λ versus M_3^{QS} for continuous-fiber composites and monolithic Terfenol-D.

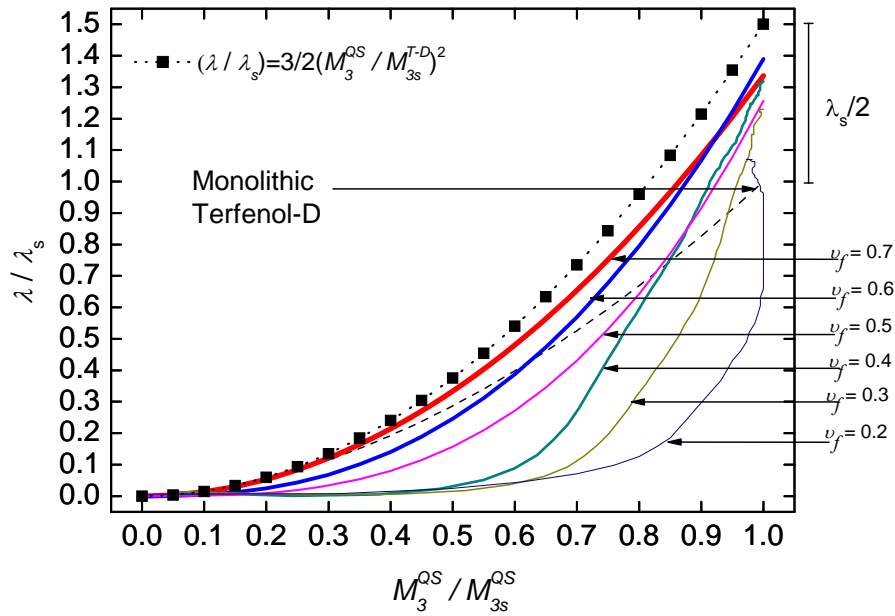


Fig. 3.18 Normalized magnetostriction versus magnetization curves for continuous-fiber composites and monolithic Terfenol-D.



3.3 Theoretical Implication with a Physical Model

3.3.1 Formulation of Physical Model

In Section 3.2.2, the significantly large λ_S in excess of 1600 ppm at 400 kA/m is observed in the continuous-fiber composites with $T_{PC} = 80$ °C in comparison with the smaller λ_S of 1115 ppm in monolithic Terfenol-D under externally unloaded conditions. Moreover, d_{33}^{OS} of the composites are higher than the monolithic Terfenol-D. The classical composite formulation for the upper and lower bounds [41,42] are unable to predict the magnetostrictive properties of our continuous-fiber composites. The thermal-induced residual compressive stresses actually play a major role in improving the observed magnetostrictive properties of the composites due to the presence or “preset” of the preferred non-180° (or 90°) domain state. In this section, a thermal stress-mediated continuous-fiber composite model is developed to describe the improved magnetostrictive properties of the composites by including the effect of thermal residual compressive stresses produced by the post-curing process in the classical composite formulation for the upper bound.

In fact, the coefficient of thermal expansion of Terfenol-D ($\alpha^{T-D} = 8 \times 10^{-6}$ /°C) is about one-eighth of the CTE of epoxy ($\alpha^{Epoxy} = 60 \times 10^{-6}$ /°C) (Table 3.1). The epoxy matrix tends to contract more than the Terfenol-D fibers in a given continuous-fiber composite, thereby inducing residual compressive stresses on the embedded Terfenol-D fibers during the cooling phase of the post-curing process. Since the composites possess highly anisotropic properties, the axial stress component should have the predominant effect over the transverse stress component. For simplicity, the horizontal stress component is neglected. Hence, the thermal-



induced residual (axial) compressive stresses (σ_T) due to the thermal mismatch between the Terfenol-D fiber and the epoxy matrix can be expressed as

$$\sigma_T = -E^{Epoxy} \cdot (\alpha^{Epoxy} - \alpha^{T-D}) \cdot \Delta T \cdot \frac{(1 - \nu_f)}{\nu_f}, \quad (3.7)$$

where E^{Epoxy} is the Young's modulus of the epoxy matrix; α^{Epoxy} and α^{T-D} are the coefficients of thermal expansion of epoxy matrix and Terfenol-D fibers, respectively; ΔT is the temperature difference between the post-curing temperature (T_{PC}) of the composite and room temperature (30 °C); and ν_f is the volume fraction of the Terfenol-D fibers. Equation (3.6) indicates that one can increase σ_T by increasing α^{Epoxy} , ΔT , or decreasing ν_f . In our composites, ΔT is varied by adjusting T_{PC} from 30 to 80 °C with respect to room temperature (30 °C) for various ν_f of 0.2 – 0.7.

It is known from the magnetization and magnetostriction processes in Figs. 1.8 and 1.9 that the combined external stress loading and applied H field on a magnetostrictive material at $T < T_C$ will lead to the production of the total allowable strain in the material due to the motion of the available 90° domain walls. As we have intentionally created σ_T to act as the external stress loading, the maximum achievable magnetostrictive strain in the Terfenol-D fibers [$\lambda_S(\sigma_T)$] thus consists of two equivalent terms with the first term representing the H -induced saturation magnetostrictive strain (λ_S) and the second term depicting the σ_T -induced preloading strain (λ_{σ_T}) as

$$\lambda_S(\sigma_T) = \lambda_S + \lambda_{\sigma_T}, \quad (3.8)$$



$$\lambda_{\sigma_T} = \frac{\lambda_S}{2} \cdot \tanh\left(\frac{2 \cdot \sigma_T}{\sigma_{TS}}\right). \quad (3.9)$$

It is noted that λ_{σ_T} in Eq. (3.9) attains its maximum value of $\lambda_S/2$ when σ_T approaches σ_{TS} in the hyperbolic tangent function. This indicates the success creation of the maximum number of non-180° domain walls in the Terfenol-D fibers.

Substituting Eqs. (3.7) and 3.9 into Eq. (3.8), the maximum achievable magnetostrictive strain in the Terfenol-D fibers, with the combined effect of the thermal-induced residual compressive stresses and the applied H field, becomes

$$\lambda_S(\sigma_T) = \lambda_S + \frac{\lambda_S}{2} \cdot \tanh\left(\frac{2 \cdot -E^{Epoxy} \cdot (\alpha^{Epoxy} - \alpha^{T-D}) \cdot \Delta T \cdot \frac{(1 - \nu_f)}{\nu_f}}{\sigma_{TS}}\right). \quad (3.10)$$

Recalling that λ_S of the classical composite formulation for the upper bound is

$$\lambda_S(\nu_f) = \lambda_S \cdot \left[\frac{E^{T-D} \cdot \nu_f}{E^{T-D} \cdot \nu_f + E^{Epoxy} \cdot (1 - \nu_f)} \right], \quad (3.11)$$

where E^{T-D} is the Young's modulus of the Terfenol-D fibers. Replacing λ_S in Eq. (3.11) by $\lambda_S(\sigma_T)$ in Eq. (3.10), the thermal stress-mediated continuous-fiber composite model for saturation magnetistive strain is

$$\lambda_S(\nu_f) = \left[\lambda_S + \frac{\lambda_S}{2} \cdot \tanh\left(\frac{2 \cdot -E^{Epoxy} \cdot (\alpha^{Epoxy} - \alpha^{T-D}) \cdot \Delta T \cdot \frac{(1 - \nu_f)}{\nu_f}}{\sigma_{TS}}\right) \right] \cdot \left[\frac{E^{T-D} \cdot \nu_f}{E^{T-D} \cdot \nu_f + E^{Epoxy} \cdot (1 - \nu_f)} \right]. \quad (3.12)$$



3.3.2 Application to Experimental Results

Figure 3.19 shows the comparison between the experimental λ_s obtained previously in Fig. 3.8 and the modeled λ_s based on Eq. (3.12) with the parameters summarized in Table 3.1. It is clear that the thermal stress-mediated continuous-fiber composite model is capable of predicting λ_s in the continuous-fiber composites at different post-curing temperatures (T_{PC}) and ν_f . For $T_{PC} = 30$ °C, the thermal stress-mediated continuous-fiber composite model reduces to the classical composite formulation for the upper bound. The effect of thermal-induced residual compressive stress is more pronounced for composites with low ν_f (< 0.3) as illustrated in Fig. 3.20 based on Eq. (3.7). This is mainly attributed to the increased epoxy contribution to the loading of the embedded Terfenol-D fibers.

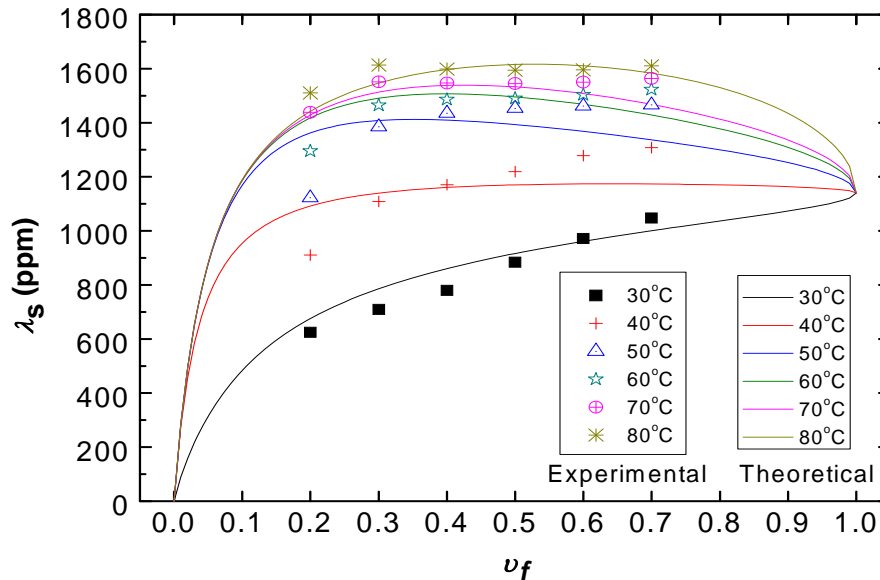


Fig. 3.19 Comparison between the experimental λ_s obtained in Fig. 3.8 and the modeled λ_s based on Eq. (3.12) with the parameters summarized in Table 3.1.



Table 3.1 Analytical model parameters.

Saturation magnetostrictive strain (ppm)	λ_s	1140
Optimal thermal compressive stress (MPa)	σ_{TS}	-20
Coefficient of thermal expansion for the epoxy matrix ($^{\circ}\text{C}$)	$\alpha^{Epoxy}(T)$	60×10^{-6}
Coefficient of thermal expansion for the Terfenol-D fiber ($^{\circ}\text{C}$)	$\alpha^{T-D}(T)$	8×10^{-6}
Young's modulus of the Terfenol-D fiber (GPa)	E^{T-D}	35
Young's modulus of the epoxy matrix (GPa)	E^{Epoxy}	2.6

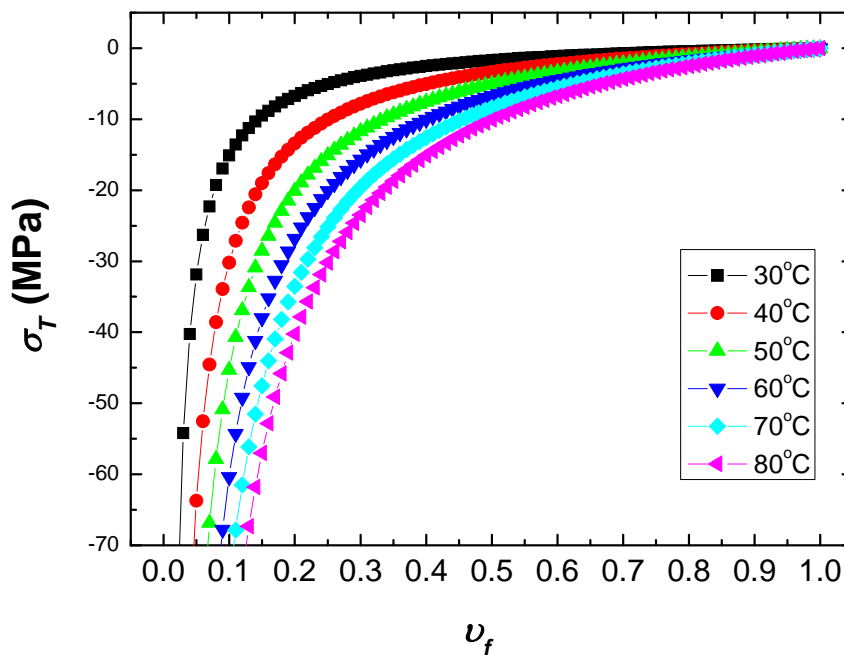


Fig. 3.20 Thermal-induced residual compressive stress (σ_T) as a function of volume fraction of Terfenol-D fibers (ν_f).



Chapter 4

Dynamic Material Properties of Continuous-Fiber Composites

4.1 Introduction

In the previous chapter, the quasistatic magnetic and magnetostrictive properties of the continuous-fiber composites have been measured. The 1608 ppm unloaded λ_S in the post-cured continuous-fiber composites at 80 °C represents the greatest value in the magnetostrictive community, being 44, 56, and 144% larger than the monolithic Terfenol-D, short-fiber composites, and particulate-chain composites, respectively. The investigation into the domain magnetization and magnetostriction processes of all material samples has revealed the physical origin of the non-180° domain wall motion in general and the 90° domain wall motion in particular. The higher fiber aspect ratio for greater stress transfer from the continuous fibers to the matrix and the texturing of the continuous fibers along the highly magnetostrictive [112] crystallographic axis are both beneficial to the practical realization of the giant unloaded λ_S as well. The thermal-stress-mediated continuous-fiber composite model has confirmed the “preset” of the maximum number of non-180° (or 90°) domain state in the continuous-fiber composites via the optimal development of residual compressive stresses in the embedded continuous fibers during the composite post-curing process.



In this chapter, the dynamic magnetic and magnetostrictive properties of the post-cured continuous-fiber composites (at 80 °C) are evaluated as functions of frequency, magnetic bias field, and Terfenol-D volume fraction under a sinusoidal magnetic drive field of 1 kA/m peak amplitude. The measured frequency dependent data, bias field dependant data, and volume fraction dependant data are discussed and compared with those of the monolithic Terfenol-D, short-fiber composites, and particulate-chain composites.

4.2 Dynamic Measurements

The in-house automated measurement system employed to evaluate the quasistatic magnetic and magnetostrictive properties of our magnetostrictive material samples in the last chapter (Figs. 3.1 and 3.2) was configured to measure the samples' dynamic magnetic and magnetostrictive properties. The schematic diagram of the dynamic measurement system is shown in Fig. 4.1. Similar to the quasistatic measurement system, the dynamic configuration can generally be identified as two basic parts: (1) the magnetic field generation part and (2) the signal detection conditioning unit. To generate magnetic fields, a dynamic signal analyzer (Ono Sokki CF5220), a water-cooled, U-shaped electromagnet (Myitem PEM-8005K), a dc power supply (Sorensen DHP200-15), a constant-current-supply amplifier (AE Techron 7572), and a pair of Helmholtz coils were used. To detect and condition the induced signals, a Hall probe (PAA71-1908-05), a dc Gaussmeter (F. W. Bell 7030), a laser vibrometer (Graphtec Demodulator AT3700), an integrating fluxmeter (Walker LDJ MF-10), a pick-up coil, and a search coil were utilized.

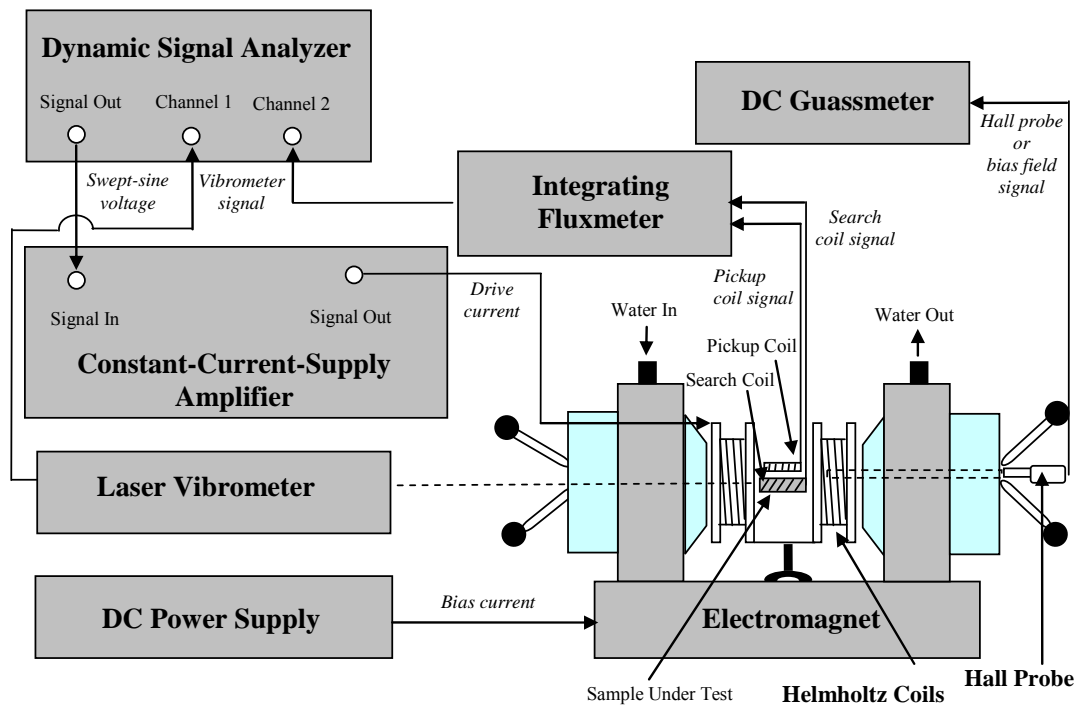


Fig. 4.1 Schematic diagram of the in-house automation dynamic measurement system.

Referring to Fig. 4.1, the dynamic magnetic and magnetostrictive properties of the samples in the longitudinal direction were measured at room temperature and with zero stress loading by sweeping a sinusoidal magnetic drive field (H_3) of 1 kA/m over a prescribed frequency range (f) of 1 – 100 kHz at a rate of 26 step/s and then measuring the corresponding magnetic induction (B_3) and dynamic strain (S_3) at discrete frequency intervals of 25 Hz/step under various magnetic bias fields (H_{Bias}) of 10 – 200 kA/m. H_3 was provided by the Helmholtz coils driven by the dynamic signal analyzer via the constant-current-supply amplifier. H_{Bias} was supplied by electromagnet controlled by the dc power supply. H_3 and H_{Bias} were monitored in-situ by the pick-up coil connected to the integrating fluxmeter and the Hall probe connected to the dc Gaussmeter, respectively. B_3 was measured using the search coil



wrapped around the sample and linked to the integrating fluxmeter. S_3 was obtained by the laser vibrometer, respectively. All quantities were sampled and recorded by the dynamic signal analyzer and stored in a computer. The dynamic relative permeability (μ_{r33}) was determined from

$$\mu_{r33} = \frac{B_3}{\mu_o H_3}, \quad (4.1)$$

where $\mu_o = 4 \pi \times 10^{-7}$ H/m is the permeability of free space. The elastic moduli at constant magnetic field strength (E_3^H) and at constant magnetic induction (E_3^B) were evaluated from the resonance frequency (f_r) and anti-resonance frequency (f_a) as observed from the μ_{r33} spectrum by

$$E_3^H = 4\rho(Lf_r)^2, \quad (4.2)$$

$$E_3^B = 4\rho(Lf_a)^2, \quad (4.3)$$

where L and ρ are the length and density of the samples, respectively. The dynamic strain coefficient (d_{33}) was obtained from

$$d_{33} = \frac{S_3}{H_3}. \quad (4.4)$$

The magnetomechanical coupling coefficient (k_{33}) was calculated using

$$k_{33} = \sqrt{1 - \left(\frac{f_r}{f_a}\right)^2} = \sqrt{1 - \left(\frac{E_3^H}{E_3^B}\right)^2}. \quad (4.5)$$



4.3 Results and Discussions

4.3.1 Frequency Dependent Data

The dependence of μ_{r33} on f at various H_{Bias} for the continuous-fiber composites ($\nu_f = 0.2 - 0.7$) is shown in Fig. 4.2, together with that for the monolithic Terfenol-D, short-fiber composite ($\nu_f = 0.5$), and particulate-chain composite ($\nu_f = 0.5$). The fundamental longitudinal mode resonances of the continuous-fiber composites are approximately 20 kHz, and the two weaker resonances at about 55 and 85 kHz are the second and third harmonics, respectively [Fig. 4.2(a)–(f)]. These harmonics are obvious only when ν_f is sufficiently large (i.e., $\nu_f \geq 0.4$) so that the magnetomechanical coupling is strong enough. [Fig. 4.2(c)–(f)]. Apart from these resonances, the frequency responses for μ_{r33} are essentially flat over the measured frequency range except for the variations associated with resonances. By contrast, significant eddy-current losses are observed for the monolithic Terfenol-D as its μ_{r33} values decrease dramatically with increasing f [Fig. 4.2(g)]. Similar to the continuous-fiber composites, the effect of eddy-current losses is also insignificant in the short-fiber and particulate-chain composites [Fig. 4.2(h)–(i)].

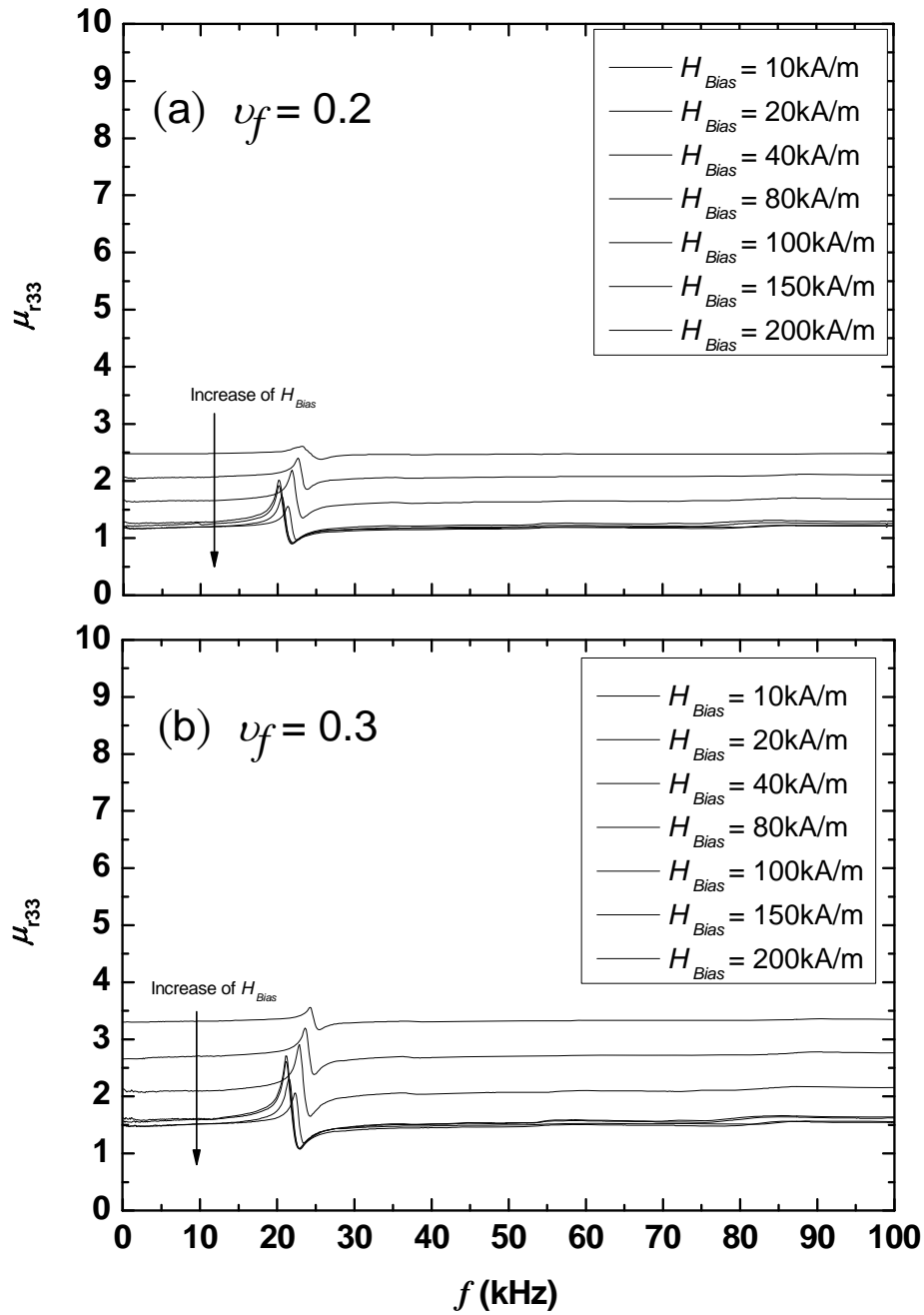


Fig. 4.2 μ_{r33} versus f at different H_{Bias} for continuous-fiber composites with (a) $\nu_f = 0.2$, (b) $\nu_f = 0.3$, (c) $\nu_f = 0.4$, (d) $\nu_f = 0.5$, (e) $\nu_f = 0.6$, and (f) $\nu_f = 0.7$, together with (g) monolithic Terfenol-D, (h) short-fiber composite ($\nu_f = 0.5$), and (i) particulate-chain composite ($\nu_f = 0.5$). [To be continued]

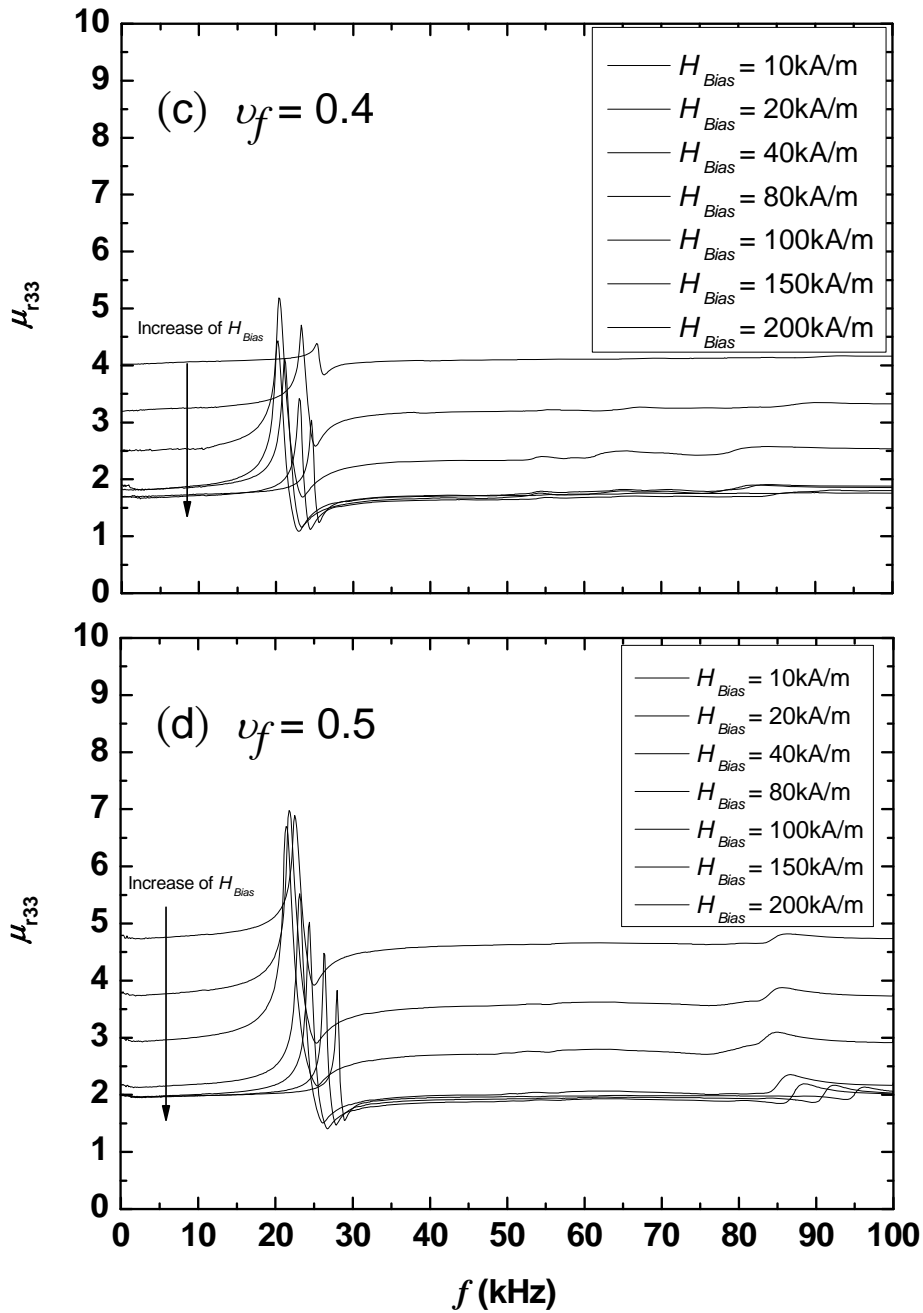


Fig. 4.2 μ_{r33} versus f at different H_{Bias} for continuous-fiber composites with (a) $v_f = 0.2$, (b) $v_f = 0.3$, (c) $v_f = 0.4$, (d) $v_f = 0.5$, (e) $v_f = 0.6$, and (f) $v_f = 0.7$, together with (g) monolithic Terfenol-D, (h) short-fiber composite ($v_f = 0.5$), and (i) particulate-chain composite ($v_f = 0.5$). [To be continued]

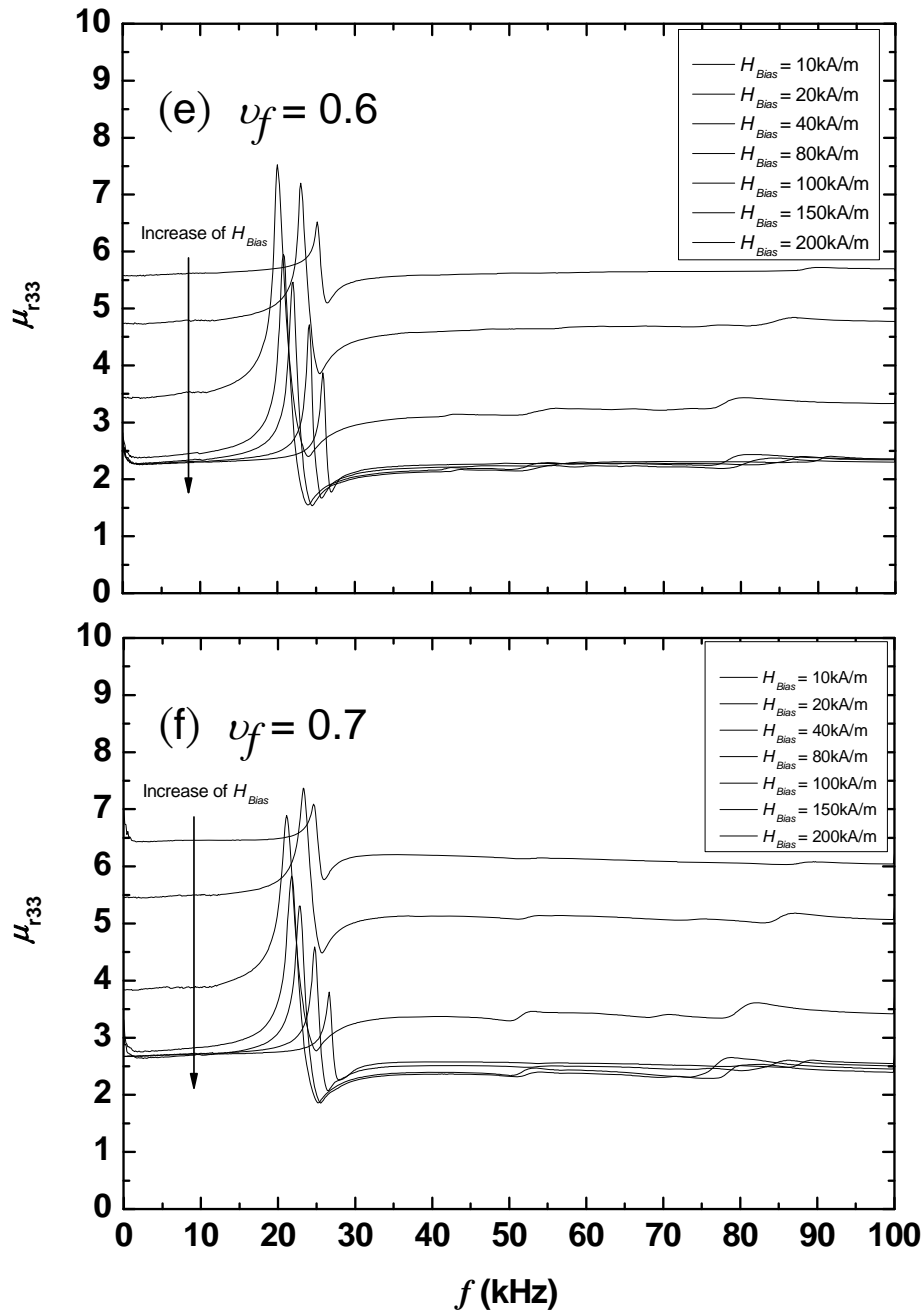


Fig. 4.2 μ_{r33} versus f at different H_{Bias} for continuous-fiber composites with (a) $\nu_f = 0.2$, (b) $\nu_f = 0.3$, (c) $\nu_f = 0.4$, (d) $\nu_f = 0.5$, (e) $\nu_f = 0.6$, and (f) $\nu_f = 0.7$, together with (g) monolithic Terfenol-D, (h) short-fiber composite ($\nu_f = 0.5$), and (i) particulate-chain composite ($\nu_f = 0.5$). [To be continued]

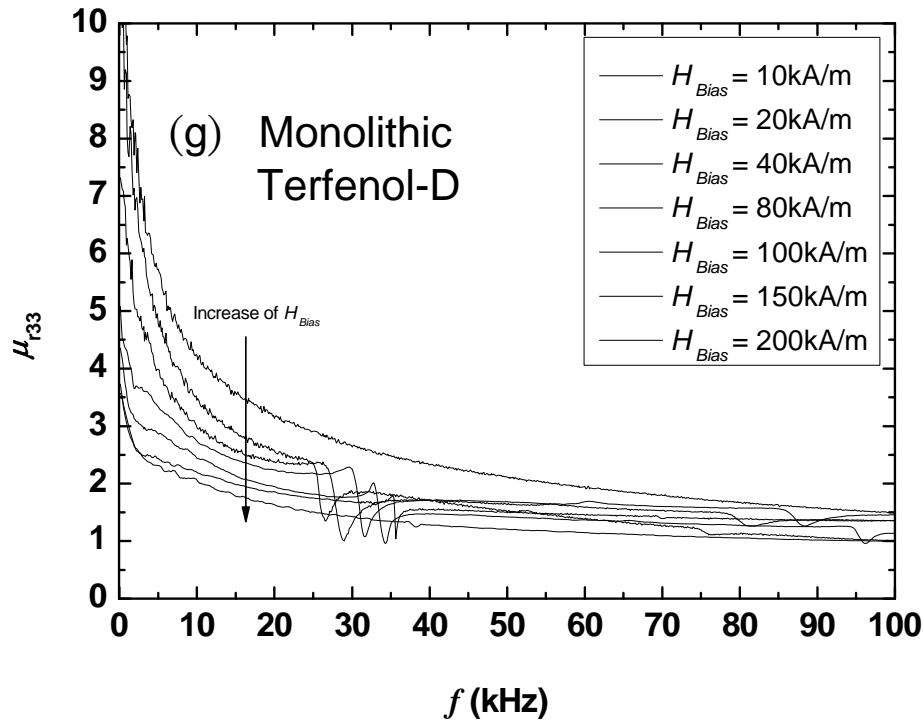


Fig. 4.2 μ_{r33} versus f at different H_{Bias} for continuous-fiber composites with (a) $\nu_f = 0.2$, (b) $\nu_f = 0.3$, (c) $\nu_f = 0.4$, (d) $\nu_f = 0.5$, (e) $\nu_f = 0.6$, and (f) $\nu_f = 0.7$, together with (g) monolithic Terfenol-D, (h) short-fiber composite ($\nu_f = 0.5$), and (i) particulate-chain composite ($\nu_f = 0.5$). [To be continued]

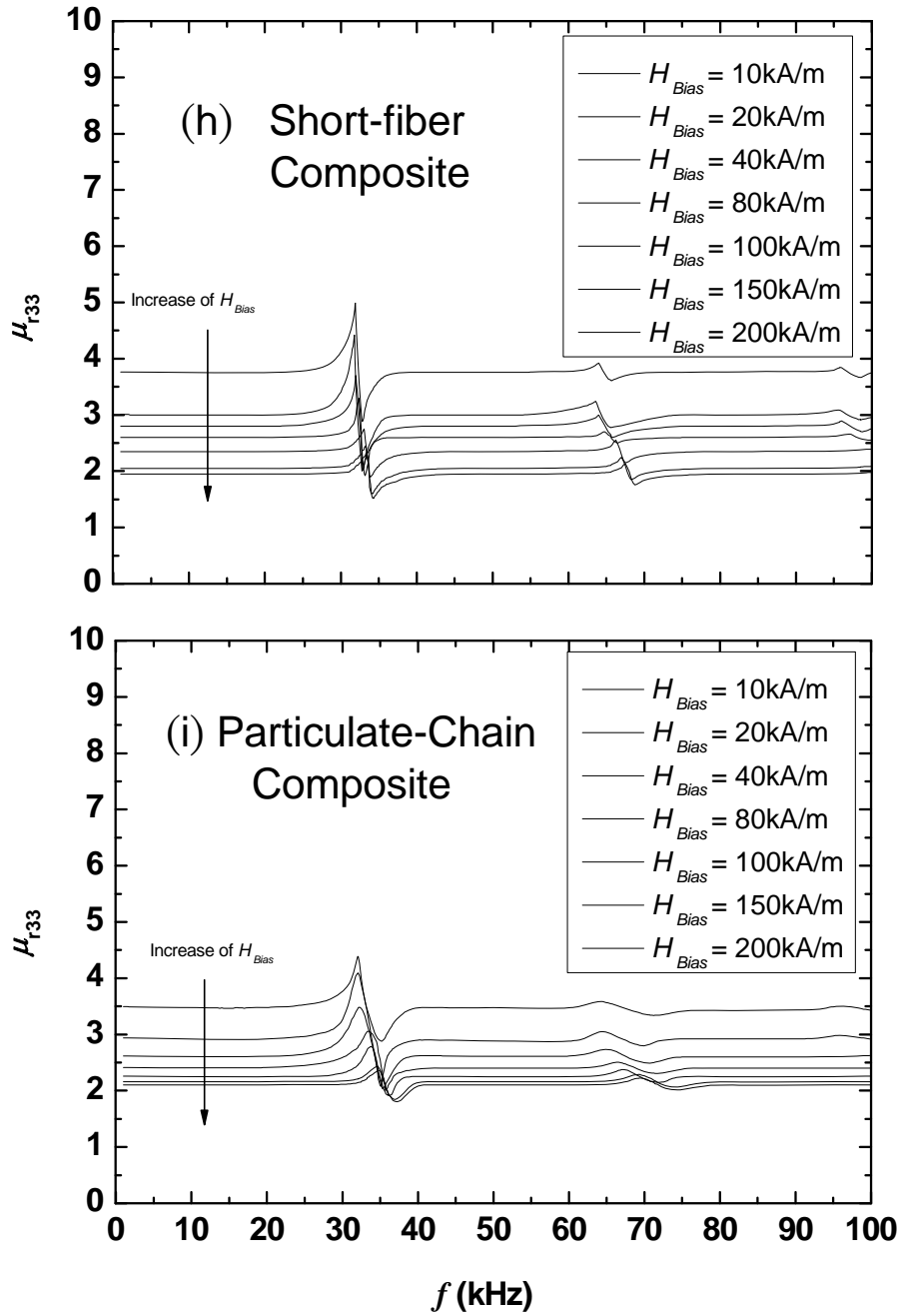


Fig. 4.2 μ_{r33} versus f at different H_{Bias} for continuous-fiber composites with (a) $\nu_f = 0.2$, (b) $\nu_f = 0.3$, (c) $\nu_f = 0.4$, (d) $\nu_f = 0.5$, (e) $\nu_f = 0.6$, and (f) $\nu_f = 0.7$, together with (g) monolithic Terfenol-D, (h) short-fiber composite ($\nu_f = 0.5$), and (i) particulate-chain composite ($\nu_f = 0.5$).



The dependence of d_{33} on f at various H_{Bias} for the continuous-fiber composites ($\nu_f = 0.2 - 0.7$), monolithic Terfenol-D, short-fiber composite ($\nu_f = 0.5$), and particulate-chain composite ($\nu_f = 0.5$) are shown in Fig. 4.3. Again, the fundamental longitudinal mode resonances of the continuous-fiber composites are found to be about 20 kHz, and the two weaker resonances at about 55 and 85 kHz are their second and third harmonics, respectively [Fig. 4.3(a)–(f)]. The observations are consistent with those of the μ_{r33} spectra reported in Fig. 4.2. Besides these resonances, the frequency responses for d_{33} are also flat over the frequency range of measurement except for the variations associated with resonances. Because of the significant eddy-current losses in the monolithic Terfenol-D as seen in the μ_{r33} spectrum [Fig. 4.2(g)], the d_{33} spectra also shows a decreasing trends with increasing f [Fig. 4.3(g)]. However, the short-fiber and particulate-chain composites are not susceptible to the eddy-current effect as reflected by their stable d_{33} spectra throughout the whole frequency range of interest, excluding the resonance regions.

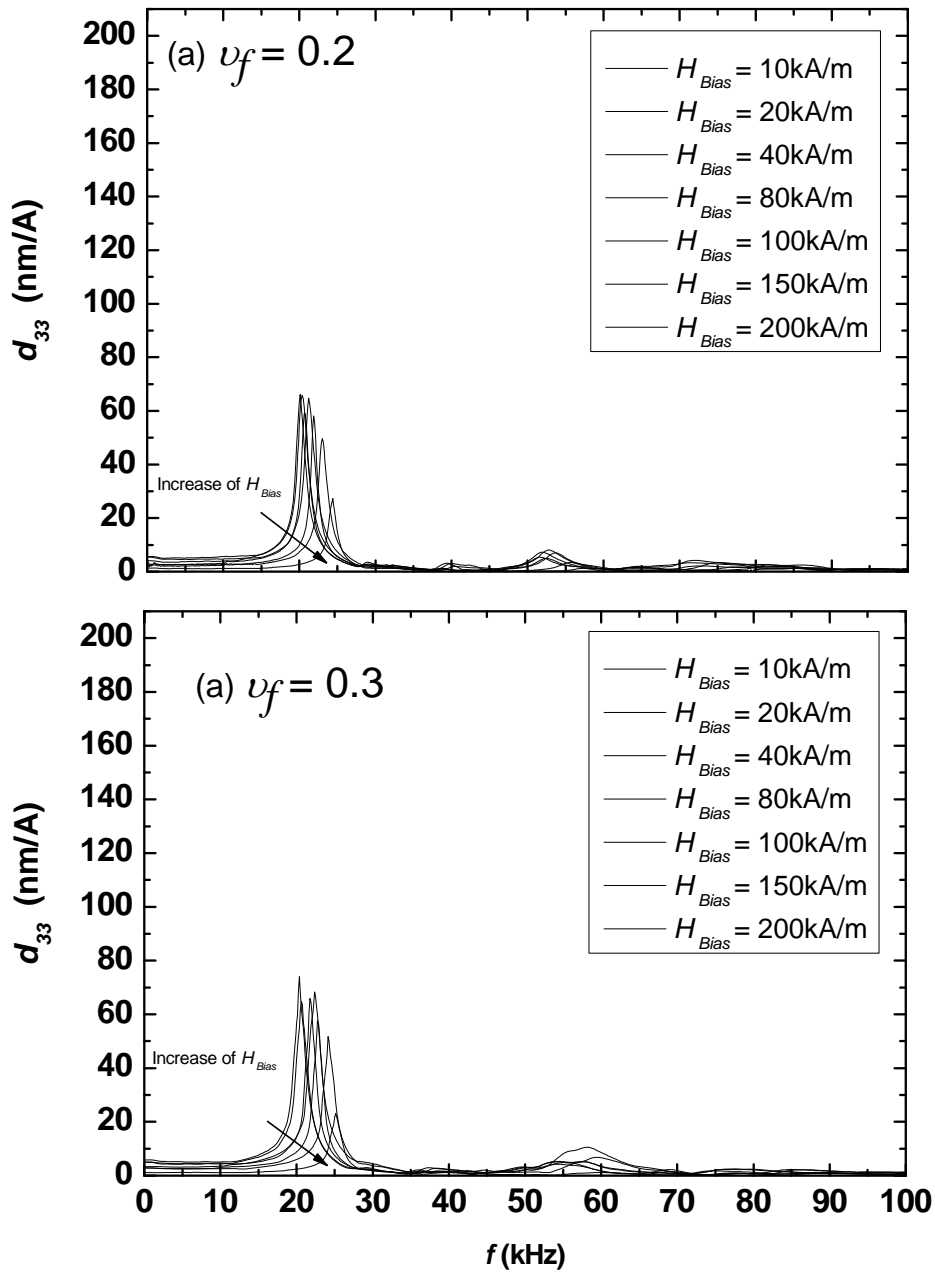


Fig. 4.3 d_{33} versus f at different H_{Bias} for continuous-fiber composites with (a) $\nu_f = 0.2$, (b) $\nu_f = 0.3$, (c) $\nu_f = 0.4$, (d) $\nu_f = 0.5$, (e) $\nu_f = 0.6$, and (f) $\nu_f = 0.7$, together with (g) monolithic Terfenol-D, (h) short-fiber composite ($\nu_f = 0.5$), and (i) particulate-chain composite ($\nu_f = 0.5$). [To be continued]

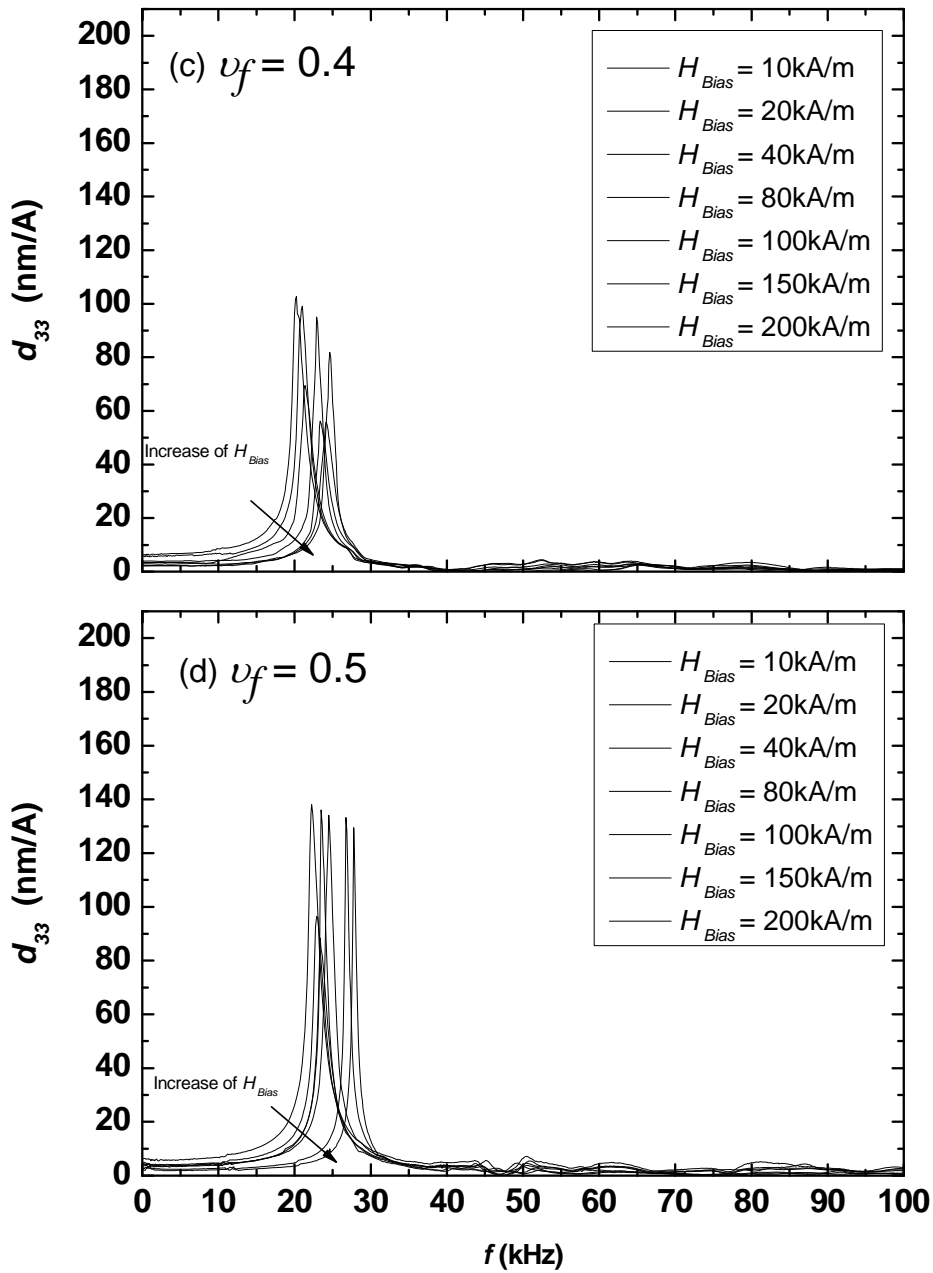


Fig. 4.3 d_{33} versus f at different H_{Bias} for continuous-fiber composites with (a) $\nu_f = 0.2$, (b) $\nu_f = 0.3$, (c) $\nu_f = 0.4$, (d) $\nu_f = 0.5$, (e) $\nu_f = 0.6$, and (f) $\nu_f = 0.7$, together with (g) monolithic Terfenol-D, (h) short-fiber composite ($\nu_f = 0.5$), and (i) particulate-chain composite ($\nu_f = 0.5$). [To be continued]

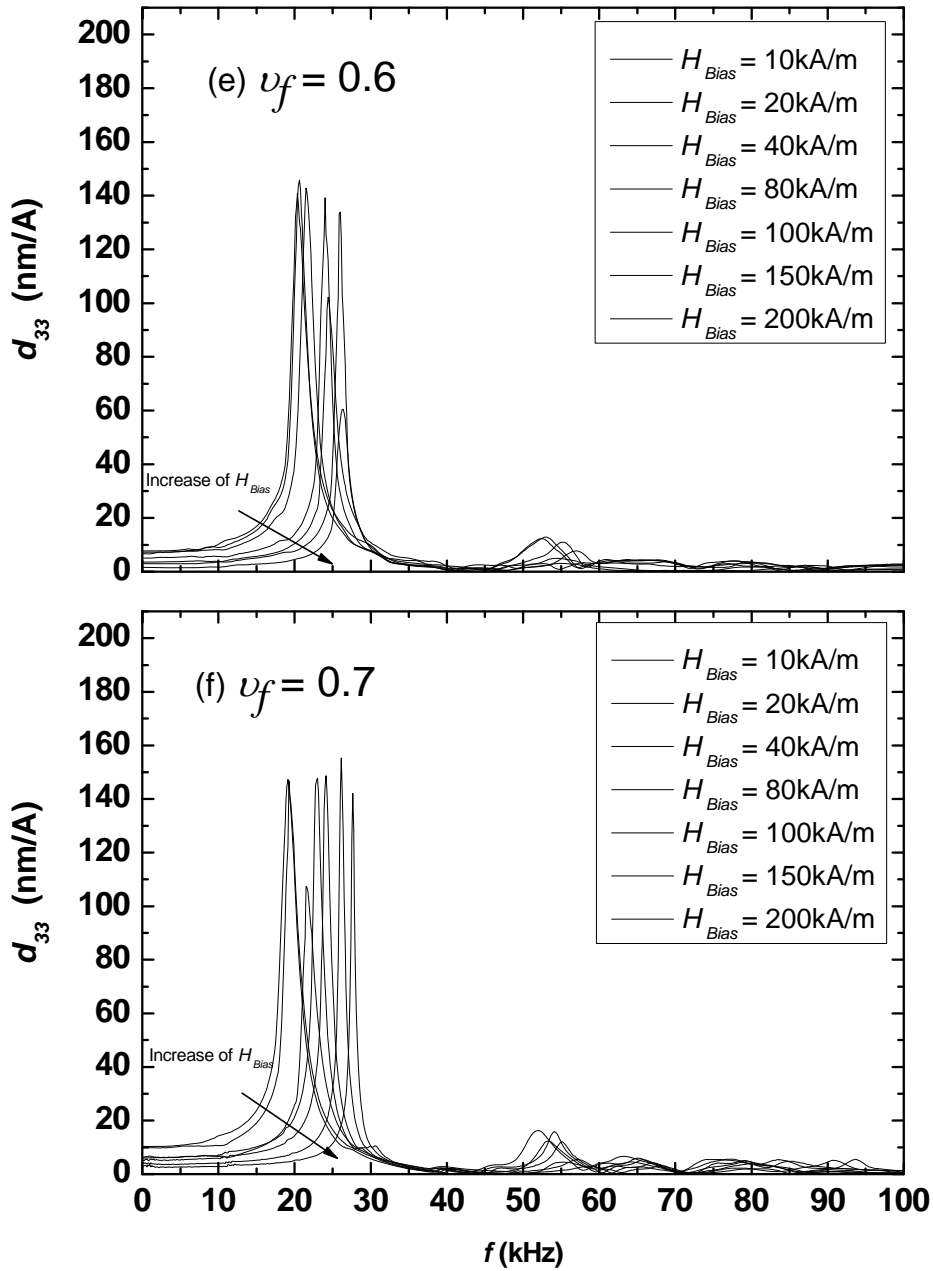


Fig. 4.3 d_{33} versus f at different H_{Bias} for continuous-fiber composites with (a) $\nu_f = 0.2$, (b) $\nu_f = 0.3$, (c) $\nu_f = 0.4$, (d) $\nu_f = 0.5$, (e) $\nu_f = 0.6$, and (f) $\nu_f = 0.7$, together with (g) monolithic Terfenol-D, (h) short-fiber composite ($\nu_f = 0.5$), and (i) particulate-chain composite ($\nu_f = 0.5$). [To be continued]

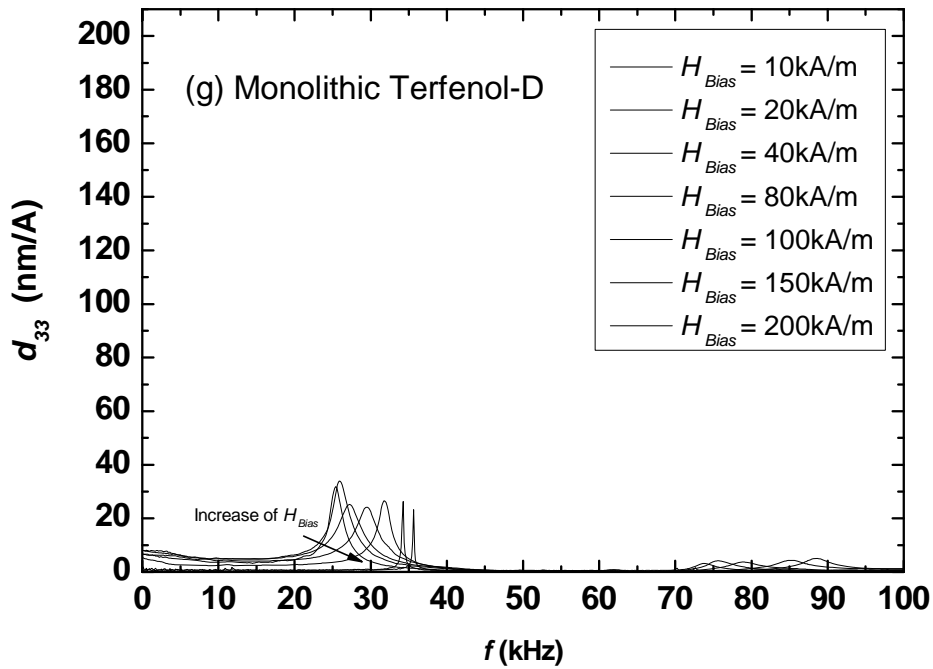


Fig. 4.3 d_{33} versus f at different H_{Bias} for continuous-fiber composites with (a) $\nu_f = 0.2$, (b) $\nu_f = 0.3$, (c) $\nu_f = 0.4$, (d) $\nu_f = 0.5$, (e) $\nu_f = 0.6$, and (f) $\nu_f = 0.7$, together with (g) monolithic Terfenol-D, (h) short-fiber composite ($\nu_f = 0.5$), and (i) particulate-chain composite ($\nu_f = 0.5$). [To be continued]

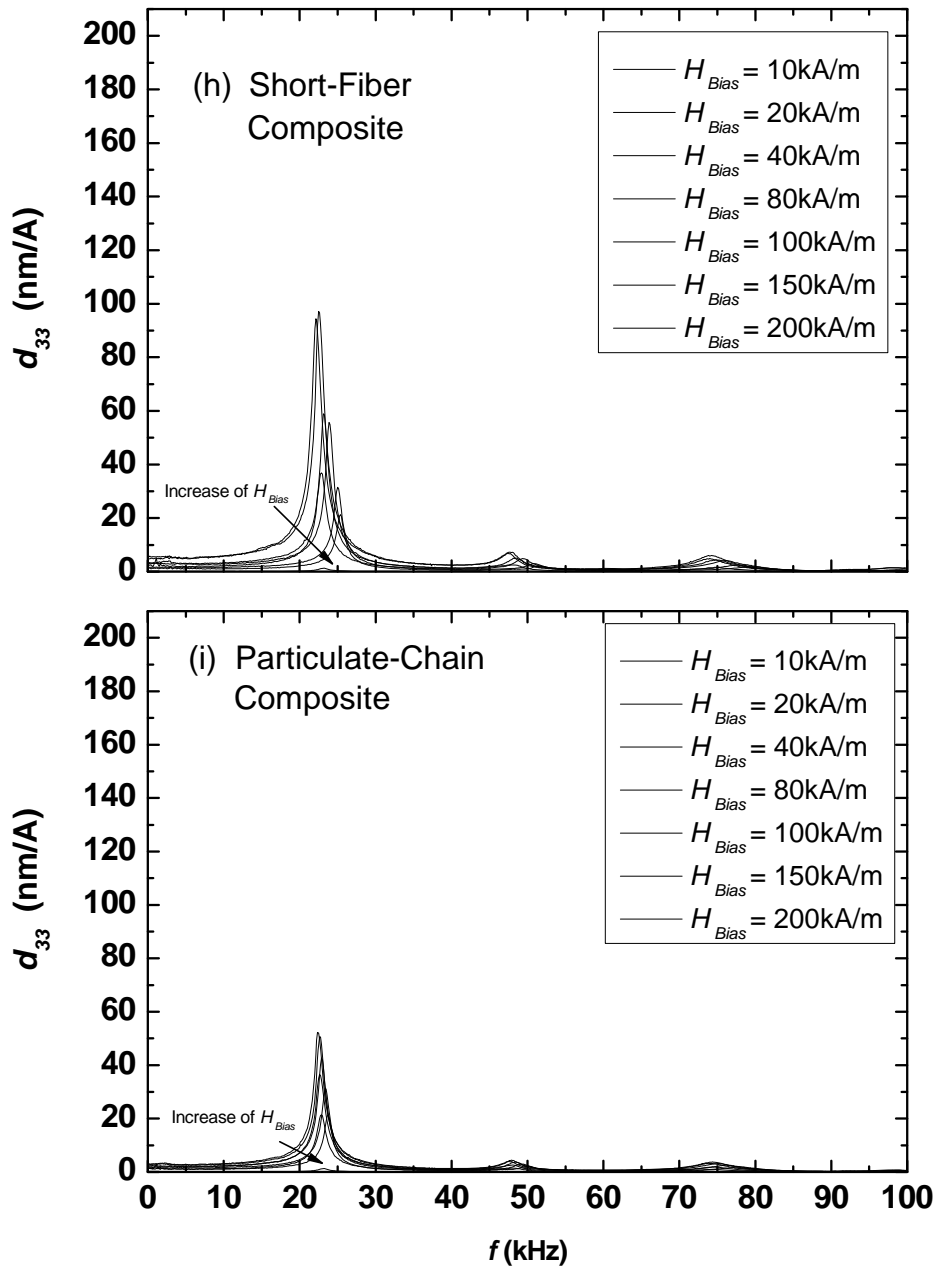


Fig. 4.3 d_{33} versus f at different H_{Bias} for continuous-fiber composites with (a) $\nu_f = 0.2$, (b) $\nu_f = 0.3$, (c) $\nu_f = 0.4$, (d) $\nu_f = 0.5$, (e) $\nu_f = 0.6$, and (f) $\nu_f = 0.7$, together with (g) monolithic Terfenol-D, (h) short-fiber composite ($\nu_f = 0.5$), and (i) particulate-chain composite ($\nu_f = 0.5$).



4.3.2 Bias Field Dependant Data

μ_{r33} as a function of H_{Bias} for all samples at various ν_f is shown in Fig. 4.4.

These data correspond to the 1 kHz values of the μ_{r33} spectra in Fig. 4.2. The μ_{r33} values of the continuous-fiber composites attain their maximum values at $H_{Bias} = 5$ kA/m and then decrease significantly in the H_{Bias} range of 5 – 40 kA/m before leveling off for $H_{Bias} > 40$ kA/m. Since the Terfenol-D continuous fibers have a cubic Laves phase, and their spontaneous magnetizations are essentially parallel to the $\langle 111 \rangle$ easy axis, there exists a considerable amount of magnetic domains and domain walls in the continuous fibers. During the composite fabrication, thermal-induced residual compressive stresses were developed axially in the continuous-fiber composites while the epoxy matrix was post-cured. These built-in residual compressive stresses effectively create a preferred non-180° domain state in the continuous-fiber composites as in the case of applying an external stress loading to assert an initial non-180° domain state in monolithic Terfenol-D. Thus, the initial maximum in μ_{r33} at $H_{Bias} = 5$ kA/m is mainly attributed to the relatively easy 180° domain-wall motion. As H_{Bias} is increased beyond this level, the reduced 180° domain-wall motion competes with the increased non-180° domain-wall motion, resulting in a decrease in μ_{r33} . For $H_{Bias} > 40$ kA/m, the contribution to μ_{r33} from the motion of 180° domain walls is negligible. This effect, together with the constraint of non-180° domain-wall motion under H_{Bias} , tends to level off μ_{r33} . The monolithic Terfenol-D has the largest μ_{r33} compared to all types of composites due to the existence of the highest $\nu_f (= 1)$. Similarly, continuous-fiber composites with



higher ν_f show larger μ_{r33} in general. However, the short-fiber ($\nu_f = 0.5$) and particulate-chain ($\nu_f = 0.5$) composites exhibit slightly lower μ_{r33} values than the continuous-fiber composite ($\nu_f = 0.5$) for relatively low H_{Bias} levels of < 80 kA/m because of the lower length-to-width fiber and particle aspect ratios of 4:1 and 1:1, respectively compared to the 45:1 for the continuous fibers. A reduction in fiber (or particle) aspect ratio tends to increase demagnetizing fields which, in turn, require larger magnetic energy to magnetize the material.

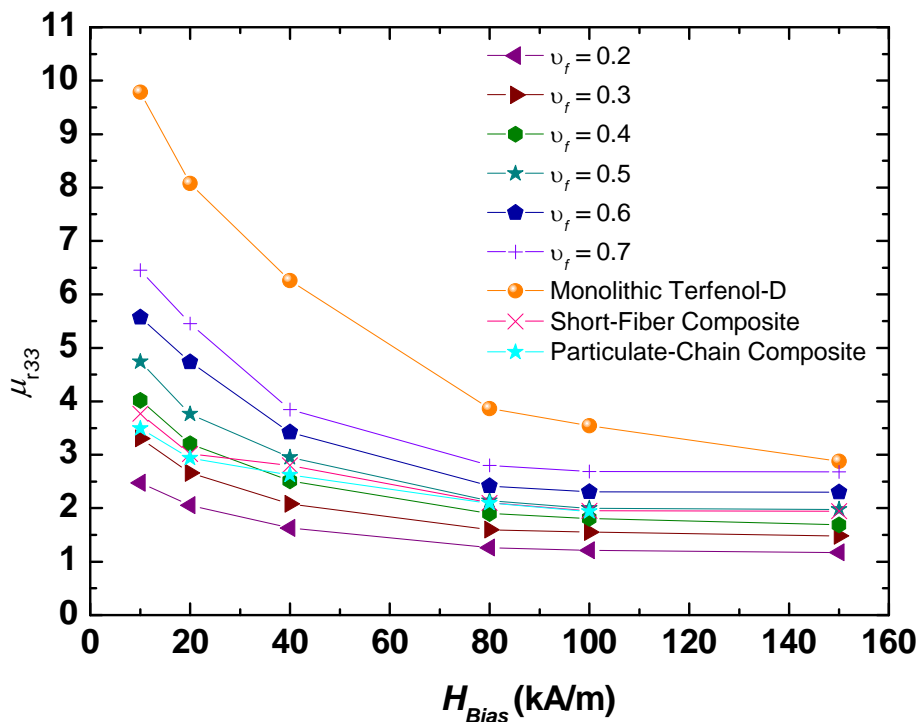


Fig. 4.4 μ_{r33} measured at 1 kHz as a function of H_{Bias} for continuous-fiber composites ($\nu_f = 0.2 - 0.7$), monolithic Terfenol-D, short-fiber composite ($\nu_f = 0.5$), and particulate-chain composite ($\nu_f = 0.5$).



Figure 4.5 shows the dependence of E_3^H and E_3^B on H_{Bias} for all samples at various ν_f . The values of E_3^H and E_3^B were calculated from the resonance frequency (f_r) and anti-resonance frequency (f_a) values of the μ_{r33} spectra in Fig. 4.2 using Eq. (4.2) and Eq. (4.3), respectively. All samples show an initial drop in E_3^H with increasing H_{Bias} . This is due to the H_{Bias} -induced motion of the available non-180° domain walls. As H_{Bias} is increased to near 40 kA/m, the compliance associated with increased deformation contribution from this non-180° domain wall motion is maximized, leading to a minimum in E_3^H . Beyond this H_{Bias} level, E_3^H as a function of H_{Bias} displays an increasing trend. The effect is ascribed to the constraint of non-180° domain-wall motion due to interaction with H_{Bias} . The monolithic Terfenol-D shows the greatest E_3^H owing to its unity ν_f . The short-fiber ($\nu_f = 0.5$) and particulate-chain ($\nu_f = 0.5$) composites, both with E_3^H and E_3^B slightly lower than the continuous-fiber composite ($\nu_f = 0.5$), are mainly attributed to lower fiber (or particle) aspect ratios with lower efficiencies in terms of stress transfer from the fibers (or particles) to the epoxy matrix. Nevertheless, all composites demonstrate the ΔE effect similar to the case in an externally loaded monolithic Terfenol-D.

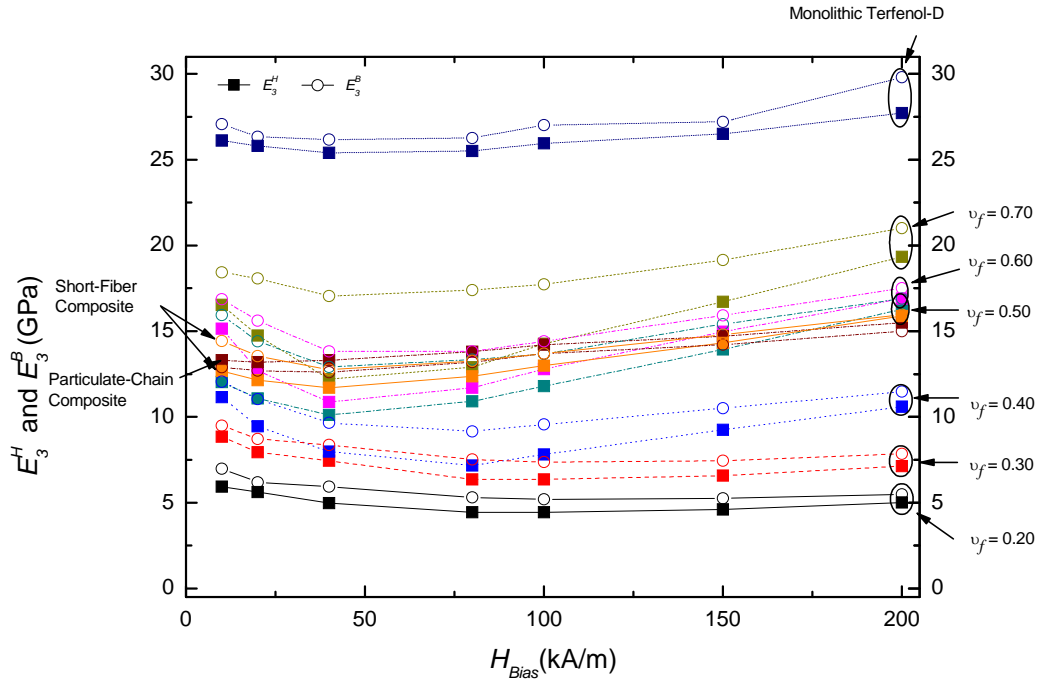


Fig. 4.5 Dependence of E_3^H and E_3^B on H_{Bias} for continuous-fiber composites ($\nu_f = 0.2 - 0.7$), monolithic Terfenol-D, short-fiber composite ($\nu_f = 0.5$), and particulate-chain composite ($\nu_f = 0.5$).

Figure 4.6 plots the d_{33} values extracted from Fig. 4.3 at 1 kHz as a function of H_{Bias} for all samples. It is clear that the d_{33} curves for all samples increase initially and display maximum values near $H_{Bias} = 40$ kA/m. This is a result of increasing and maximizing S_3 contribution from the non-180° domain-wall motion, respectively. In particular, the occurrence of maximum d_{33} at about 40 kA/m suggests that all samples are basically biased in the center of the “burst region” of their quasistatic $\lambda-H_3^{QS}$ curves (Fig. 3.4). The results agree with the initial decrease in both μ_{r33} and E_3^H for $H_{Bias} < 40$ kA/m (Figs. 4.4 and 4.5). Importantly, continuous-fiber composites with increased ν_f of ≥ 0.6 possess the greatest d_{33} values. The results are in good agreement with the quasistatic d_{33}^{QS} responses shown in Figs. 3.9 and 3.10.



Such good agreement also implies the predominant effects of the thermal-induced residual compressive stresses in the continuous fibers, a higher fiber aspect ratio for greater stress transfer from the continuous fibers to the matrix, and the texturing of the continuous fibers along the highly magnetostrictive [112] crystallographic axis to the monolithic Terfenol-D, short-fiber composite, and particulate-chain composite, respectively.

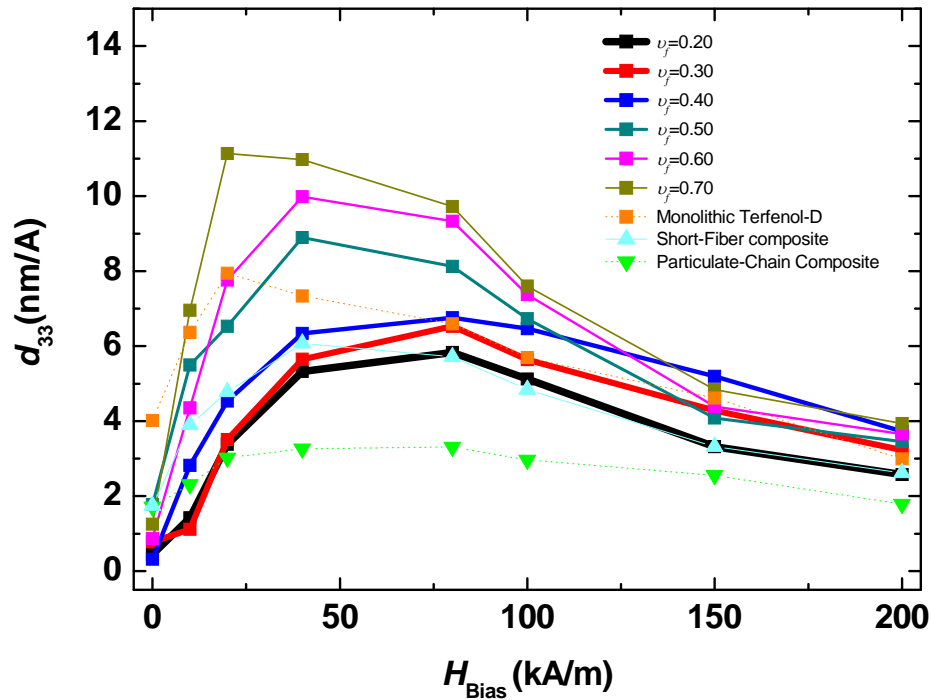


Fig. 4.6 d_{33} measured at 1 kHz as a function of H_{Bias} for continuous-fiber composites ($v_f = 0.2 - 0.7$), monolithic Terfenol-D, short-fiber composite ($v_f = 0.5$), and particulate-chain composite ($v_f = 0.5$).

Figure 4.7 shows k_{33} as a function of H_{Bias} for all samples at various v_f . The k_{33} values were determined from the resonance frequency (f_r) and anti-resonance frequency (f_a) values of the μ_{r33} spectra in Fig. 4.2 using Eq. (4.5). In fact, k_{33} is a



measure of the fraction of magnetic energy that can be converted into mechanical energy per cycle and vice versa. The increase in k_{33} for $H_{Bias} < 40$ kA/m indicates an increase in energy transduction. This is associated with the increased S_3 output as H_{Bias} increases. A maximum in k_{33} occurred also near 40 kA/m suggests the maximum energy conversion between the elastic and magnetic states of the materials. A decrease in k_{33} for $H_{Bias} > 40$ kA/m reflects the saturation of S_3 by H_{Bias} . The continuous-fiber composites with ν_f of ≥ 0.4 demonstrate comparable k_{33} - H_{Bias} responses to the monolithic Terfenol-D. The short-fiber composite ($\nu_f = 0.5$) only has the k_{33} - H_{Bias} response close to the continuous-fiber composite with $\nu_f = 0.3$, while the particulate-chain composite ($\nu_f = 0.5$) is even fall short of the k_{33} - H_{Bias} response of the continuous-fiber composite with $\nu_f = 0.2$. The reasons are the same as those for the enhancement in the d_{33} - H_{Bias} responses in Fig. 4.6. In other words, it can be described by the increased magnetomechanical coupling as a result of the increased mechanical activities in the continuous-fiber composites.

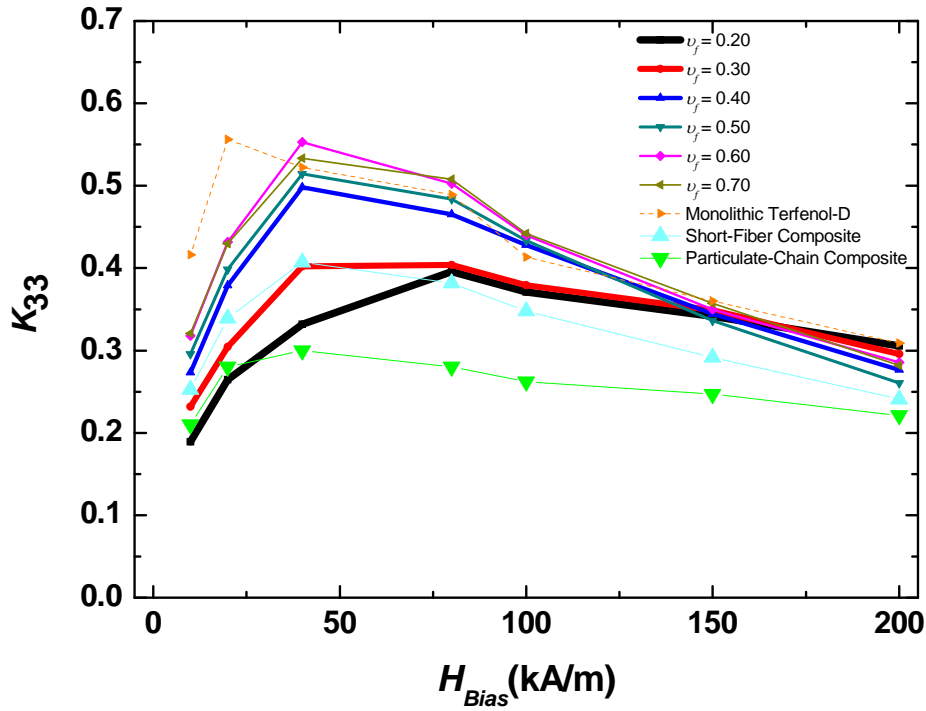


Fig. 4.7 k_{33} measured at 1 kHz as a function of H_{Bias} for continuous-fiber composites ($\nu_f = 0.2 - 0.7$), monolithic Terfenol-D, short-fiber composite ($\nu_f = 0.5$), and particulate-chain composite ($\nu_f = 0.5$).

4.3.3 Volume Fraction Dependant Data

Figure 4.8 displays the ν_f dependence of μ_{r33} at $H_{Bias} = 40$ kA/m for all samples. The prediction of μ_{r33} based on the rule of mixture formulation as expressed in Eq. (4.6) is also plotted on the same figure for comparison.

$$\mu_{r33} = \nu_f \mu_{r33}^{T-D} + (1 - \nu_f) \mu_{r33}^{Epoxy} . \quad (4.6)$$

It is clear that the μ_{r33} values associated with the continuous-fiber composites not only show a nearly linear function of ν_f but also coincides well with the prediction. This good agreement is also extended to both the short-fiber ($\nu_f = 0.5$) and particulate-chain ($\nu_f = 0.5$) composites even though the effect of fiber (or particle)



aspect ratio and hence the effect of demagnetizing fields also exert certain degrees of influence on μ_{r33} as described in Fig. 4.4. Hence it is concluded that the magnetic properties of the epoxy-bonded Terfenol-D composites are mainly dependent on the Terfenol-D volume fraction ν_f followed by the fiber (or particle) aspect ratio or the resulting demagnetizing fields.

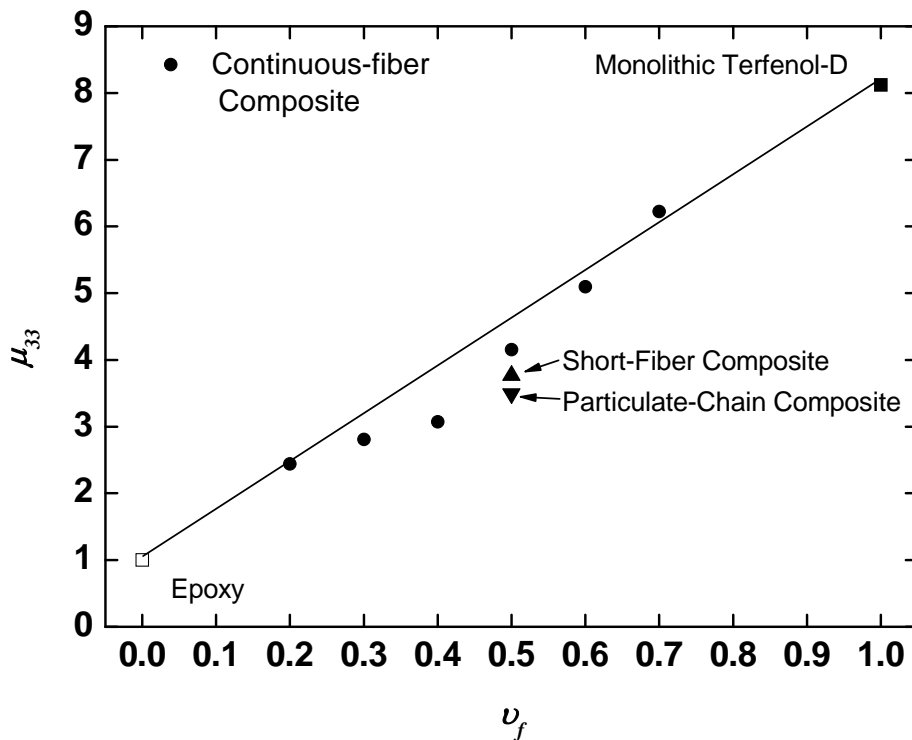


Fig. 4.8 ν_f dependence of μ_{r33} at $H_{Bias} = 40$ kA/m for continuous-fiber composites ($\nu_f = 0.2 - 0.7$), monolithic Terfenol-D, short-fiber composite ($\nu_f = 0.5$), and particulate-chain composite ($\nu_f = 0.5$), where the symbols and line represent the experimental and calculated data, respectively.



The E_3^H versus ν_f of all samples is illustrated in Fig. 4.9, in conjunction with the classical composite formulations for the lower and upper bounds expressed in Eqs. (4.7) and (4.8), respectively [43–47]:

$$E_3^H = \frac{E_3^{T-D} E^{Epoxy}}{\nu_f E^{Epoxy} + (1 - \nu_f) E_3^{T-D}}, \quad (4.7)$$

$$E_3^H = \frac{\nu_f E_3^{T-D}}{\nu_f + (1 - \nu_f) \frac{S_{33}^{T-D}}{S_{11}^{Epoxy}}}. \quad (4.8)$$

It is found that the E_3^H values of the continuous-fiber composites agree well with the upper bound formulation, confirming the true configuration of one-dimensionally aligned continuous fibers (fiber aspect ratio = 45:1) embedded in a three-dimensionally connected epoxy matrix. While the short-fiber composite ($\nu_f = 0.5$) has a reduced fiber aspect ratio of 4:1, its E_3^H value remains quite close to the values of the continuous-fiber composite ($\nu_f = 0.5$) and the upper bound formulation. The particulate-chain composite ($\nu_f = 0.5$) shows the quasi-behavior and is thus bounded by the upper and lower bounds. It can be expected that particulate-chain composites with $\nu_f < 0.5$ and > 0.5 are likely described by the lower and upper bound formulations, respectively.

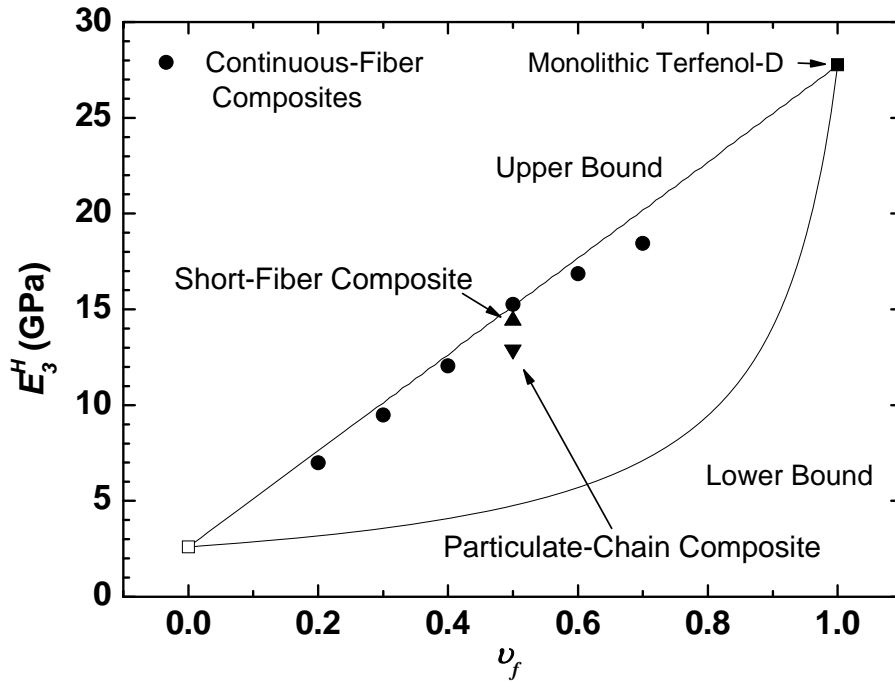


Fig. 4.9 Variation of E_3^H with ν_f at $H_{Bias} = 40$ kA/m for continuous-fiber composites ($\nu_f = 0.2 - 0.7$), monolithic Terfenol-D, short-fiber composite ($\nu_f = 0.5$), and particulate-chain composite ($\nu_f = 0.5$), where the symbols and lines represent the experimental and calculated data, respectively.

Figure 4.10 relates the ν_f dependence of d_{33} for all samples with the classical composite formulations for the lower and upper bounds expressed in Eqs. (4.9) and (4.10), respectively [44–48] as follows:

$$\nu_f \frac{d_{33}^{T-D} - d_{33}}{d_{33}^{T-D} + 2d_{33}} + (1 - \nu_f) \frac{d_{33}^{Epoxy} - d_{33}}{d_{33}^{Epoxy} + 2d_{33}} = 0, \quad (4.9)$$

$$d_{33} = \frac{\nu_f d_{33}^{T-D}}{\nu_f + (1 - \nu_f) \frac{S_{33}^{T-D}}{S_{11}^{Epoxy}}}. \quad (4.10)$$

It is found that the d_{33} values of the continuous-fiber composites generally exceed the upper bound formulation for the whole range of ν_f . The short-fiber composite ($\nu_f =$



0.5) is well-predicted by the upper bound formulation, while the particulate-chain composite ($\nu_f = 0.5$) can be predicted by either the upper or lower bound formulation. The results are again in good agreements with the findings associated with Fig. 4.6, elucidating the existence of combined thermal-induced residual compressive stresses, large fiber aspect ratio, and [112] texturing in the continuous-fiber composites.

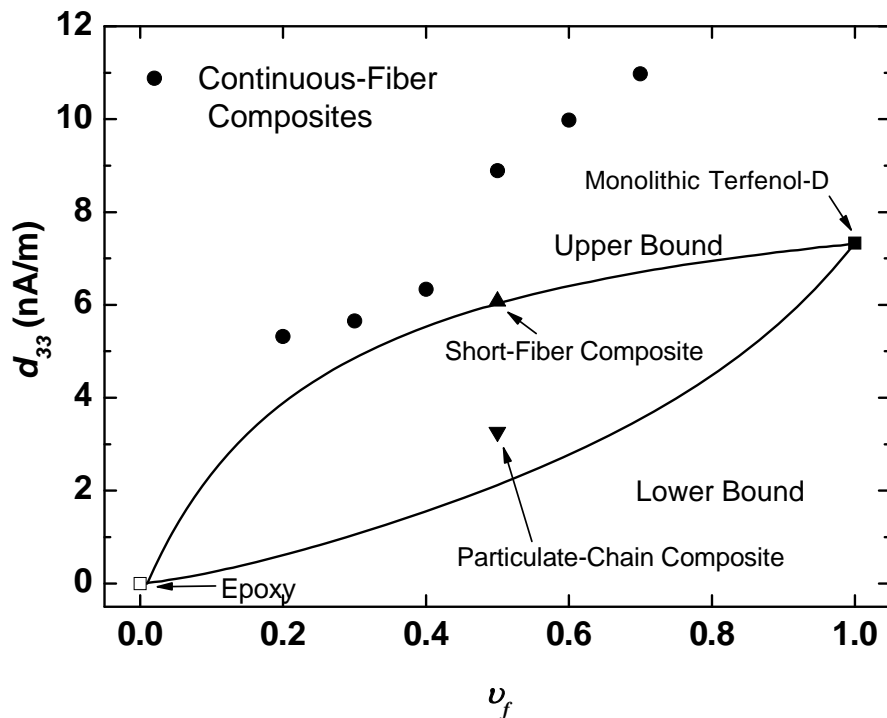


Fig. 4.10 ν_f dependence of d_{33} at $H_{Bias} = 40$ kA/m for continuous-fiber composites ($\nu_f = 0.2 - 0.7$), monolithic Terfenol-D, short-fiber composite ($\nu_f = 0.5$), and particulate-chain composite ($\nu_f = 0.5$), where the symbols and lines represent the experimental and calculated data, respectively.



Figure 4.11 plots the variations of k_{33} with ν_f for all samples, along with the classical composite formulations for the lower and upper bounds shown in Eqs. (4.11) and (4.12), respectively [64–68] as follows:

$$\nu_f \frac{k_{33}^{T-D} - k_{33}}{k_{33}^{T-D} + 2k_{33}} + (1 - \nu_f) \frac{k_{33}^{Epoxy} - k_{33}}{k_{33}^{Epoxy} + 2k_{33}} = 0, \quad (4.11)$$

$$k_{33} = \frac{\nu_f k_{33}^{T-D}}{\nu_f + (1 - \nu_f) \frac{S_{33}^{T-D}}{S_{11}^{Epoxy}}}. \quad (4.12)$$

k_{33} of the continuous-fiber composites increases rapidly with increasing ν_f but tends to level off and even larger than the monolithic Terfenol-D for $\nu_f > 0.4$. The higher value of k_{33} in comparison with Terfenol-D is due to the improved magnetomechanical coupling as discussed in Fig. 4.7. For the short-fiber composites, their k_{33} values can be predicted by the upper or lower bound formulation, depending on ν_f . For the particulate-chain composites, the description based on the lower bound formulation is more suitable.

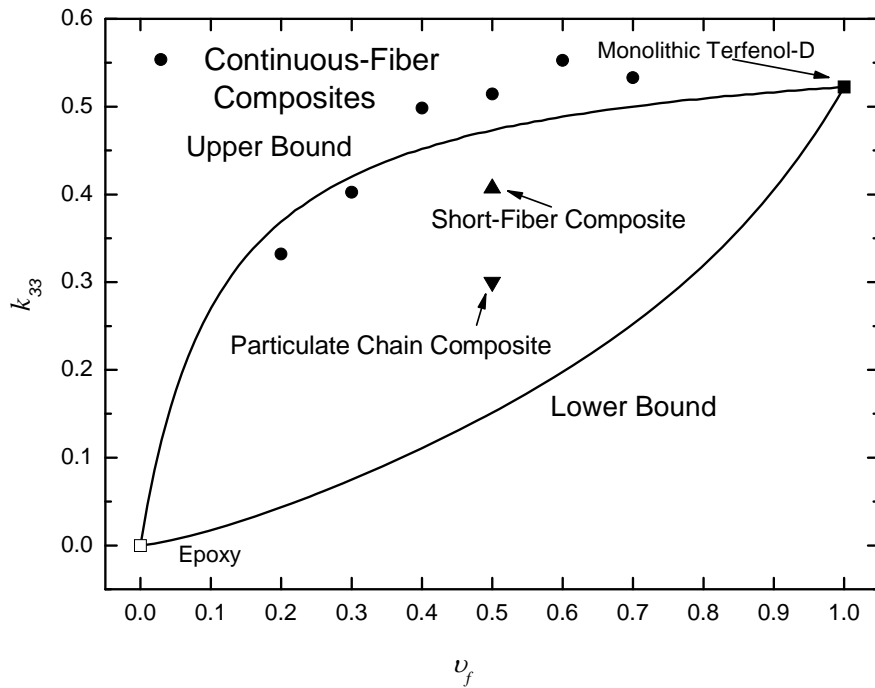


Fig. 4.11 v_f dependence of k_{33} at $H_{Bias} = 40$ kA/m for continuous-fiber composites ($v_f = 0.2 - 0.7$), monolithic Terfenol-D, short-fiber composite ($v_f = 0.5$), and particulate-chain composite ($v_f = 0.5$), where the symbols and lines represent the experimental and calculated data, respectively.



Chapter 5

Applications to Smart Devices

5.1 Introduction

Having been confirmed in the previous chapters, continuous-fiber composites, which possess superior quasistatic and dynamic magnetostrictive properties when compared with their monolithic Terfenol-D, short-fiber composites, and particulate-chain composites, make them a promising type of engineering magnetostrictive material for smart actuator and transducer applications. In fact, the success development of a practical device to maximally include the superior properties as observed in its parental smart material relies heavily on the design and fabrication technologies as well.

In this chapter, two interesting types of smart devices are designed, analyzed, fabricated and characterized to demonstrate the application potential of the continuous fiber composites. These devices include a tunable vibration absorber incorporating piezoelectric-magnetostrictive sensor/actuator and a 64 kHz sandwich transducer. The first device is used to exhibit the quasi-static property of the composite and the second device is intended to demonstrate the dynamic property of the continuous-fiber composites. For each device, the application background will be introduced. Then, the device's structure and operating principle will be described. Later, the fabrication and characterization will be disclosed. Finally, the concluding remarks will be included.



5.2 Tunable Vibration Absorber

5.2.1 Application Background

Tuned vibration absorbers are pre-tuned passive vibration absorption devices comprising a predetermined set of passively damped mass and spring to reduce the susceptibility to vibrations of a structure at a particular resonance frequency [49]. Subsequent tuning of the natural frequencies of these absorbers is impracticable once the absorbers are designed and fabricated. Adjustable tuned vibration absorbers usually have a damped mass and an adjustable spring such that fine-tuning of their designated natural frequencies is achieved manually by adjusting the stiffness of the spring through some mechanical means [50].

Tunable vibration absorbers (TVA) often utilize smart materials (e.g. PZT piezoelectric ceramics, Terfenol-D magnetostrictive alloys or Nitinol shape memory alloys) as the principal tuning means to provide the distinct feature of tunable stiffness via an external tuning signal [51–53]. With such tuning means, one may easily and precisely adjust the natural frequency of such a TVA to optimally match a structural resonance frequency and thereby absorb structural vibrations without adding any extra component and affecting the vibration levels of the structure at other frequencies.

While effectiveness and usefulness, the existing TVAs are incapable of self-sensing structural vibrations for the implementation of real-time, closed-loop tuning of their natural frequencies; they are limited to an open-loop mode of operation instead. Although it is possible to establish a closed-loop operation via an installation of vibration sensors (e.g., accelerometers) on the vibrating structures and/or on the



TVA, this method not only increases engineering costs but also leads to difficulties in assuring a reasonably high degree of TVA-sensor collocation. In view of this, we have developed a promising new type of TVA, comprising a specifically designed smart materials-based sensoriactuator connected to a mounting frame by two flexible beams coupled to axial ends of the sensoriactuator, to provide the real-time, closed-loop tuning capability in a simple, cost-effective and reliable manner [54]. In this study, we describe the working principle of the smart TVA with a piezoelectric-magnetostrictive (PE-MS) sensoriactuator and present the structure, tunability, sensibility and absorbability of a prototype TVA with the designated natural frequency of 63 Hz in the absence of external tuning signals.

5.2.2 Structure and Operating Principle

Figure 5.1 shows the conceptual design of the smart TVA. The PE-MS sensoriactuator is lumped, in this design, using a damped mass $2M$, and is integrated with two flexible beams and a mounting frame to form the smart TVA. Each of the flexible beams acts as a spring in the transverse (or y) direction to support the lumped damped mass on one side. These flexible beams are subject to an axial force F provided by the lumped damped mass (i.e. the MS actuator of the sensoriactuator) in the x direction. The two flexible beams are made of the same material having Young's modulus E_b and density ρ_b . Besides, they are designed with the same length L_b , width w_b and thickness t_b so that each of them has a rectangular cross-section with $w_b > t_b$, area $A_b (= w_b t_b)$, inertial moment $I_b (= w_b t_b^3 / 12)$ and axial stiffness $k_b (= E_b A_b / L_b)$. It is assumed that the mid-planes of the two flexible beams are oriented in

the xoz plane. The conceptual design in Fig. 5.1 then behaves essentially a continuous dynamic beam system with the lumped damped mass situated in the middle of the system. It is also assumed that the system operates fundamentally in its first bending mode with the lumped damped mass vibrating along the y direction. This suggests that tuning, in the smart TVA, is based on the sensitivity of bending stiffness and bending natural frequency of the system in response to the axial force exerted on the system while sensing is mainly governed by the sensitivity of inertial force of the lumped damped mass with respect to structural vibrations. In other words, when an optimally tuned natural frequency is achieved in the smart TVA, the lumped damped mass (i.e., the PE sensors of the sensoriauator) will experience the maximum inertial force in the y direction, giving out an indication of the optimal absorption of vibrational energy from the vibrating structure by the smart TVA.

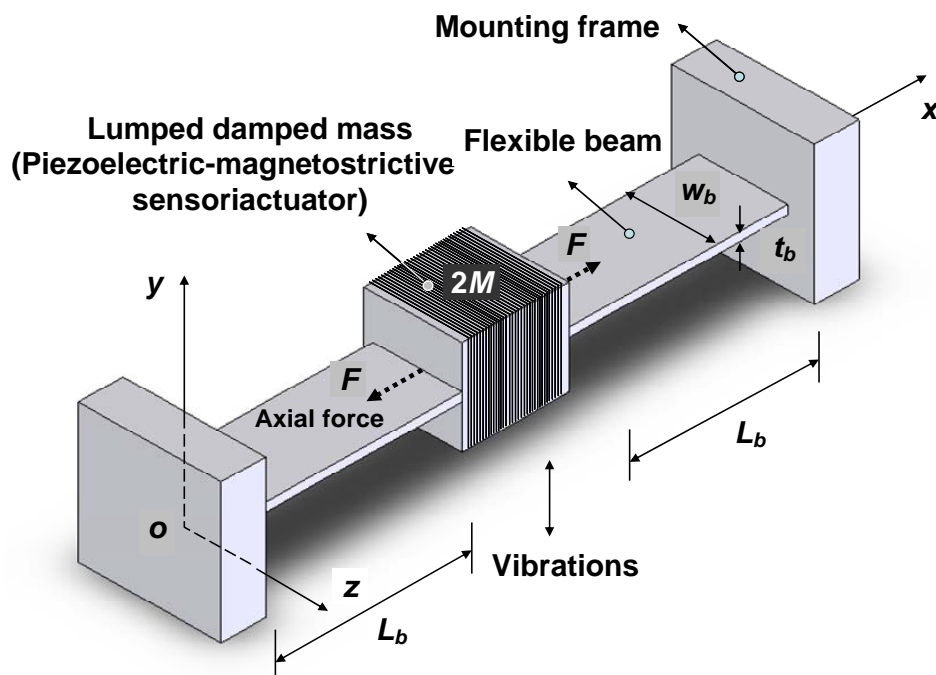


Fig. 5.1 Conceptual design of the smart TVA.



Since the conceptual design in Fig. 5.1 exhibits mirror symmetry, the continuous dynamic beam system can be simplified as a half model in Fig. 5.2. The single flexible beam is assumed to be mechanically clamped at one end while its other end is attached to half the lumped damped mass (i.e., M) with a roller-like movement in the y direction. Rayleigh's method [55,56] is used to calculate the tunable natural frequency of the system (i.e. the natural frequency of the smart TVA in the presence of an external tuning signal). A mode shape function that satisfies the boundary conditions of the system can be expressed as

$$u(x) = 1 - \cos \frac{\pi}{L_b} x, \quad (5.1)$$

where u = motion of the system in the y direction and x = position coordinate in the x direction. According to Rayleigh's method [55,56], the modal bending stiffness k and modal mass m of the first bending mode are determined, respectively, to be

$$k = \frac{\pi^2}{L_b} \left[E_b I_b \left(\frac{\pi}{L_b} \right)^2 - F \right] \quad (5.2)$$

and

$$m = 3\rho_b A_b L_b + 8M. \quad (5.3)$$

Therefore, the tunable natural frequency of the smart TVA f , which corresponds to the first bending natural frequency of the system acted with an axial force F , is obtained as follows:

$$f = \frac{1}{2\pi} \sqrt{\frac{\frac{\pi^2}{L_b} \left[E_b I_b \left(\frac{\pi}{L_b} \right)^2 - F \right]}{3\rho_b A_b L_b + 8M}}. \quad (5.4)$$

From Eqs. (5.2) and (5.4), it is known that F has the determinative effect on k and f .

If $F = 0$, f in Eq. (5.5) is reduced to

$$f_o = \frac{1}{2\pi} \left(\frac{\pi}{L_b} \right)^2 \sqrt{\frac{E_b I_b L_b}{3\rho_b A_b L_b + 8M}}, \quad (5.5)$$

where f_o = designated natural frequency of the smart TVA in the absence of external tuning signals. If F is a tensile force such that its sign is negative, both k and f can be tuned to increase with increasing F . Conversely, if F is a compressive force such that it has a positive sign, both k and f of the system can be tuned to decrease with increasing F . This indicates that there exists a critical (compressive) axial force F_{cr} in the system at which both k in Eq.5.2 and f in Eq.5.4 vanish, giving

$$F_{cr} = E_b I_b \left(\frac{\pi}{L_b} \right)^2. \quad (5.6)$$

Combining Eqs. (5.4), (5.5), and (5.6), we have

$$\frac{f}{f_o} = \sqrt{1 - \frac{F}{F_{cr}}}. \quad (5.7)$$

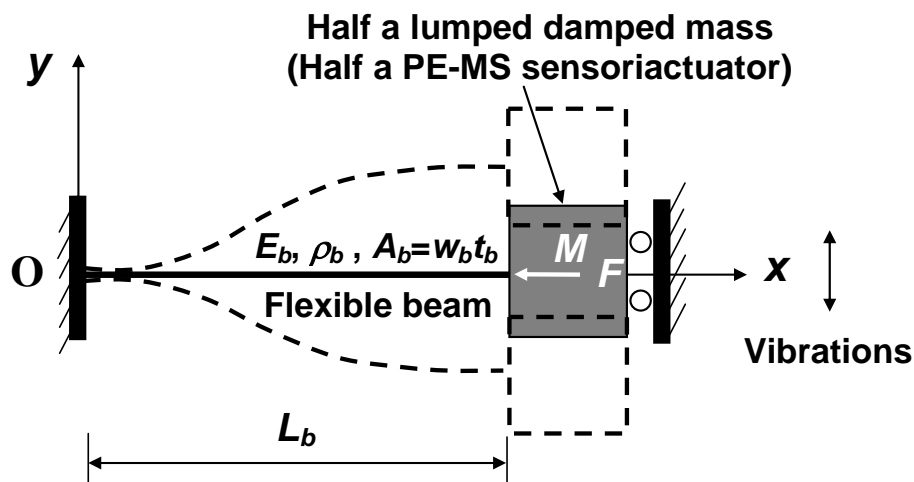


Fig. 5.2 Simplified dynamic model for the conceptual design.



To practically realize the smart TVA described in the previous paragraph, the axial force F is to be generated by the MS actuator of a PE-MS sensoriauator and the MS actuator is to be energized by an external tuning magnetic field H . Hence, the evaluation of the relationship between H and F , and hence H and f , is practically important for designing the smart TVA. By replacing the lumped damped mass in Figs. 5.1 and 5.2 by a PE-MS sensoriauator with an equivalent mass $2M$, the generated F can be related to H and properties of both the MS actuator and the flexible beams-mounting frame structure by

$$F = \frac{k_a k_m}{k_a + k_m} L_a d_{33} H, \quad (5.8)$$

where k_a = axial stiffness of the MS actuator; k_m = axial stiffness of the flexible beams-mounting frame structure; L_a = length of the MS actuator; and d_{33} = strain coefficient of the MS actuator. It is noted that k_a and k_m in Eq. (5.8) can further be expressed as

$$k_a = E_a^H \frac{A_a}{L_a} \quad (5.9)$$

and

$$k_m = \frac{k_b k_f}{k_b + k_f}, \quad (5.10)$$

where E_a^H = Young's modulus of the MS actuator at constant H ; A_a = cross-section area of the MS actuator; k_b = axial stiffness of the flexible beams; and k_f = axial stiffness of the mounting frame. Equation (5.8) states that in the absence of the flexible beams-mounting frame structure such that $k_m = 0$, the MS actuator will produce free deformation with zero F output. On the other hand, when the flexible



beams-mounting frame structure is sufficiently rigid such that $k_m \rightarrow \infty$, the generated F will approach to its blocked value, giving $F \sim F_B = k_a L_a d_{33} H$. Nevertheless, the critical external tuning magnetic field H_{cr} required to create the critical axial force F_{cr} in the smart TVA, according to Eq. (5.8), is

$$H_{cr} = \frac{k_a + k_m}{k_a k_m L_a d_{33}} F_{cr}. \quad (5.11)$$

Combining Eqs. (5.7), (5.8), and (5.11), we have

$$\frac{f}{f_o} = \sqrt{1 - \frac{F}{F_{cr}}} = \sqrt{1 - \frac{H}{H_{cr}}}. \quad (5.12)$$

The tuning curve based on Eq. (5.12) is plotted in Fig. 5.3. Recalling that magnetostriction in most existing MS materials (e.g., Terfenol-D) is positive (i.e., elongation) irrespective of the sign of H [57]. Accordingly, F , in this case, is essentially a compressive force so that the resulting TVA features unidirectional low-frequency tuning from f_o . Figure 5.3 also reveals the existence of a nonlinear relationship between the frequency ratio f/f_o and the magnetic field ratio H/H_{cr} (or the force ratio F/F_{cr}). The nonlinearity increases significantly for H/H_{cr} (or F/F_{cr}) in excess of 0.35. Thus, the linearity limit of f/f_o is found to be about 0.8 at H/H_{cr} (or F/F_{cr}) = 0.35. This, in turn, implies the maximum linear tunability of natural frequency of 20 % in the smart TVA.

In practice, when such a smart TVA is employed in vibration absorption of its underneath structure with a resonance frequency f_r , it is required that f of the smart TVA be tuned from f_o to f_r . At a steady-state condition, if f is tuned to approach f_r , the inertial force acting on the lumped damped mass will be increased; and at $f = f_r$, this inertial force will be maximized due to the effect of structural resonance. Using

this unique feature, a practical smart TVA possessing the attractive functionality of tuning-while-sensing is realized by replacing the lumped damped mass by a PE-MS sensoriauator to be described in the next section.

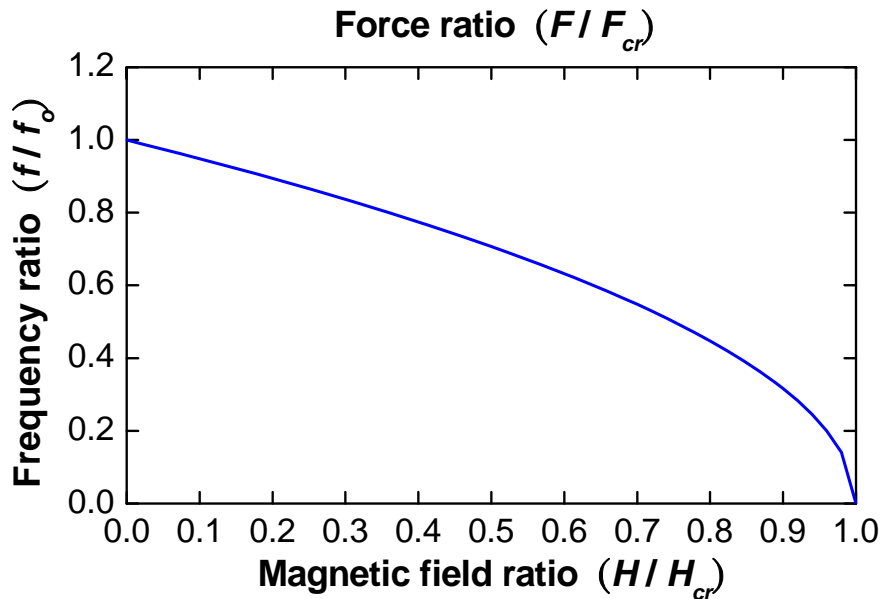


Fig. 5.3 Graphical illustration of the relationship between the frequency ratio (f / f_0), magnetic field ratio (H / H_{cr}) and force ratio (F / F_{cr}) of the smart TVA shown in Fig. 5.1.

5.2.3 Fabrication

The fabricated smart TVA is shown in Fig. 5.4. This TVA has dimensions 160 mm (length) \times 54 mm (width) \times 50 mm (height) and a mass 550 g. The two flexible beams were made of stainless steel 304 (SST304) and had the same dimensions of 32 mm long, 6.5 mm wide and 0.56 mm thick. The mounting frame was also made of SST304 and had screw holes in its top and bottom plates for installation of the TVA onto vibrating structures. The lumped damped mass $2M$ in Figs. 5.1 and 5.2 was replaced by a PE-MS sensoriauator of mass 100 g.

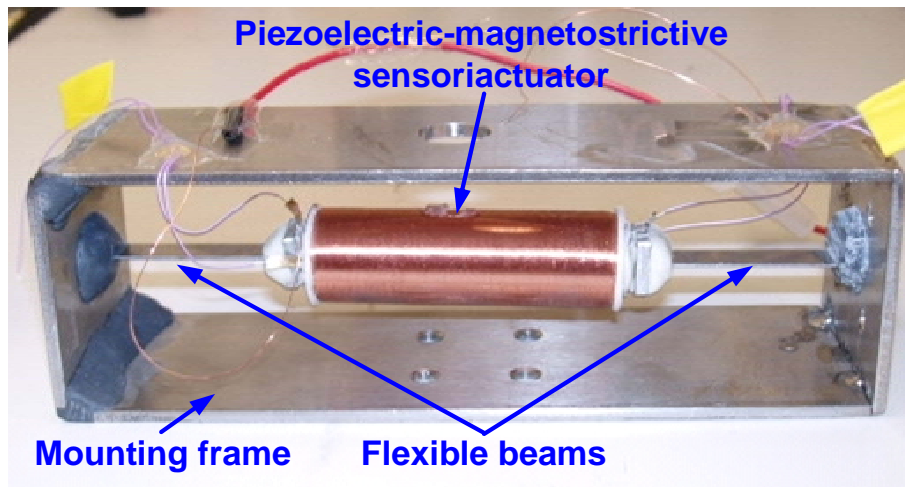


Fig. 5.4 A smart TVA prototype.

Figure 5.5 shows the assembly diagram of the PE-MS sensor/actuator. The sensor/actuator was formed by inserting a self-made, rod-shaped, continuous-fiber composite actuator (60 mm long, 12 mm diameter) into a solenoid, sandwiching the MS composite actuator between two PKI502 PZT piezoelectric ceramic patch sensors (10 mm diameter, 1 mm thickness) and then cementing the whole sensor/actuator assembly with two SST304 back plates. The MS composite actuator was prepared by embedding and aligning 0.6 volume-fraction Terfenol-D particles in Araldite LY564/HY2954 epoxy matrix. This composite material has been shown to possess distinct advantages of reduced eddy-current losses, brittleness, cost and increased shape novelty compared to its monolithic Terfenol-D for advanced actuator and transducer applications [56,58]. Detailed fabrication process of the composite can be found from Chapter 2 and the material properties are extracted from Chapter 3. The solenoid, having 13 layers of 273-turn AWG 32 enameled copper wire wrapped parallel on a Teflon bobbin, was used to supply the tuning magnetic field H to the continuous-fiber composite actuator. Two copper foils, each of 0.5 mm thickness,

were used as electrodes for connection of electrical leads to each of the two PE patch sensors. Two polyimide layers, each of 0.5 mm thickness, were inserted between the MS composite actuator and the signal electrode of the PE patch sensors to avoid short-circuiting the actuator and sensor signals. Some important geometric and material parameters of the MS composite actuator and the flexible beams-mounting frame structure are summarized in Tables 5.1 and 5.2, respectively.

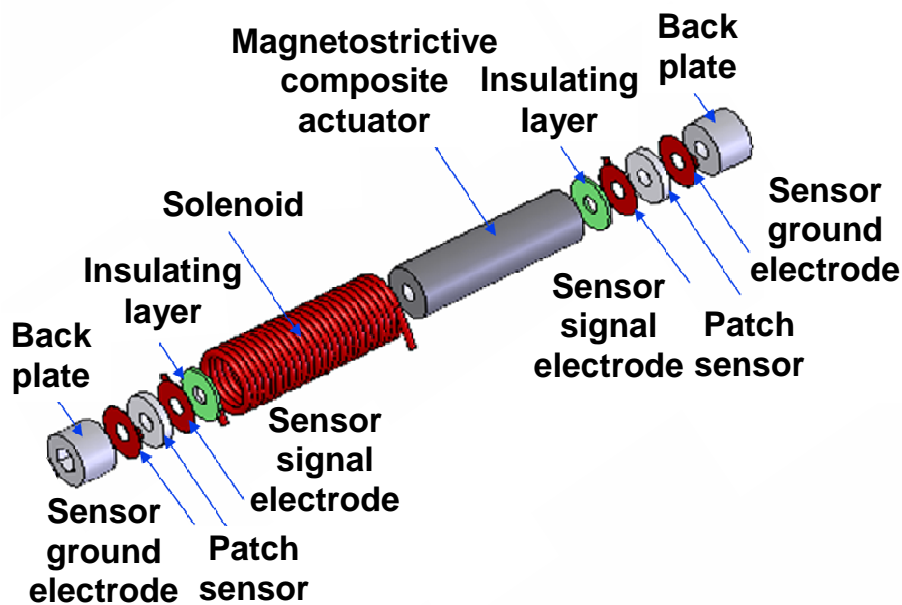


Fig. 5.5 Assembly diagram of the PE-MS sensor/actuator.



Table 5.1 Some important geometric and material parameters of the MS composite actuator used in the sensoriauator.

Parameter	Value
Dimensions: length L_a (mm)	60
diameter D_a (mm)	12
MS strain coefficient, d_{33} (ppm/Oe)	1.02
Young's modulus at constant H , E_a^H (GPa)	15.22
Maximum linear magnetostriction (ppm)	790
Maximum linear magnetic field (Oe)	700

Table 5.2 Some important geometric and material parameters of the flexible beams-mounting frame structure.

Item	Parameter	Value
Flexible beams	Dimensions (mm): length L_b	32
	width w_b	6.5
	thickness t_b	0.56
	Inertial moment, I_b (pm^4)	0.095
	Axial stiffness, k_b (N/ μm)	22.75
	Young's modulus, E_b (GPa)	200
	Density, ρ_b (kg/m^3)	7800
Mounting frame	Axial stiffness, k_f (N/ μm)	5.8



With this configuration, the sensor/actuator not only serves as a lumped damped mass for the smart TVA, but also functions as an actuator to provide an axial force to the flexible beams (via the MS composite actuator) and as a sensor to monitor the signals associated with structural vibrations (via the two PE patch sensors). Through adjusting the dc tuning magnetic field (i.e. an external tuning signal) applied to the MS composite actuator of the sensor/actuator to change the axial force to the flexible beams, the bending stiffness of the flexible beams is changed and the natural frequency of the smart TVA is tuned. Through monitoring the maximum signal amplitude generated by the PE patch sensors in response to a structural resonance, an optimally tuned natural frequency of the smart TVA (i.e. tuned to the targeted structural resonance) can be achieved for active vibration absorption applications.

5.2.4 Characterization

5.2.4.1 Tunability

The smart TVA was installed on a shaker (LDS V406) for evaluation of its frequency tunability (Fig. 5.6). A dynamic signal analyzer (SigLab 50-84) was used to generate an analog random signal ranging from 0 to 1 kHz to a power amplifier (LDS PA100E) so as to excite the shaker to provide a reference vibration along the y direction. A commercial, light-weight (i.e., 4.2 g) accelerometer (ENDEVCO ISOTRON 256HX-10) was mounted on the surface of the sensor/actuator to measure the acceleration response in the y direction. The dynamic signal analyzer was also used to gather the frequency response function (FRF) of the input excitation signal and the output accelerometer signal. A dc power supply (Sorensen DHP200-15) was

employed to drive the solenoid for generating a dc tuning magnetic field H to the MS composite actuator, which, in response to H , then produces a static axial force F for tuning of the natural frequency of the smart TVA.



Fig. 5.6 Measurement setup for characterization of the smart TVA.

Figure 5.7 plots the measured FRFs of the smart TVA at various H . It is clear that the designated natural frequency of the smart TVA at zero tuning fields f_0 is 57.8 Hz. As H increases, the MS composite actuator expands and produces a larger F to the flexible beams, thereby reducing the bending stiffness of the flexible beams and hence the natural frequency of the smart TVA. At an increased H of 690 Oe, the natural frequency of the smart TVA is as low as 50.9 Hz, resulting in a large tunability of 12 %.

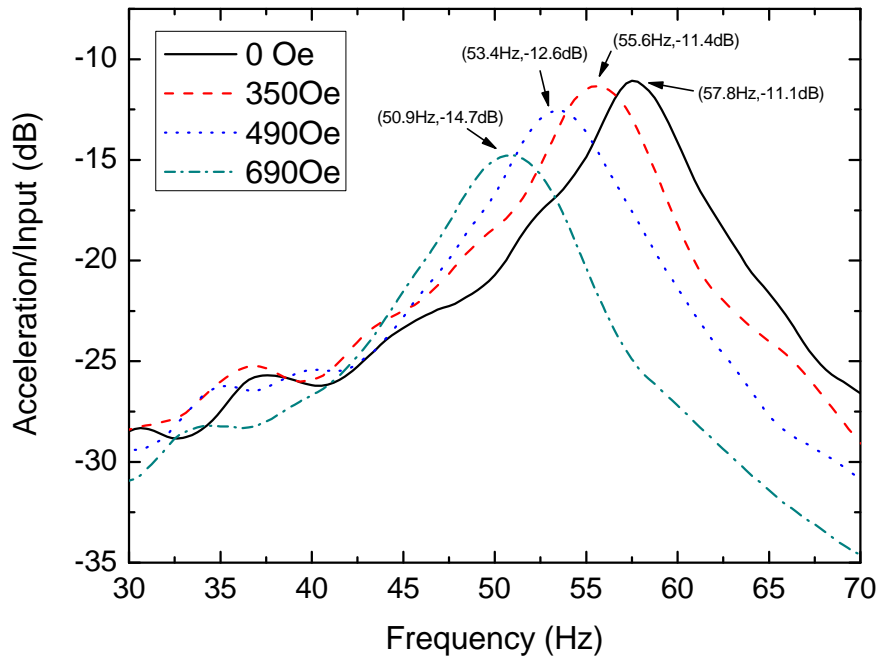


Fig. 5.7 Measured FRFs on the TVA under various magnetic tuning fields.

Figure 5.8 illustrates the measured (from Fig.5.6) and predicted [by Eq. (5.7)] natural frequencies f and predicted axial force F [by Eq. (5.6)] of the smart TVA as a function of H . It is obvious that the measured f are in good agreement with those obtained by prediction with the maximum error of less than 2 %. On the other hand, F is found to increase linearly from 0 to ~103 N when H is increased from 0 to 700 Oe. At $H = 690$ Oe, F is about 100 N, reaching about 44 % of F_{cr} of about 183 N [by Eq. (5.6)].

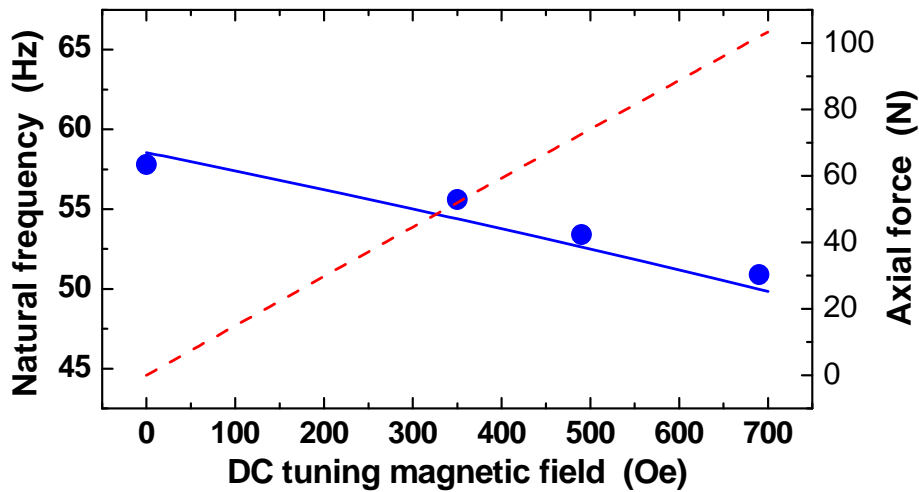


Fig. 5.8 Measured (symbol) and predicted (solid line) natural frequencies and predicted axial force (dotted line) as a function of dc tuning magnetic field.

5.2.4.2 Sensibility

Two different sensibility measurements were carried out, based on the embedded PE patch sensors, to demonstrate the self-sensing of (1) the natural frequency of the smart TVA and (2) the signals associated with a structural resonance.

The experimental setup for self-sensing of the natural frequency of the smart TVA was the same as that used in the tunability measurement. The FRFs measured by the PE patch sensors at each H were directly compared with those captured using the accelerometer installed on the surface of the sensor/actuator. Figure 5.9 shows two FRFs measured at $H = 350$ and 690 Oe. The natural frequencies measured by the PE patch sensors agree well with those detected by the accelerometer. This good agreement suggests that the PE patch sensors can effectively replace the commercial accelerometer for in-situ sensing of the natural frequency of the smart TVA.

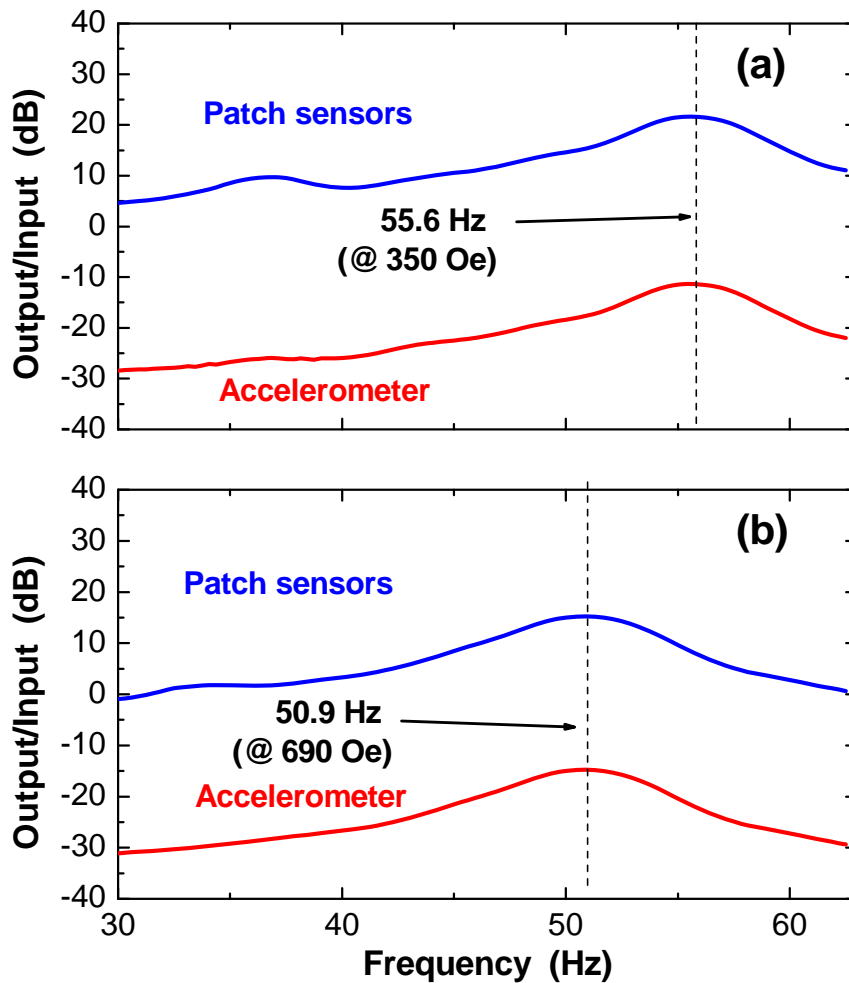


Fig. 5.9 FRFs measured using the PE patch sensors and a commercial accelerometer at (a) 350 and (b) 690 Oe.

To examine the sensing capability of the PE patch sensors at a structural resonance, the smart TVA was installed on the shaker that, in turn, was excited sinusoidally at 58 Hz to simulate a troublesome resonance. By applying different H to the MS composite actuator while monitoring the corresponding time-domain PE patch sensor signals, the vibration waveforms at different H are displayed in Fig. 5.10. It is seen that the amplitude of the PE patch sensor signal reaches a minimum at 0 Oe; it then increases with increasing H , and when H is increased to 350 Oe, the PE patch sensor signal is maximized in amplitude.

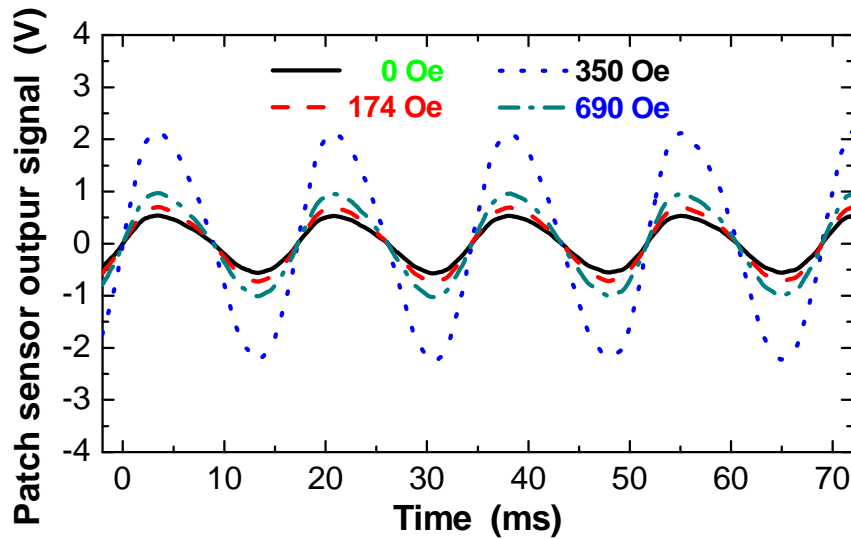


Fig. 5.10 PE patch sensor output signals at different dc tuning magnetic fields in response to a simulated resonance at 58 Hz.

It is known from the tunability curves in Figs. 5.7 and 5.8 that the natural frequency of the smart TVA at $H = 350$ Oe is 55.6 Hz. This confirms the optimal tuning of the smart TVA to match with the simulated structural resonance at 58 Hz. Further increasing H beyond 350 Oe decreases the amplitude of the PE patch sensor output, reflecting over-tuning of the smart TVA. Consequently, this in-situ tuning-while-sensing capability is definitely an advantage for the advance of the active vibration control technology.

5.2.4.3 Vibration Absorption

Impulse test was implemented to acquire the FRF of the steel plate-neoprene resilient mounts structure, which shown in Fig. 5.11. The size of the steel plate is 245 x 285 x 25mm and the weight is 13.5kg and the three neoprene damper is place under the steel plate. An impulse hammer was used to excite the structure and an accelerometer was employed to measure the response (Fig. 5.11). When the applied magnetic field reaches to 350 Oe, the TVA is tuned to 49.1 Hz. The measured FRF by the impulse test under the control is shown in Fig. 5.12 as dashed line. A 3.4 dB control is observed in the targeted resonance. The control result is significant, although the damping ratio of the test bed is quite large already.

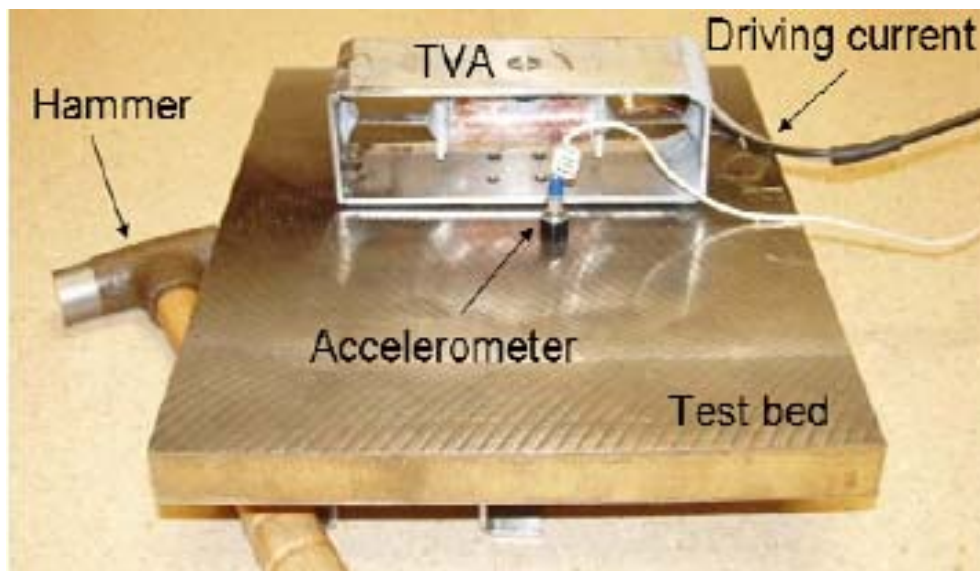


Fig. 5.11 Test bed for vibration control using smart TVA.

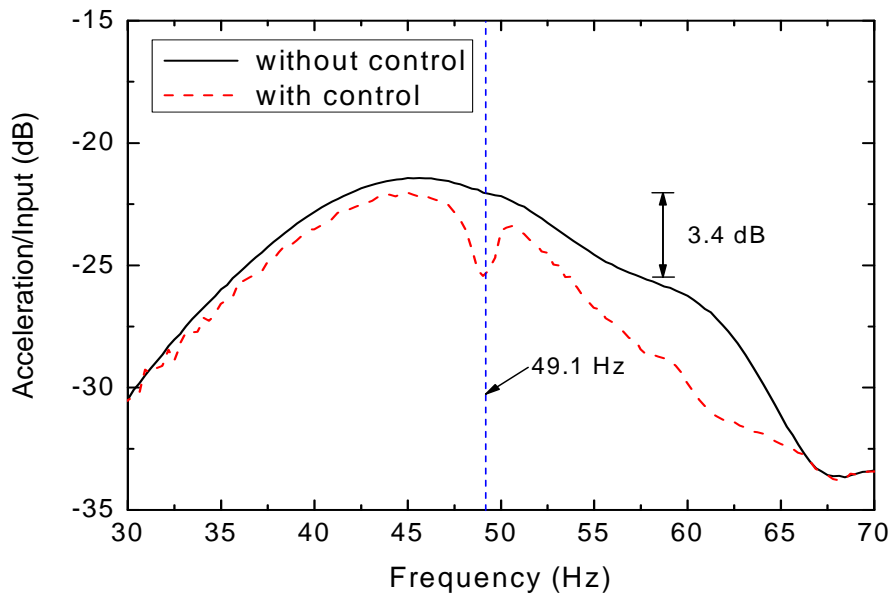


Fig. 5.12 Vibration absorption performance in a steel plate-neoprene resilient mounts structure.

5.2.4 Concluding Remarks

A novel smart TVA has been developed and evaluated, both theoretically and experimentally. The smart TVA consists of a force actuator-sensor unit suspended in a rigid frame by two flexible beams coupled to the axial ends of the force actuatorsensor unit and the frame. The force actuator-sensor unit comprised of a Terfenol-D continuous fiber composite-based force actuator sandwiched between two PZT piezoelectric ceramic-based force sensors to which they are clamped by two rigid back plates.. The measured natural frequency of the smart TVA is 57.8 Hz at zero magnetic fields. A significantly reduced natural frequency of 50.9 Hz, corresponding to a high tunability of 12%, has been achieved upon the application of a relatively low magnetic field of 690 Oe. The tunable natural frequencies of the smart TVA measured by the PE patch sensors of the sensoriauator agree well with



those obtained by a commercial accelerometer. A relatively large absorption of 3.4 dB has been obtained in a steel plate-neoprene resilient mounts structure. The results due to tuning of the natural frequency of the smart TVA while sensing of a structural resonance have demonstrated great promise of deploying the smart TVA for active absorption of vibrations in vibrating structures.



5.3 64 kHz Sandwich Ultrasonic Transducer

5.3.1 Application Background

Sandwich transducers have been widely used in sonic and ultrasonic applications to deliver sonic or ultrasonic energy to their loads. Examples include transducers for underwater sonar, industrial cleaning, machining, bonding and welding, dental and surgical tools, as well as chemical and food processing, to name a few. Historically, the design and application of the transducers have been intimately tied to piezoelectric materials, in particular lead zirconate titanate (PZT) piezoelectric ceramics and their composites. It was not until recently when a giant magnetostrictive rare-earth-iron alloy Terfenol-D was discovered. While possessing a significantly higher power-handling capability than PZT and having been commercially adopted in sonic transducers, further application of monolithic Terfenol-D in sonic and ultrasonic transducers is not yet successful due to the presence of eddy-current losses that increase rapidly with frequency.

Our continuous-fiber composites, consisting of one-dimensionally aligned Terfenol-D fibers embedded in a three-dimensionally connected passive epoxy matrix, are not subject to this problem due to increased electrical resistivity. Additional benefits of using these composites are their mechanical durability, tailorable properties, and cost effectiveness. Due to the improved in dynamic magnetomechanical properties of the composites, the use of the materials in sonic and ultrasonic transducers becomes feasible. In order to transplant the continuous-fiber composite technology to practical transducers, we have aimed in this section to



develop a 64 kHz sandwich transducer based on a tube-shaped continuous-fiber composite with Terfenol-D volume fraction of 0.6.

5.3.2 Design and Fabrication

Figure 5.13 shows a general structure of the magnetostrictive driver which is clamped by two metal slabs and a central pre-stressed screw. These two slabs are used to provide a desired mechanical bias to the composite tube. Furthermore, they prevent the transducer parts from fracturing under high drive field. Between two slabs, it consists of a magnetic circuit. This magnetic circuit is the main part of the driver. The magnetic circuit has a magnetostrictive composite tube sandwiched between a pair of ring-shaped permanent magnet. The composite-magnet assembly is situated in a drive solenoid. A pair of ring-shape permanent magnets is suited at both ends of the composite tube. It provides an average magnetic bias (dc) field to the composite tube such that the composite tube elongates along its length and produces a large initial static strain. The drive solenoid surround the composite tube for providing an oscillating strain centered on the initial static strain.

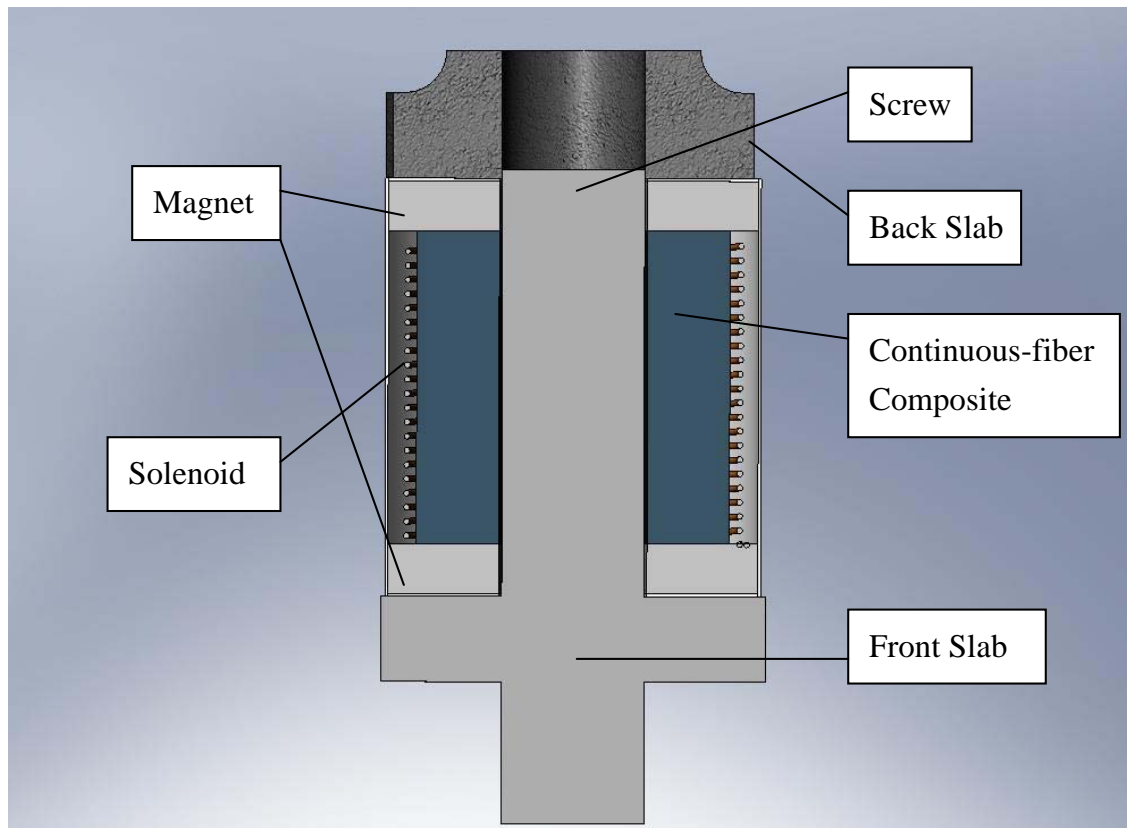


Fig. 5.13 Schematic diagram of the generic structure of magnetostrictive driver

The transducer is operated in resonance frequency, which is the value which all assemblies of the transducer oscillate together. The target operating frequency of ultrasonic bonding transducer is around 64 kHz. The resonant frequency depends on variety of parts. The most significant parts are the dimensions and material properties of the magnetostrictive composite tube and metal slabs. Moreover, magnitude of magnetic field bias and the mechanical pre-stress which is produced by two slabs also affect the resonant frequency and quality of wire bonding.

As the target of the transducer is operation with around 64 kHz. The magnetostrictive composite transducer functions as a half-wave, longitudinal, mass-



spring-mass, linear vibrator/motor to deliver maximum ultrasonic vibrations to its load at its resonance frequency. The transducer is made up of few parts; front slab, threaded shaft, back slab, a pair of permanent magnets, pair of magnetic flux guide a external flux guide and a Terfenol-D composite tube. Each part was assembled using different materials. According to the pervious study, the transducer has a length of around 16 mm (excluding the screw for load connection). The threaded shaft and the front slab are made of stainless steel 304, which is the most common grade of stainless steel. An aluminum alloy 7075 is used to fabricate the back slab. The thickness of these two slabs is around 3 mm. In between two slabs, a pair of permanent magnets, NdFeB, Neodymium Iron Boron, which form as a ring shape, and the thickness of magnets is about 1-3 mm. The most important part of the transducer is the Terfenol-D composite, which is located in the middle of the transducer and clamped by the permanent magnets. It is a tube shape which has inner diameter of 5 mm and outer diameter of about 11 mm. Furthermore, a copper wire solenoid surrounds the composite tube with a finite air gap in between. The solenoid is made by wrapping the copper wire parallel on the composite. To guide the magnetic flux into the composite tube, a pair of about 0.25 mm thick, Ni-based return-path rings on each end of the composite magnet assembly and a Ni-based external return-path cylinder having a wall thickness of around 0.3mm are created. The schematic diagram of the magnetostrictive composite sandwich transducer is shown in Fig. 5.14.

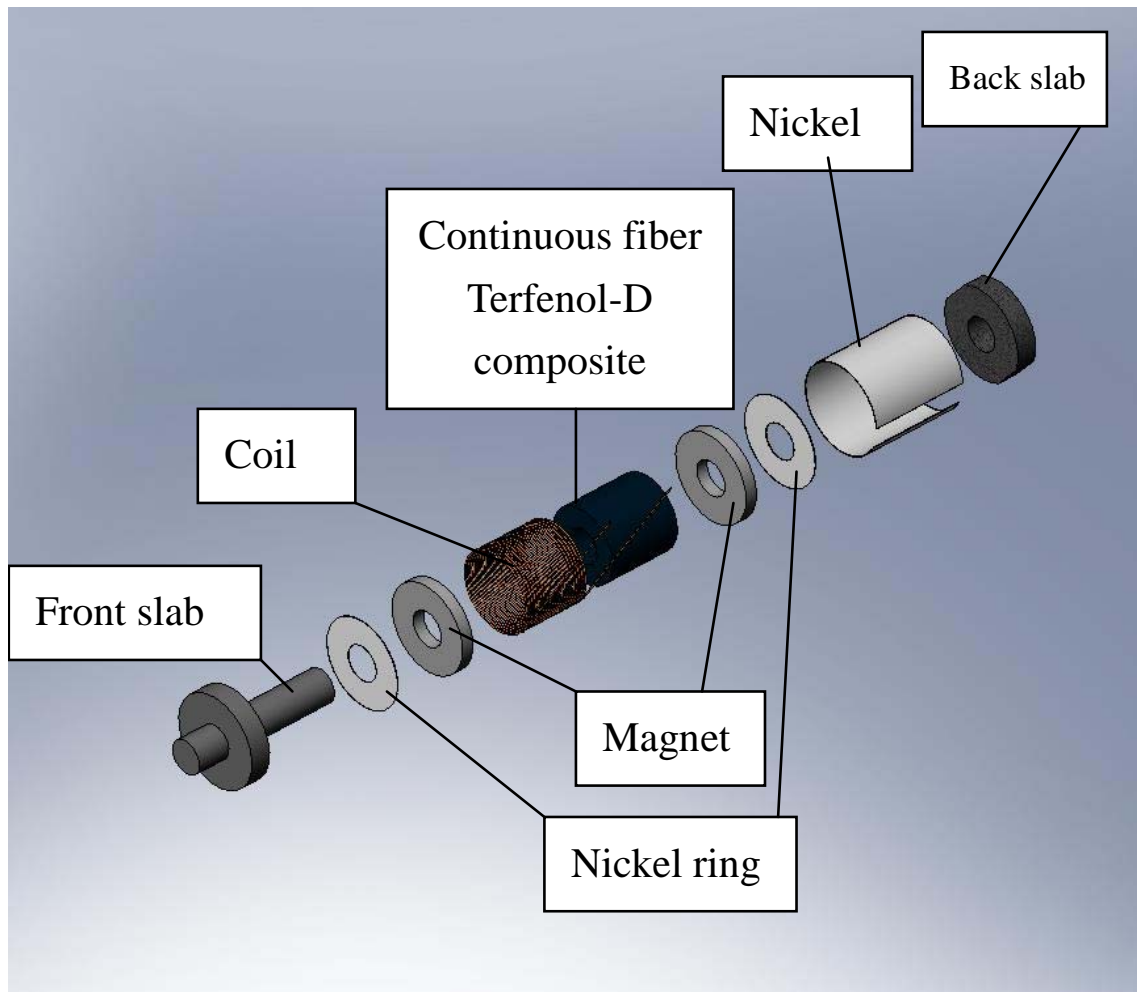


Fig. 5.14 Explode view of a 64 kHz Terfenol-D composite transducer

In this application, the design of the transducer was based on this previous design. By changing the length of the Terfenol-D composite and due to the difference volume fracture between Terfenol-D and epoxy and the fabrication process, the transducer with Terfenol-D continuous fiber composite has axial resonant frequency in around 64 kHz.

Since Terfenol-D composite transducer is a magnetic field based object and there is a pair of permanent magnets, magnet analysis is needed to observe the magnetic field distribution in the magnet circuit.



To simulate a 3-D magnet circuit analysis, this usually requires a huge number of elements to get an acceptable accuracy of the magnetic field distribution. Therefore to simplify the 3-D magnetic circuit problem and reduce the huge element number requirement, a 2-D planar model was used. Moreover, due to the symmetry, only half of the 2-D modal is drawn in the simulation.

To gain insight into the design of the magnetic circuit, an ANSYS 10.0 finite-element model was created to determine the distributions of the dc magnetic flux lines and magnetic field strength of the circuit. The PLANE13 element was used for the magnetic analysis. Magnetic properties of the composite tube, NdFeB permanent magnets, and nickel magnetic flux guide listed in Table 5.3 were input into the model. For magnetic analysis, excluding the modal analysis, an air region surrounding the magnetic circuit was needed to simulate the effect of infinite boundary permeability and coercive field is applied to generate magnetic field.



Table 5.3 Magnetic Properties of the transducer for simulation.

Materials	Relative Permeability	Coercive Field (A/m)
Terfenol-D Continuous fiber composite	5	--
NdFeB (Permanent magnet)	1.004	800000
Pure nickel (magnet flux guide)	600	--
Aluminum alloy 7075 (back slab)	1	--
Stainless Steel 304 (front slab and thread shaft)	1.02	--
Pure copper (solenoid)	1	--
Air	1	--

In the simulation, 2-D element PLANE 13 was used in all material regions, which shown in Fig. 5.15. PLANE 13 has a 2-D magnetic, electrical and structure field capability with limited coupling between the fields. Therefore this element is suitable for 2-D magnetic field distribution simulation. PLANE 13 is defined by four nodes with up to four degrees of freedom per node. The element has nonlinear magnetic capability for modeling B-H curves or permanent magnet demagnetization curves.

In the meshing, 3098 elements and 5907 nodes were produced. Since the most important part is the transducer, more elements and nodes formed, especially the magnetic circuit.

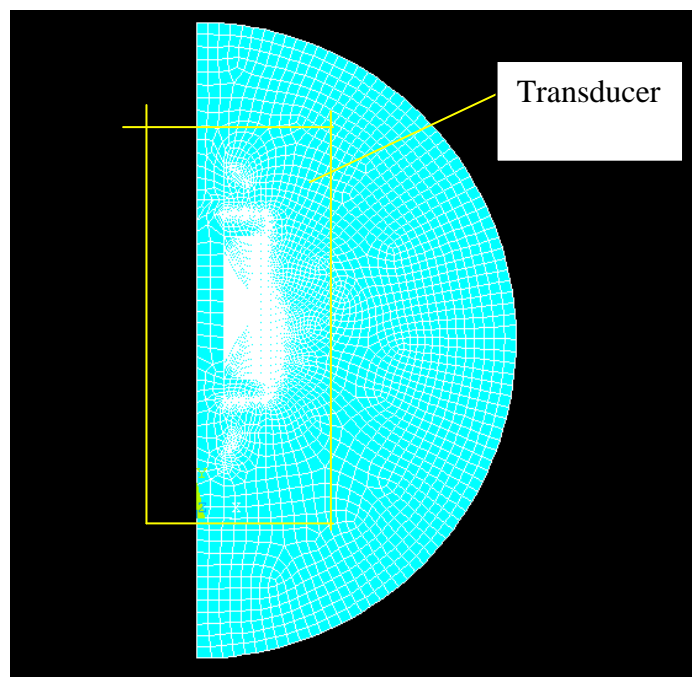


Fig. 5.15 Meshed 2D magnetic simulation drawing

After meshing, static analysis was chosen as the analysis type and the model was then run.

After simulation, a 2-D flux line distribution picture can be found in general “postproc”. According to the result in Fig. 5.16, there is only a small amount of leakage from the permanent magnets that does not flow through the composite tube. It is due to the magnetic flux guides which guide the magnetic field. If the external flux guide is not available, then the fewer magnetic fields will flow through the composite.

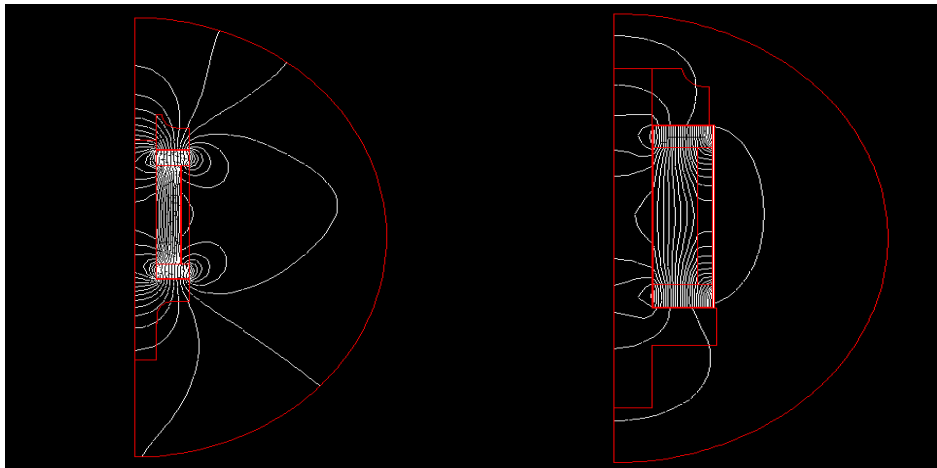


Fig. 5.16 Simulation result of magnetic field distribution analysis (a) without flux guide,
(b) with flux guide

When plotting the magnetic field strength against distance along composite tube in Fig. 5.17, a slightly uneven distribution of magnetic flux is observed along the length of the tube. It indicated that the existence of a non-uniform distribution of magnetic field strength. The magnetic field strength exhibits a parabolic shape with minimum field strength of 24.9kA/m occurring in the center of the composite tube. This effect may be attributed to the flux leakage and reluctance of the composite tube.

Nevertheless, an average magnetic field strength of 37.3kA/m is obtained to provide the desired magnetic bias to the transducer.

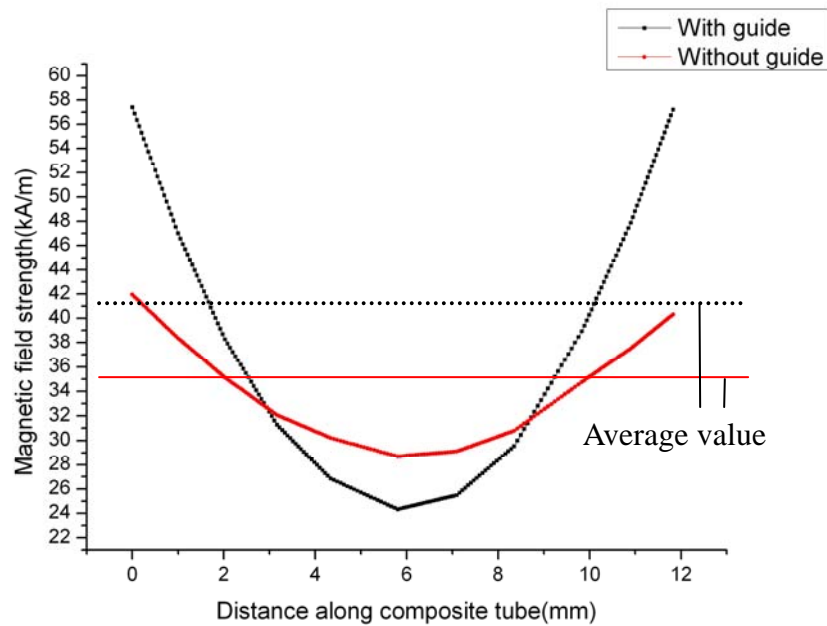


Fig 5.17 Comparison between with and without magnetic flux guide

Obviously, in Fig. 5.17 the distribution of magnetic field strength which the magnetic circuit without external flux guides is more even along the distance. However, it has an average magnetic field strength of 37kA/m which is smaller than the value of 41kA/m.



Table 5.4 Material properties of the continuous-fiber composite for simulation.

	Material properties	Values
Terfenol-D composite	Density	7900 kg/m^3
	Elastic deformation	$E_x = E_y = 5.62 \times 10^9 \text{ Pa}$ $E_z = 1.6 \times 10^{10} \text{ Pa}$ $G_{xz} = G_{yz} = 2.05 \times 10^9 \text{ Pa}$ $G_{xy} = 8.21 \times 10^9 \text{ Pa}$
	Poisson's ratio	$\nu_{xy} = 0.644$ $\nu_{xz} = \nu_{yz} = 0.214$
	Magnetostrictive constant(piezoelectric constant)	$d_{31} = -5.3 \times 10^{-9} \text{ nm/A}$ $d_{15} = 2.8 \times 10^{-8} \text{ nm/A}$ $d_{33} = 1.1 \times 10^{-8} \text{ nm/A}$
	Permeability	$\mu_{11}^T = 1.3 \times 10^{-5}$ $\mu_{33}^T = 5.3 \times 10^{-6}$



Table 5.5 Material properties of the transducer parts for simulation.

	Stainless steel 304	Aluminum alloy 7075	NdFeB
Density	8030 kg/m ³	2820 kg/m ³	7800 kg/m ³
Young's modulus	1.92 × 10 ¹¹ Pa	7.2 × 10 ¹⁰ Pa	1.6 × 10 ¹¹ Pa
Poisson's ratio	0.3	0.35	0.3
	Copper	Nickel	
Density	8900 kg/m ³	8900 kg/m ³	
Young's modulus	1.17 × 10 ¹¹ Pa	2.21 × 10 ¹¹ Pa	
Poisson's ratio	0.3	0.3	

Harmonic response analysis is used to predict the sustained dynamic behavior of the structures, thus to verify whether the designs will successfully overcome resonance, fatigue, and other harmful effects of forced vibrations or not.

According to the pervious study, magnetostrictive property is similar to piezoelectric effect, the transducer can simulate with a piezoelectric method, apply a magnetic flux to both end of Terfenol-D composite.

When a transducer is subjected to load (electrical energy) which is normal to the surface of composite, the transducer vibrates. However, the shape of vibration and the mode shape depend on the frequency of the applied load. If the frequency is equal to the natural frequency of the transducer, the mode shape in this frequency will be excited so that resonance occurs with enlarged amplitude.

In the harmonic analysis, voltages were applied to the surface of the Terfenol-D composite instead of applying current to the solenoid for producing



magnetic field. 1 kA/m was applied to one surface of the composite and 0 kA/m was supplied to another surface. In the simulation, SOLID 98 was used. It is a 10-nodes tetrahedral element. The element has a quadratic displacement behavior and is well suited to modal irregular meshes. Also it has lots of degree of freedom (displacement, temperature, voltage and magnetic). Moreover, major material properties can be input including piezoelectric matrix. Since the major surfaces of Terfenol-D composite are electrode resulting in equi-potential surfaces, the nodes of SOLID 98 that modal each of these surfaces have their voltage degrees of freedom coupled together so that the applied potential load can be conveniently placed on a single node of each electrode. The harmonic frequency range was set from 30 kHz to 90 kHz and number of substeps is 60. More substeps would have a smoother and accurate result. However it is time consuming and 1 kHz per steps is enough in this simulation.

The amplitude of the head of transducer in x, y and z direction against frequency was plotted in Fig.5.18. From the graphs, red line represent z-direction displacement, x-axis and y-axis displacement are represented by green and blue line respectively. According to Fig. 5.18, a large peak of red line is occurred in 64 kHz, which is the resonant frequency of its axial mode. Moreover, the x-axis and y-axis displacements are relatively small; the magnitude of z-axis displacement is over 100 times larger than the x-axis displacement and over 10000 times of the y-axis displacement in the same frequency. These results contribute that there was an axial mode in 64 kHz and it meets the requirement for 64 kHz wire bonding technique. However, there was another peak in z-axis displacement at 84 kHz. The magnitude of this peak is smaller than the previous one and the order of magnitude is only 10^{-16} ,

which is 10 times smaller than the peak at 64 kHz. Moreover, both displacement in x and y axis reach their largest peaks near this frequency value, especially x-axis displacement. An observable peak of x-axis displacement is shown in Fig. 5.18 whereas nothing can be observed for y-axis. Apart from these, the magnitude of maximum peak in x-axis displacement has the same order as z-axis displacement in 84 kHz. As mentioned before, lateral mode and undesirable mode near axial mode frequency would affect the quality of wire bonding. Therefore 84 kHz is not the best frequency to operate the transducer due to the presence of x direction displacement.

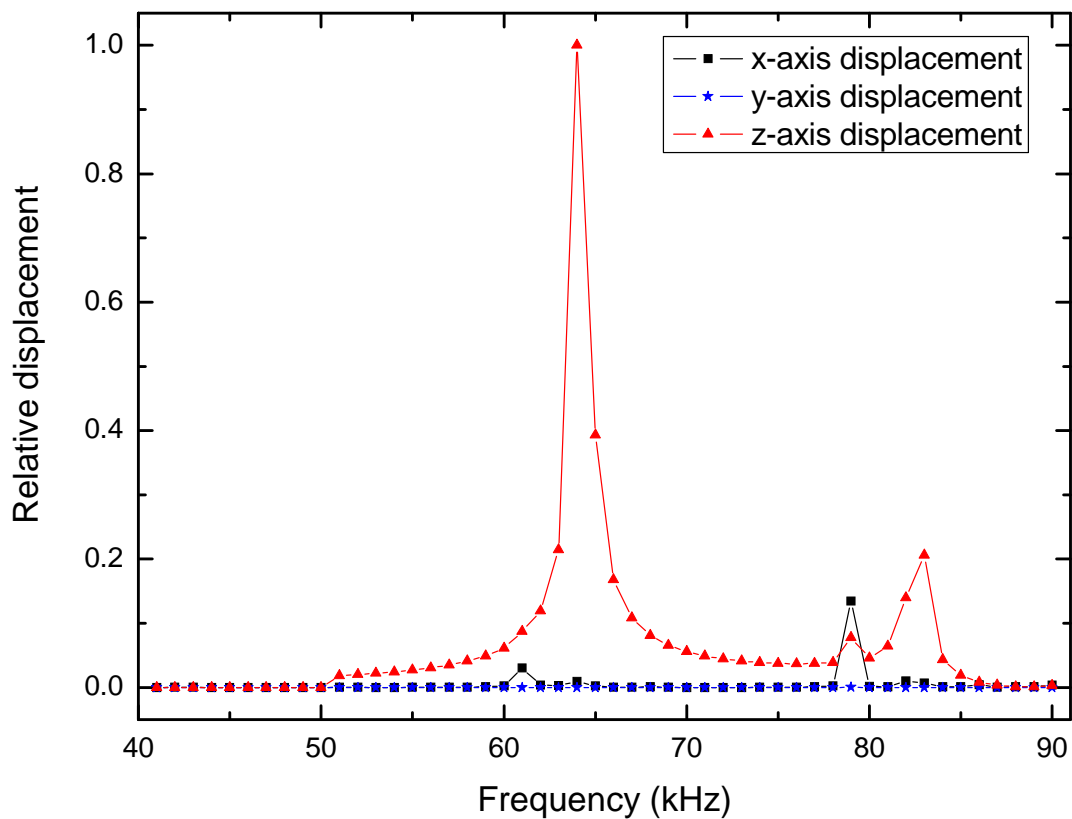


Fig.5.18 Harmonic analysis result in x-, y- and z-axis displacement



To conclude, the design of transducer meets the condition for 64 kHz wire bonding technology, and the simulation can help to predict the performance and shows the modes shape that cannot be seen in reality. After simulation, follow the dimension of every parts of transducer to fabricate these assemblies.

After simulation, the dimensions of the transducer parts were confirmed. Utilize this design to fabricate every parts of transducer. A tube of continuous-fiber composite was cut into 5 parts; they are 14mm, 10mm, 4mm, 3mm and 2mm long. Front slab, back slab, solenoid, magnetic flux guide and external flux guide were fabricated as the simulated dimensions which shown in Fig. 5.19.

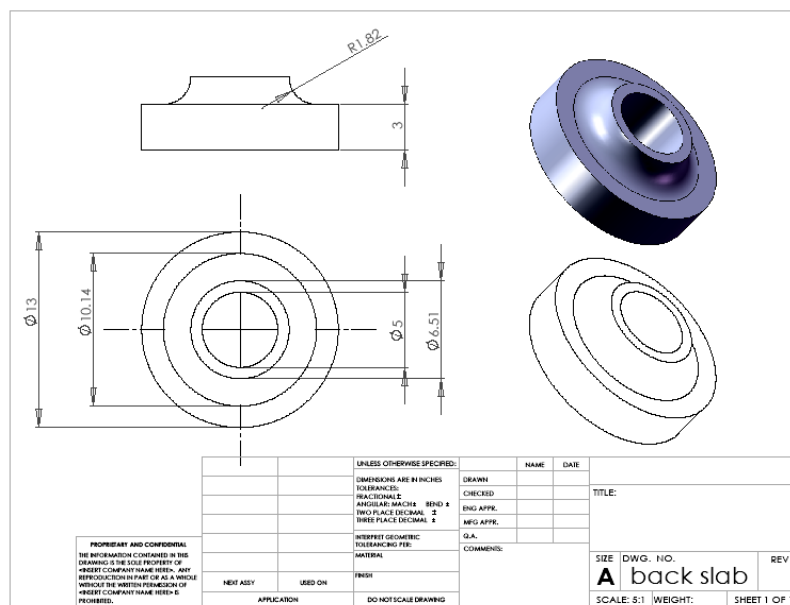


Fig. 5.19(a) 3D design of front slab and back slab

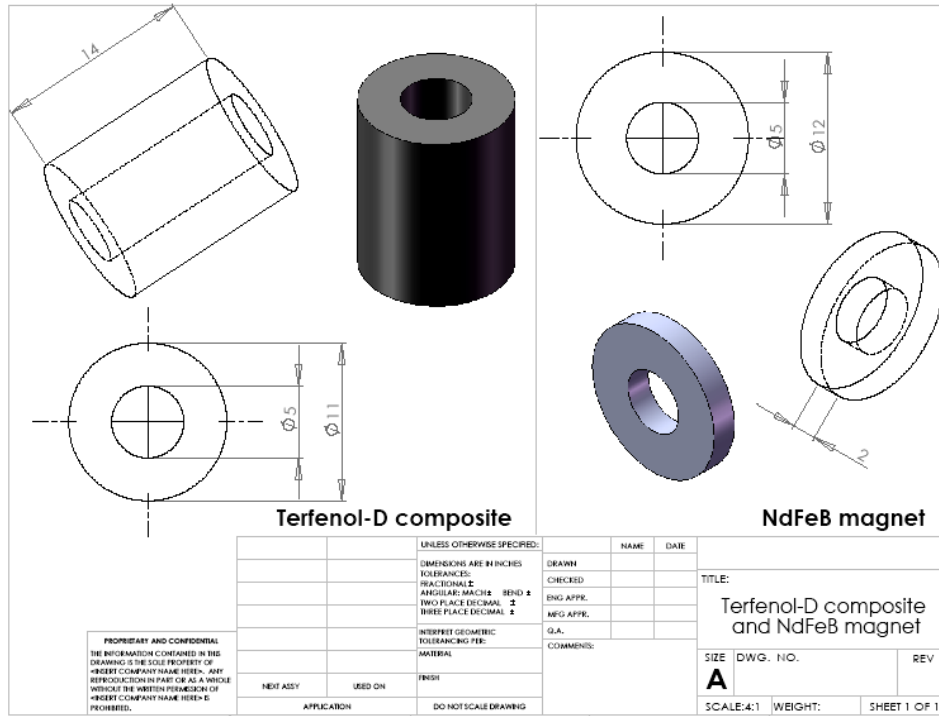


Fig. 5.19(b) Design of Terfenol-D composite and NdFeB permanent magnet

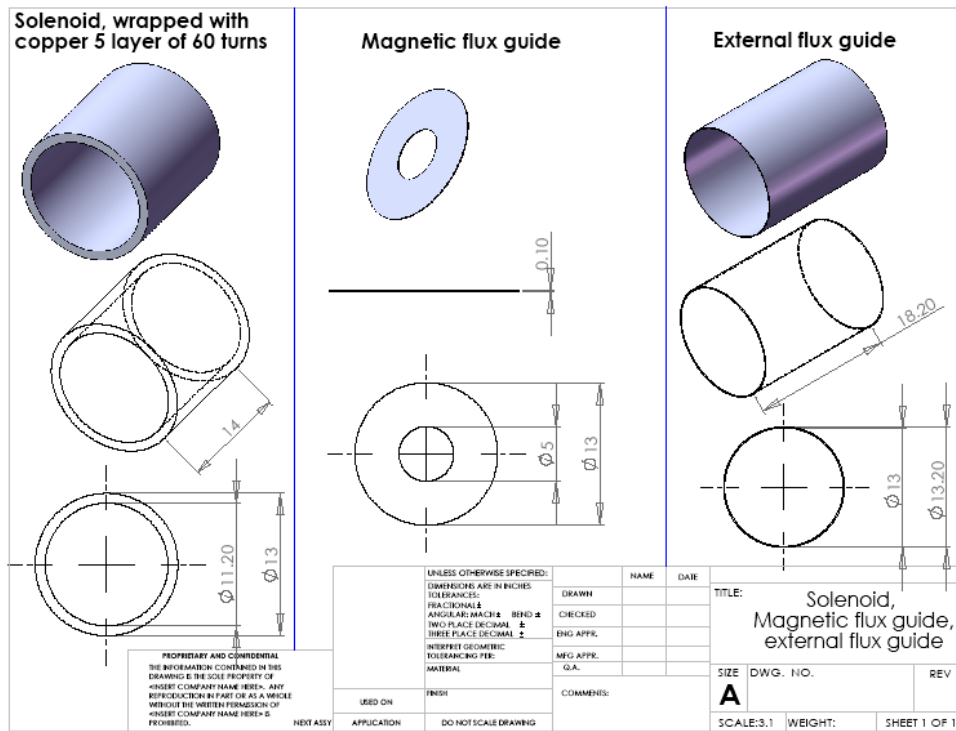


Fig. 5.19(c) Design of solenoid, magnetic flux guide and external flux guide

Although a good result is obtained in the simulation, the experimental measurement is also required. The dynamic performances of the transducer were characterized by measuring the electrical resonance characteristics and vibrational characteristics. The experimental details of these two parts are described in next chapter, together with results and discussion. Here are the parts and assemblies of the transducer:



Fig. 5.20 Terfenol-D continuous fiber composite, front slab and back slab

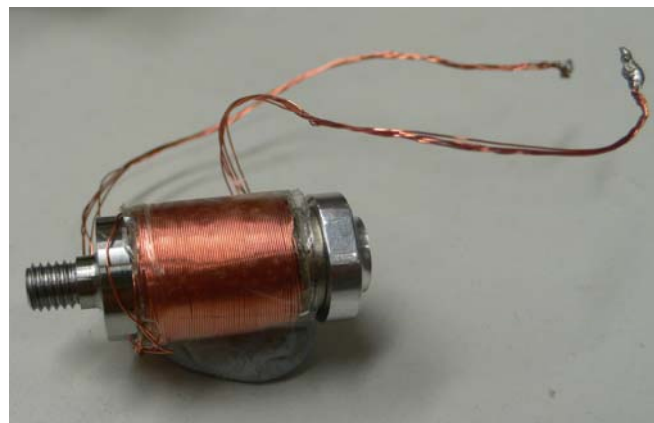


Fig. 5.21 Continuous-fiber composite transducer



5.3.3 Characterization

The electrical resonance characteristics of ultrasonic bonding transducers were evaluated by measuring their electrical impedance spectra using Agilent 4294A precision impedance analyzer with a HP 16047D test fixture. In the setting of the analyzer, continuous taking the data and set “osc level” be 20mA. The DC bias current was set to the value of 100mA. The electrical resonance characteristics of the transducer were measured in the frequency range of 50 kHz to 100 kHz. The transducer was connected to the fixture and free vibration condition was simulated in order to minimize any disturbance to the original behavior of the transducer.

Fig. 5.22 show the measured electrical impedance and phase angle against frequency in range from 55-80 kHz. Effective coupling is a factor between mechanical energy converted and electrical energy input, it shows the efficiency of the transducer. The effective coupling (k_{eff}) of the transducer can be calculated by using

$$k_{eff} = \sqrt{1 - \left(\frac{f_r}{f_n}\right)^2} \quad (5.13)$$

where f_r and f_n are the resonance and anti-resonance frequencies of the transducer, as observed from the complex electrical impedance spectrum respectively, therefore the k_{eff} of the transducer is 0.27.

In Fig. 5.22, a peak and a trough are detected at 64.3 kHz and 66.9 kHz corresponding to the resonance and anti-resonance frequencies of the 14 mm Terfenol-D composite transducer operating in its fundamental longitudinal mode of

vibration. Compare with the simulation, a peak in axial mode is observed in 64.3 kHz, there was 1 % difference between experimental and simulation result.

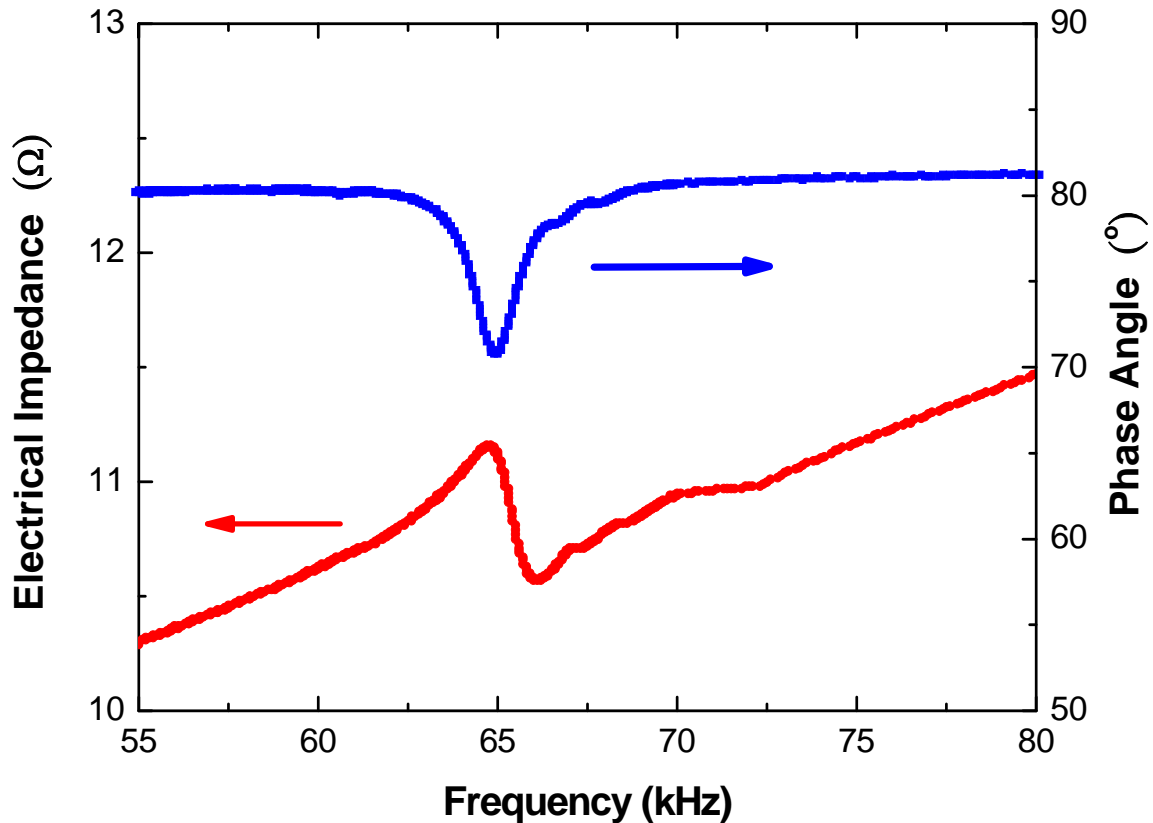


Fig. 5.22 Electrical characteristic of transducer from 55 kHz to 80 kHz

During the measurement, there was a variation with changes in pre-stress. Increasing the pre-stress would shift resonance and anti-resonance frequencies and phase change to higher frequency. Also increasing the length of composite tube would reduce the resonance frequency thus phase change would shift lower too. These phenomenon match the simulation in ANSYS®. The graph below shows the frequency shift when the length of composite changes and the influence of pre-stress.

In the vibrational characteristics measurement, an Ono Sokki CF-5200 multipurpose fast Fourier transform (FFT) analyzer was used to generate a swept



sinusoidal voltage of constant amplitude at sequential frequencies ranging from 0 Hz to 100 kHz. This output drove a Techron 7572 power supply amplifier operated in constant current mode. The constant current from the power supply is provided energy to the drive solenoid of the transducer, producing a sinusoidal (ac) drive field. A laser vibrometer was used to measure the magnetic field induced longitudinal displacement amplitude of the transducer.

Fig. 5.23 shows the measured displacement of transducer with the 14mm long continuous-fiber composite tube as a function of frequency and simulation result when transducer is subject to a magnetic drive field. An obvious maximum peak is observed at 65 kHz, this peak represents the maximum displacement of the transducer and resonance is occurred, which is match the simulation result in the pervious chapter. At resonance, the strain coefficient is found to be 99.6nm/A, which is approximately 100 times larger than its non-resonance values (i.e. 0.80nm/A at 50 kHz), also it is 2.5 times higher than the particulate-chain transducer As can be seen, the spectrum near 65 kHz is quite flat, no significant peaks and displacement surrounding the resonant frequency. As mentioned before, undesirable modes and displacement which near the operation frequency would affect the quality and performance of wire bonding, therefore the transducer can operate in 65 kHz with high quality wire bond.

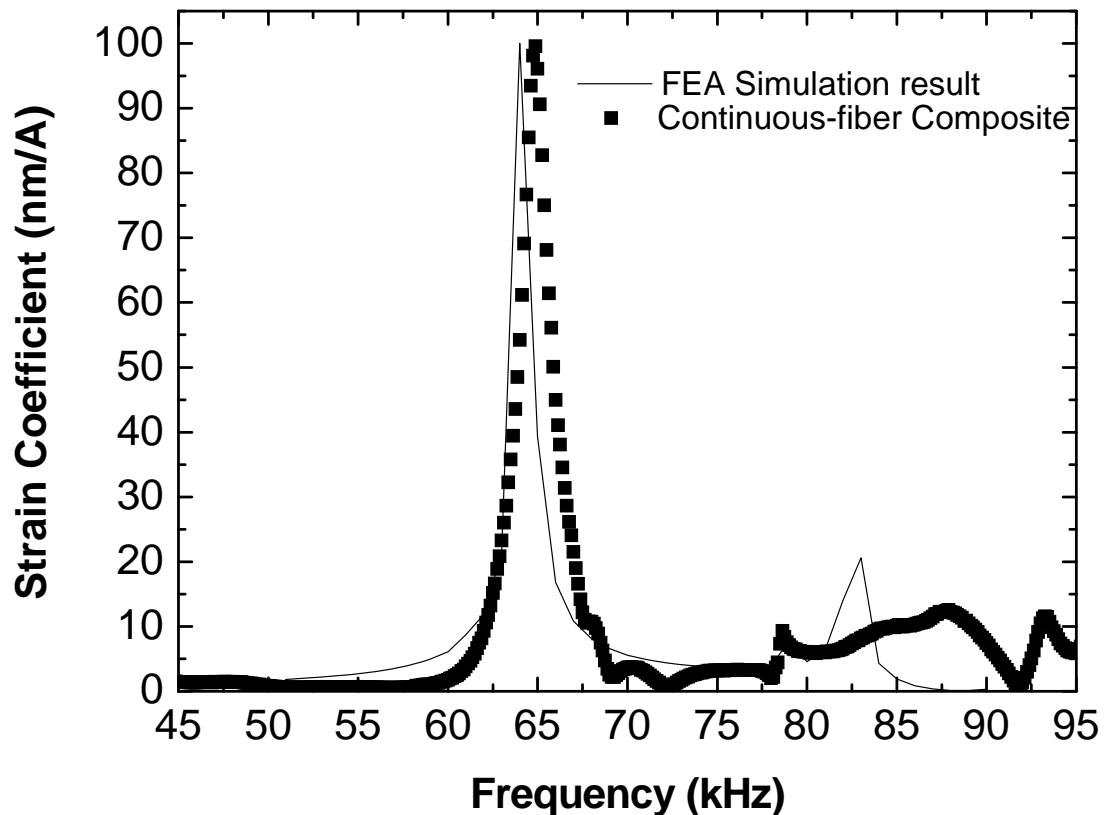


Fig. 5.23 Strain coefficient against frequencies for 14mm long composite transducer

In the vibrational characteristics measurement, the most important and critical parameter which influence the result is the value of pre-stress. During the measurement, a trend can be observed, when reduce the value of pre-stress by not screwing the transducer too heavy, then the spectrum would have lots of fluctuations and lots of peaks would produce. This is due to the mismatch of the composite and the transducer parts. However, when a large pre-stress is applied, most of the vibration would be compressed and the displacement would greatly decrease especially in resonant frequency. Thus no observational peak is generated in the resonant frequency. In conclude, a suitable value of pre-stress is needed to have a better performance of transducer.



5.3.4 Concluding Remarks

A 64-kHz sandwich transducer has been fabricated using an 0.60 volume-fraction Terfenol-D continuous fiber composite tube as the driving element. The dc magnetic performance of the transducer has been analyzed using an ANSYS finite-element model. The dynamic operational performance of the transducer has been characterized by measuring its electrical and vibrational characteristics. The results have revealed a resonance frequency of 65.0 kHz, a strain coefficient of 99.6 nm/A, and with no noticeable eddy-current losses in the transducer for frequencies up to 100 kHz. Therefore, it is practically viable to use Terfenol-D continuous-fiber composites for ultrasonic transducer applications.



Chapter 6

Conclusions and Suggestions for Future Work

6.1 Conclusions

Studies of the design, fabrication, and material properties of epoxy-bonded, [112]-oriented Terfenol-D continuous-fiber magnetostrictive composites have been carried out in this thesis. A demonstration of the application potential of these composites in new generation magnetostrictive transducer and actuator devices has been performed. Conclusions of the thesis are provided in the following sections.

6.1.1 [112]-Oriented Terfenol-D Continuous Fibers

As monolithic Terfenol-D is hard and brittle, traditional mechanical cutting based on diamond sawing is unable to produce Terfenol-D fibers with length-to-width aspect ratios greater than 5:1. In this work, bar-shaped, [112]-oriented Terfenol-D fibers with an extremely high aspect ratio of 45:1 (45 mm long, 1 mm wide) have been successfully produced a specific wire electrical discharge machining (WEDM) process. The resulting crystallographically oriented continuous fibers, which are significantly longer than the state-of-the-art, needle-shaped Terfenol-D short fibers of aspect ratio 4:1 (about 3 mm long and 0.8 mm wide), represent a major breakthrough in enabling engineering magnetostrictive composites with preferred crystallographic orientation.



6.1.2 Epoxy-Bonded Terfenol-D Continuous-Fiber Composites

The prepared [112]-oriented Terfenol-D continuous fibers have been used to fabricate bar-shaped, epoxy-bonded, [112]-oriented Terfenol-D continuous-fiber composites of 45 mm long and (12 mm × 12 mm) square cross section with six different Terfenol-D volume fractions ranging from 0.2 to 0.7. State-of-the-art epoxy-bonded Terfenol-D short-fiber and particulate-chain composites of the same dimensions have also been fabricated for comparison.

The quasistatic magnetic and magnetostrictive properties of the continuous-fiber composites have been measured as functions of applied magnetic field, Terfenol-D volume fraction, and post-curing temperature with zero external stress loading and at room temperature, together with the monolithic Terfenol-D, short-fiber composites, and particulate-chain composites. Significant improvement in the magnetostrictive properties of the continuous-fiber composites has been found. In particular, huge saturation magnetostrictive strains in excess of 1600 ppm, being 44, 56, and 144 % larger than the monolithic Terfenol-D, short-fiber composites, and particulate-chain composites, respectively, has been achieved in unloaded continuous-fiber composites with 80 °C post-curing at 400 kA/m. The investigation into the domain magnetization and magnetostriction processes of the materials has revealed the physical original of the non-180° domain wall motion in general and the 90° domain wall motion in particular. It has been learnt that the higher fiber aspect ratio for greater stress transfer from the continuous fibers to the matrix and the texturing of the continuous fibers along the highly magnetostrictive [112] crystallographic axis are both beneficial to the practical realization



of the giant unloaded saturation magnetostrictive strains. Based on the composite mechanics and filled with the requirements for temperature-dependent stress equilibrium within the composites and stress-dependent saturation strain of Terfenol-D, a physical model has been developed, and a confirmation of the “preset” of the maximum number of non-180° (or 90°) domain state in the continuous-fiber composites via the optimal development of residual compressive stresses in the embedded continuous fibers during the composite post-curing process has been made.

The dynamic magnetic and magnetostrictive properties of the continuous-fiber composites have been evaluated as functions of frequency, magnetic bias field, and Terfenol-D volume fraction. The frequency dependent data has indicated an insignificant eddy-current effect in the composites for operating frequencies up to 500 kHz; the bias field dependent data has provided an improved understanding of the magnetization and magnetostriction processes in the composites; and the volume fraction dependent data has suggested an optimal device performance and cost by using composites with Terfenol-D volume fractions not less than 0.5. A guide to designing and optimizing the composites for device applications has also been generated.

6.1.3 Applications to Smart Devices

Two innovative types of smart devices, including a tunable vibration absorber and a 64 kHz sandwich transducer, have been developed and presented to demonstrate the superior quasistatic and dynamic properties of the continuous-fiber composites, respectively.



The tunable vibration absorber has been created for active absorption of vibrations in vibrating structures. It consists of a piezoelectric ceramic–magnetostrictive composite sensor/actuator suspended in a mounting frame by two flexible beams connected to axial ends of the sensor/actuator. The sensor/actuator serves to produce an axial force for tuning of the natural frequency of the TVA, to gather the signals associated with structural vibrations and to provide a lumped damped mass for the TVA. By monitoring the sensor/actuator output voltage while adjusting its input magnetic field, the natural frequency of the TVA is tuned to the targeted resonance frequency of a structure. The working principle, design prototype, and operating performance of a 57.8 Hz absorber have been reported. A high tunability of natural frequency of 12 % and a good sensibility of vibrations comparable to a commercial accelerometer have been obtained in conjunction with a high absorbability of vibrations of 3.4 dB in a steel plate-neoprene resilient mounts structure.

The 64 kHz sandwich transducer has been designated to function as a half-wave, longitudinal, mass-spring-mass, linear vibrator and to alleviate the intrinsic eddy-current losses in magnetostrictive alloy-based transducers. It has a length of 14 mm and consists of a magnetic circuit and a prestress mechanism. The magnetic circuit is composed of the composite tube, a pair of ring-shaped NdFeB permanent magnets, a drive solenoid, and a Ni-based magnetic flux guide. The distributions of the dc magnetic flux lines and magnetic field strength of the transducer have been determined using an ANSYS finite-element model. The dynamic performance of the transducer has been evaluated by measuring its electrical and vibrational characteristics. The results have revealed that the



transducer resonates at a frequency of 65 kHz with a strain coefficient of 99.6 nm/A, and an effective coupling coefficient of 0.27. Eddy-current losses in the transducer have been insignificant in the measured frequency range of 45 – 95 kHz. The good transducer performance has indicated promising applications of the continuous-fiber composites in ultrasonic devices.

6.2 Suggestions for Future Work

6.2.1 Epoxy-Bonded, Light Rare Earths-Substituted Terfenol-D Continuous-Fiber Composites

The success in fabricating Terfenol-D continuous-fiber composites has marked a milestone of producing engineering magnetostrictive composites. While Terfenol-D and its composites are useful in general, they constitute large amounts of rare and expensive heavy rare earths Tb and Dy. These heavy rare earths, Tb in particular, are much less abundant in the Earth's crust than their light rare earths counterparts such as neodymium (Nd), praseodymium (Pr), etc. In fact, the abundance for Tb and Dy are only 1.1 and 4.5 g/tonne compared to 38 and 9.5 g/tonne for Nd and Pr. Due to their higher density and difficulty in mining and purification, prices of Tb and Dy are significantly higher than the light rare earths (i.e., 0.2 and 1 cm³/USD for Tb and Dy versus 4.9 and 5 cm³/USD for Nd and Pr). By comparison, the abundance for Fe and aluminum (Al) are as high as 41,000 and 82,000 g/tonne, and their market prices are as low as 1,058 and 146 cm³/USD, respectively. The global strategy for utilization and protection of natural resources has resulted in a number of strategic research programs worldwide, especially in the US,



Europe, China, Japan, and South Korea, since the 1990s to find good replacements for Terfenol-D by using light rare earths in substitution for Tb and/or Dy in the ordinary Terfenol-D composition. To date, reports in the literature have concentrated mainly on the light rare earths-substituted magnetostrictive alloys. Therefore, the continuous-fiber composites developed in the present study will lead to the realization of low-cost, high-performance epoxy-bonded, light rare earths-substituted Terfenol-D continuous-fiber composites in the near future.

6.2.2 Power Sonic and Ultrasonic Applications

The overall enhancement of the quasistatic and dynamic magnetostrictive properties of the continuous-fiber composites has shown great promise in transducer and actuator applications. In practice, these composites can be used in a broad range of immediate applications, such as transducers for underwater sonar, industrial cleaning, machining, bonding and welding, dental and surgical tools, vibration control, as well as chemical and food processing, to name a few. Moreover, these composites can be deployed in novel applications where the eddy current-induced heating and bandwidth limitation, brittleness-imposed challenges to machining and shape novelty, and composition and property varieties are of great concern.



List of References

- [1] D. Jiles, *Introduction to Magnetism and Magnetic Materials*, Second Edition, Chapman & Hall, London, 1998.
- [2] R. A. McCurrie, *Ferromagnetic Materials : Structure and Properties* Academic, London ; San Diego, 1994.
- [3] Richard M. Bozorth, *Ferromagnetism* ; Piscataway, N.J. : IEEE Press, New York, 1978.
- [4] Martin, D. H., *Magnetism in Solids*, Iliffe, London, 1967.
- [5] K. H. J. Buschow and F.R. de Boer, *Physics of Magnetism and Magnetic Materials*, Kluwer Academic/Plenum Publishers, New York, 2003.
- [6] A. Goldman, *Handbook of Modern Ferromagnetic Materials*, Kluwer Academic Publishers, Boston , 1999
- [7] D. Craik, *Magnetism : Principles and Applications*, J. Wiley, Chichester ; New York, N.Y , 1995.
- [8] E. D. Torre., *Magnetic Hysteresis* , IEEE Press, New York , 1999
- [9] G. Bertotti., *Hysteresis in Magnetism : for Physicists, Materials Scientists, and Engineers* , Academic Press, San Diego, 1998.
- [10] S. Chikazumi, *Physics of Ferromagnetism*, Clarendon Press, Oxford ; Oxford University Press, New York, 1997.



- [11] R. R. Birss, C. A. Faunce and E. D. Isaac, "Magnetomechanical effects in iron and iron-carbon alloys", *J. Phys. D: Appl. Phys.*, Vol. 4, No. 7, pp. 1040-1048, 1971
- [12] G. T. Rado and H. Suhl, *Magnetism*, Academic P., New York, 1963
- [13] Magnetostriction - Wikipedia, the free encyclopedia, retrieved December 2006, from <http://en.wikipedia.org/wiki/Magnetostriction>
- [14] A. E. Clark, "Magnetostrictive rare earth-Fe₂ compounds", *Ferromagnetic materials*, E. P. Wohlfarth, editor, North-Holland Publishing Company, Amsterdam, Vol. 1, pp. 531-589, 1980.
- [15] E. W. Lee, "Magnetostriction and magnetomechanical effects", *Report Progress in Physics*, Vol. 18, pp. 184-220, 1955.
- [16] V. K. Wadhawan, *Introduction to Ferroic Materials*, Gordon and Breach Science Publishers, Amsterdam, The Netherlands, 2000
- [17] *Handbook of Industrial Materials*, Elsevier Advanced Technology, Oxford, 1992
- [18] M. Wun-Fogle, J. B. Restorff, K. Leung, J. R. Cullen, and A. E. Clark, "Magnetostriction of Terfenol-D heat treated under compressive stress," *IEEE Transactions on Magnetics*, Vol. 35, No.5, pt.2, pp. 3817-3819, 1999.
- [19] A. E. Clark, J. P. Teter, and O. D. McMasters, "Magnetostriction 'jumps' in twinned Tb_{0.3}Dy_{0.7}Fe_{1.9}" *Journal of Applied Physics*, Vol. 63, No.8, pt.2B, pp. 3910-3912, 1988.



- [20] B. W. Wang, S. C. Busbridge, Y. X. Li, and A. R. Piercy, "Magnetostriction and magnetization process process of $Tb_{0.27}Dy_{0.73}Fe_2$ single crystal," *Journal of Magnetism and Magnetic Materials*, Vol. 218, pp. 198-202, 2000.
- [21] J. B. Restorff, "Magnetostrictive materials and devices", *Encyclopedia of Applied Physics*, Vol. 9, pp. 229-244, 1994.
- [22] F. V. Hunt, "Electroacoustics: the analysis of transduction and its historical background", *American Institute of Physics for the Acoustical Society of America*, 1953.
- [23] S. Legvold, J. Alstad, and J. Rhyne, "Giant Magnetostriction in Dysprosium and Holmium Single Crystals," *Phys. Rev. Lett.*, Vol. 10, No.12, pp. 509-511, 1963.
- [24] A. E. Clark, B. DeSavage, W. Coleman, E. R. Callen, and H. B. Calen, "Saturation Magnetostriction of Single-Crystal YIG," *Journal of Applied Physics*, Vol. 34, No. 4, pp. 1296-1297, 1963.
- [25] A. E. Clark, B. F. DeSavage, and R. Bozorth, "Anamalous Thermal Expansion and Magnetostriction of Single Crystal Disprosium," *Physical Review*, Vol.138, No. 1A, pp. 216-224, 1965.
- [26] J. J. Rhyne, and S. Legvold, "Magnetostriction of Tb Single Crystals", *Physical Review*, Vol. 138, 2A, pp. 507-513, 1965
- [27] A. E. Clark, "Magnetostrictive rare earth- Fe_2 compounds," *A handbook on the properties of magnetically ordered substances*, Vol. 1, Wolfarth, E. P., ed. pp. 531-589, 1980.
- [28] M. Schwartz, *Encyclopedia of Smart Materials*, J. Wiley, New York, 2002.



- [29] A. Vlot and J. W. Gunnink., *Fibre Metal Laminates : An Introduction*, Kluwer Academic Publishers, Dordrecht ; Boston, 2001
- [30] L. Sandlund, M. Fahlander, T. Cedall, A. E. Clark, J. B. Restorff and M. Wun-Fogle, "Magnetostriction, elastic modules, and coupling factors of composite Terfenol-D", *Journal of Applied Physics*, Vol. 75, No. 10, pp. 5656-5658, 1994.
- [31] L. Ruiz de Angulo, L. Abell and I. R. Harris, "Magnetostrictive properties of polymer bonded Terfenol-D", *Journal of Magnetism and Magnetic Material*, Vol. 157, pp.508-509, 1996.
- [32] S. W. Or, N. Nersessian, and G. P. Carman, "Dynamic Magnetomechanical Behavior of Terfenol-D/Epoxy 1-3 Particulate Composites", *IEEE Transactions on Magnetics*, Vol. 40, No. 1, pp. 71-77, 2004.
- [33] G. P. McKnight, *[112] Oriented Terfenol-D composites*, Los Angeles: University of California Doctoral Dissertation, 2002.
- [34] Baotou Rare Earth Research Institute data sheet, from <http://www.brire.com/brire/cpxx/cpxx.htm>
- [35] S. W. Or, and G. P. Carman, "Dynamic Magnetoelastic Properties of Epoxy-Bonded Terfenol-D Particulate Composite with a Preferred [112] Crystallographic Orientation", *IEEE Transactions on Magnetics*, Vol. 41, No 10, pp.2790-2792, 2005.
- [36] Electrical discharge machining- Wikipedia, the free encyclopedia, Retrieved June 2006, from http://en.wikipedia.org/wiki/Electrical_discharge_machining



- [37] C. Y. Lo, S. W. Or, and H. L. W. Chan, "Large Magnetostriction in Epoxy-Bonded Terfenol-D Continuous-Fiber Composite with [112] Crystallographic Orientation", *IEEE Transactions on Magnetics*, Vol. 42, No. 10, pp.3111–3113, 2006.
- [38] C. L. Lee, K. H. Wei, "Curing kinetics and viscosity change of a two part epoxy resin during mold filling in resin-transfer molding process", *J Appl Polym Sci*, Vol. 7, No. 2, pp.139 -148, 2000.
- [39] AralditeLY564/Aradur2954 data sheet, from, retrieved March 2004 <http://www.huntsman.com/advanced%5Fmaterials/>
- [40] M. Al-Jiboory, D. G. Lord, Y. J. Bi, J. S. Abell, A. M. H. Hwang, and J. P. Teter, M. Al-Jiboory and D. G. Lord, "Magnetic domains and microstructural defects in Terfenol-D", *Journal of Applied Physics*, Vol. 73, pp. 6168, 1993.
- [41] J. C. Halpin and J. L. Kardos "Halpin-Tsai equations:A review", *Polymer Engineering and Science*, Vol. 16, No. 5, pp 344-352, 1976.
- [42] Berryman, J. G.. "Generalization of Eshelby's formula for a single ellipsoidal elastic inclusion to poroelasticity and thermoelasticity." *Phys. Rev. Lett.*, Vol. 79, pp. 1142–1145, 1997.
- [43] D. Stroud, "The effective medium approximations: some recent developments", *Superlattices and Microstructures*, Vol. 23, No, 3, pp. 567-571, 1998
- [44] K. S. Ravichandran, "Elastic properties of two-phase composite", *Journal of American Ceramic Society*, Vol. 77, No. 5, pp.1178-1184, 1994.



- [45] H. L. W. Chan, and J. Unsworth, "Simple model for piezoelectric ceramic/polymer 1-3 composites used in ultrasonic transducer applications", *IEEE Transactions on Ultrasonics, Ferroelectrics and Frequency on Control*, Vol. 36, No. 4, pp. 434-441, 1989.
- [46] K. A. Klicker, *Piezoelectric composite with 3-1 connectivity for transducer applications*, Solid State Science, The Pennsylvania State University Doctoral Dissertation., 1981.
- [47] H. L. W. Chan, *Piezoelectric ceramic/polymer 1-3 composites for ultrasonic transducer applications*, Mac-quarie University Doctoral Dissertation., 1987.
- [48] T. R. Gururaja, W. A. Schulze, L. E. Cross, and R. E. Newnham, "Piezoelectric composite materials for ultrasonic transducer applications. Part 11: Evaluation of ultrasonic medical applications. " *IEEE Trans. Sonics Ultrasonics*, Vol. 32, pp. 499-513, 1985.
- [49] J. B. Hunt, *Dynamic Vibration Absorbers.*, The Garden City Press: U.K., 1979.
- [50] T. S. Davis, Adjustable tuned mass damper, US Patent US 6,681,908 B2, 2004.
- [51] A. B. Flatau, M. J. Dapino, & F. T. Calkins, High bandwidth tunability in a smart vibration absorber. *Journal of Intelligent Material Systems and Structures* Vol. 11, pp. 923-929, 2000.
- [52] N. Jalili, & D. W. Knowles IV, Structural vibration control using an active resonator absorber: modeling and control implementation. *Smart Materials and Structures* Vol. 13: pp. 998-1005, 2004.
- [53] E. Rustighi, M. J. Brennan, & B. R. Mace, A shape memory alloy adaptive tuned vibration absorber: design and implementation. *Smart Materials and Structures* Vol. 14, pp. 19-28, 2005.



- [54] S. W. Or, H. L. W. Chan, P. K. Choy, & P. C. K. Liu, Tunable vibration absorption device. US Patent US 2006/0175169 A1. 2006.
- [55] W. T. Thomson, & M. D. Dahleh, *Theory of Vibration with Applications*. Prentice Hall: N.J., U.S.A., 1998.
- [56] D. Li, S. W. Or, H. L. W. Chan, P. K. Choy, & P. C. K. Liu, Tunable vibration absorber incorporating piezoceramic sensor/actuator. *Japanese Journal of Applied Physics*, Vol. 45(5B): pp. 4787-4792. 2006.
- [57] C. Y. Lo, S. W. Or, & H. L. W. Chan, Large magnetostriction in epoxy-bonded Terfenol-D continuous-fiber composite with [112] crystallographic orientation, *IEEE Transactions on Magnetics* Vol. 42(10), pp. 3111-3113, 2006.
- [58] S. W. Or, C. S. Yung, & C. Y. Lo, A 64-kHz sandwich transducer fabricated using pseudo 1-3 magnetostrictive composite. *IEEE Transactions on Magnetics* Vol. 42(1), pp. 47-50. 2006.
- [59] S. W. Or, N. Nersessian, & G. P. Carman, Dynamic magnetomechanical behavior of Terfenol-D/epoxy 1-3 particulate composites. *IEEE Transactions on Magnetics* Vol. 40(1), pp. 71-77, 2004.
- [60] T. Li, S. W. Or, and H. L. W. Chan, Magnetolectric effect in a parallel sandwich of magnetostrictive pseudo 1-3 composite and piezoelectric 2-2 composite. *Journal of Magnetism and Magnetic Materials* Vol.304(1), pp.442-444,2006.